Ghent University
Faculty of Sciences

Development of Full-Field and Scanning X-ray Fluorescence Microspectroscopy

Ir. Jan Garrevoet

Dissertation submitted to obtain the academic degree of Doctor in Science

Ghent University
Faculty of Sciences

Promotor: Prof. Dr. Laszlo Vincze
Dr. Bart Vekemans

Exam Commission: Prof. Dr. Karel Strijckmans
Prof. Dr. Laszlo Vincze
Dr. Bart Vekemans
Prof. Dr. Luc Van Hoorebeke
Prof. Dr. Peter Vandenabeele
Dr. Gerald Falkenberg
Dr. Imre Szalóki

Words of Thanks

Although a PhD is a personal endeavour, an endeavour I liked a lot, it would not have been possible without the help of others. During this period I have met and worked with a lot of great people, one slightly crazier than the other.

Prof. Dr. Laszlo Vincze, my promotor, gave me the possibility to go on this wonderful journey and was always there when I needed some advice, even when I called him at 4 at night he still showed up at the beamline to give us a helping hand in figuring out what the problem was. I enjoyed all the talks we had about physics, cars, and computer electronics.

I would also like to thank the Agency for Innovation by Science and Technology (IWT) for the financial support.

Dr. Bart Vekemans, my co-promotor, you introduced me into the world of IDL, ”mijlstenen”, and ”monsters”. I can still remember in 2010 you letting me take the pilot seat at a beamline for the very first time. We shared a passion for music which resulted in a few weird sing along moments.

Tom, my linux/mac brother, you showed me the wonderful world of writing IDL to C bindings, gave a greater insight into linux, I missed you having around as a fellow computer geek but absolutely didn't miss the high pitch heavy metal noises reaching my side of the office :-P. Which brings me to Lien, who was glad I left for the office at the end of the corridor because I was driving her insane with my hyperactive legs. Sorry for that! Although our scientific paths did not cross very often, I will never forget that one beamtime at beamline L.

Eva, or Britney ;-), we shared a lot of time together at ID13 and P06 or in the car for that matter, and got to know each other pretty well over time. I always enjoyed talking to you and working together on projects.

Pieter, although we from time to time have different opinions, we made a good team during the beamtimes we did with the SLcam®. If you ever want to through a weird play list, check Pieters iPod.

Stephen, mister ”I have one more question”, you showed a natural interest for all the Monte Carlo simulations and were not afraid to disturb me

over and over again with another question. Stephen, +1. But please do not play the Pokemon rap again while I am coding ;-).

Brecht, we have not spent a lot of time together (can quickly change during a beamtime), but each time we did I had a nice time. Checking out the performance of the new sources, looking at the sometimes strange detector settings, ...

With Matthieu on the other hand I have spent more time in a confined space than is healthy for a normal human being, luckily we are not entirely normal ;-). Matthieu and I never seemed to have gotten along with the sequencer... I look forward to our ongoing collaboration.

Michiel, David, and Maarten it has been a pleasure working with you. See you at the coffee machines!

Manfred, Gerald, Paul, Anne, Adeline, Sylvain, Sylvia, Frank, and Thorsten for all the nice experiments and synchrotron moments.

Stijn, keep on doing what you are doing and I am glad you can take over my function of night guard of S12.

Peeps from S12, you will be truly missed! I deeply enjoyed are conversations during lunch, team building activities, and all the other interesting experiences I shared with you guys. You all made S12 like a home to me ;-) And on that point, I would like to say thanks to my parents for keeping up with the ghost that appeared to be living in your house, appearing late at night and disappearing again in the morning, while only leaving behind a few clues of its existence, laundry and missing food.

Lastly I need to thank the zoo. They seem to have the special ability to endure or filter out the right part of the spectrum enabling them to share a life with me. Thanks!!

Jan Garrevoet
Hamburg
June 2015

Table of Contents

List of Figures

List of Tables

Acronyms

η efficiency coefficient. 2-3

E_c critical energy. 2-10, 2-11

E_{kin} kinectic energy. 2-1

A activity. 2-2

ADC Anolgue Digital Converter. 2-37, 3-4

B brilliance. 2-7

BM bending magnet. 2-5, 2-12, 2-14

Bq Becquerel. 2-2

CAMEX CMOS amplifier and multiplexer. 2-37, 3-2–3-4, 3-13, 3-14

CCM channel cut monochromator. 2-26

CNT carbon nanotubes. 2-4

CORBA Common Object Request Broker Architecture. 4-2

CR Count Rate. 3-15

CT computed tomography. 1-2, 4-11, 4-12, 5-13, 6-2, 6-4, 6-5, 6-7–6-9, 8-2

CTE charge transfer efficiency. 3-10

DA Dynamic Analysis. 2-43, 2-44

DCC Doubly Curved Crystal. xii, xiv, 1-2, 2-24, 2-25

DCM double crystal monochromator. 2-26

DUBBLE Dutch Belgian Beamline. 4-14

ED Energy Dispersive. xiii, 8-1–8-3

ENC equivalent noise charge. 2-35, 2-36

ER energy resolution. 3-16, 3-17, 8-1

ESRF European Synchrotron Radiation Facility. 4-11, 4-12, 4-14

F Fano factor. 2-35

F flux. 2-7

FE Field Emission. 2-4

FEL free electron laser. 2-9

FET front-end transistor. 2-31, 2-32

FPM Fundamentel Parameter Method. 2-45, 2-47

FWHM Full Width At Half Maximum. 2-34, 2-35, 3-16

GUI Graphical User Interface. 3-8

HDF5 Hierarchical Data Format 5. 3-9, 3-10

HPGe high purity germanium. 2-30

ID insertion device. 2-5, 2-6, 2-11, 2-12, 6-5

KB Kirkpatrick-Baez. 2-20, 2-21

LN2 liquid nitrogen. 2-30

OOT Out of Time. 3-10–3-12

PRNG Pseudo Random Number Generator. 2-48

PT Peaking Time. 3-16

QE quantum efficiency. 2-34

QM quadrupole magnet. 2-5

RAID redundant array of inexpensive disks. 3-11

ROI Region Of Interest. 2-41, 3-9, 3-10, 4-14, 4-15

SDD Silicon Dirft Detector. xii, 2-30, 2-31, 3-13, 3-15, 3-16, 4-14, 6-8

SR synchrotron radiation. 2-9

SRM Standard Reference Material. 1-2, 2-44, 2-47, 8-3

TANGO TAco Next Generation Objects. 4-2

TEC Thermoelectric Modules. 3-4, 3-5

UPS Uninterruptable Power Supply. 3-4

XANES X-ray Absorption Near Edge Structure. 4-13–4-15

XRF X-ray Fluorescence. xiii, 1-1, 1-2, 2-39, 2-40, 2-44, 2-48, 3-1, 3-12, 3-17, 4-4, 4-7, 4-8, 4-11, 4-12, 5-13, 6-1, 6-2, 6-4, 6-5, 6-8, 8-2, 8-3

Nederlandstalige Samenvatting

De meest recente ontwikkingelingen aangaande energie dispersieve X-stralen detector technologie opent nieuwe wegen voor de drie dimensionale bepaling van (spoor) elementen in monsters op de micrometer schaal. De momenteel standaard methoden om 3D elementaire informatie te bekomen, confocaal X-stralen Fluorescentie (XRF) en Computationele Tomografie (CT) XRF, leveren bevredigende resultaten op maar zijn tijdrovend en vereisen drie dimensionale beweegbaarheid van het monster. Het gebruik van grote oppervlakten detectoren, zoals de Maia detector, hebben als groot voordeel hun grote ruimtehoek waaronder ze X-stralen kunnen detecteren, waardoor steeds kortere meettijden mogelijk worden. Deze hogere efficiëntie zorgt ervoor dat technieken voor 3D XRF steeds attractiever worden en dus ook meer algemeen worden toegepast.

Door de introductie van een nieuwe 2D ED detector, SLcam® genaamd, werd het mogelijk om in één keer twee dimensionale elementaire distributie beelden te bekomen wanneer het monster met een ongefocuseerde X-stralen bundel wordt belicht. Door de combinatie van deze nieuwe 2D ED detector met een lineair gefocuseerde X-stralen bundel, bekomen door slechts gebruikt te maken van één van de spiegels van een Kirkpatrick-Baez spiegel paar aan de P06 bundellijn van de Petra III deeltjesversneller in Hamburg, demonstreerden we een nieuwe methodologie voor drie dimensionele elementaire beeldvorming. Deze nieuwe metholodogie voor 3D μXRF beeldvorming werd getest op natuurlijke diep aarde diamanten welke wolken van natuurlijke inclusies bevat. Door het sample lineair orthogonaal te scannen doorheen de horizontaal gefocuseerde X-stralen bundel verkrijgt men excitatie en detectie van verscheidene 2D elementaire distributie beelden, welke gecombineerd kunnen worden tot een drie dimensionale representatie van het monster zonder gebruik te maken van een reconstructie algoritme. Door het grote gizichtsveld van de SLcam® ($\sim 2\,\mathrm{mm}$), is het mogelijk om 3D informatie over mm^3 schaal volumes met een resolutie van $\approx 8\,\mu\mathrm{m}$, wat voordien onmogelijk was door gebruik te maken van de conventieel beschikbare methoden.

Een alternatieve methodologie om tomografische elementaire distributie beelden te bekomen werd ontwikkeld door gebruik te maken van een parallele X-stralen bundel en deze te combineren met een spleet gecollimeerde 2D ED detector. De collimator is orthogonaal georienteerd op de bundelrichting zodat elke kolom van de detector overeenkomt met één pixel van het bestraalde pad.Hierdoor wordt de beeldhoek aanzienlijk vergroot waardoor men sneller kan meten. Deze methodologie werd succesvol toegepast aan de ID19 bundellijn aan het ESRF in Grenoble, waar metingen werden uitgevoerd op tanden van chimpansees and Neanderthalers.

Een laboratorium micro XRF spectrometer werd ontworpen welke gebruik maakt van een gemonochromatiseerde X-stralen bundel als primaire excitatiebron en een Silicon Dirft Detector (SDD) detector met als doel het verschaffen van 2D/3D scanning capaciteiten. De spectrometer is gebaseerd op een custom designed versie van de X-beam Superflux MF X-stralen bron (X-ray Optical Systems Inc, Albany, USA), welke gebruik maakt van een $50\,\mathrm{W}$ Mo anode microfocus buis met geïntegreerd 3 Doubly Curved Crystal (DCC) optica die de X-stralen niet enkel focuseert maar ook monochromatiseert. Het monster bevindt zich op een XYZθ positioneringssysteem dat parallel of onder 45° in relatie tot de primaire X-stralen gemonteerd kan worden. De fluorescentie stralen worden gedetecteerd door een SDD (E2v Scientific Instruments) met een actieve dikte van het Si kristal van $450\,\mu\mathrm{m}$ en een oppervlakte van $60\,\mathrm{mm}^2$ welke intern gecollimeerd is tot $50\,\mathrm{mm}^2$. Een Beryllium venster van $8\,\mu\mathrm{m}$ dikte zorgt voor de vacuum afscheiding. Door middel van karakterisatie van de detector elektronica werden de meest optimale instellingen gekozen in combinatie met de gebruikte X-stralen bron. De monochromatische excitatie zorgt ervoor dat, onder de (multiple) Compton/Rayleigh scatter piek regio, de XRF spectra verkregen met deze laboratorie spectrometer gelijkaardige piek-tot-achtergrond verhoudingen heeft zoals deze verkregen worden aan synchrotron bronnen. Hierdoor worden detectie limieten in het sub-ppm domein verkregen voor transitie metalen voor een waaier van sample matrixes in een meettijd van $1000\,\mathrm{s}$. Een Monte Carlo simulatie kwantificatie algoritme, gebaseerd op het in house ontwikkelde software paket XMI-MSIM, werd ontwikkeld waardoor deze spectrometer een ideaal werktuig is voor kwantitatieve scanning μXRF toepassingen in vakgebieden als Aard- en milieuwetenschappen.

Summary

The latest developments in Energy Dispersive (ED) X-ray detection technology opens new avenues for the determination of 3D distribution of (trace) elements within the investigated samples on the microscopic scale. The currently used techniques to obtain 3D elemental images, confocal X-ray Fluorescence (XRF) and XRF tomography deliver satisfactory results but are typically time consuming since both techniques require sample scanning in three dimensions. The use of large array detectors, such as the Maia detector, can however detect X-rays with a large solid angle and high throughput, enabling a considerable decrease in dwell times for fast X-ray fluorescence imaging, making 2D/3D scanning XRF more generally applicable.

By the introduction of a novel 2D energy dispersive (ED) detector (SLcam®), one can directly obtain 2D elemental distribution images of the sample in question when it is illuminated by a broad X-ray beam. By combining this novel 2D ED detector and a linearly focused X-ray beam obtained by using only one mirror of a Kirkpatrick-Baez mirror system at Petra III P06 (DESY, Hamburg, Germany), we demonstrated a new method for 3D elemental micro-imaging. This new methodology towards 3D micro-XRF imaging was tested on deep Earth natural diamonds containing a cloud of mineral inclusions. The sample was scanned through the horizontally focused (vertically oriented) sheet beam of excitation resulting in the generation and detection of multiple 2D elemental distribution images, which were combined to form a 3D representation of all detectable elements present in the sample. Due to the large field of view of the SLcam® ($\sim 2\,\mathrm{mm}$), one can obtain 3D information of mm^3 sized volumes with a spatial resolution of $\approx 8\,\mu\mathrm{m}$, which was previously impractical by using conventional 3D scanning techniques due to the extended measurement time required.

A second methodology to obtain tomographic elemental distribution images was presented using the same ED pixel detector (SLcam®) collimated with a vertical slit, enlarging the effective solid angle of the detector. Illuminating the sample with a pencil beam results in the simultaneous meas-

urement of the illuminated line profile in the sample, where each column on the detector represents a single pixel along this axis. This methodology was successfully applied during measurements on teeth from chimpanzees and Neanderthals at the ID19 beamline of the ESRF.

Next to methodological developments in synchrotron based XRF imaging, a laboratory micro-XRF spectrometer was developed which combines monochromatic, focused X-ray beam excitation with a high-performance silicon drift detector (SDD) and 2D/3D scanning capability. The spectrometer is based on a customised version of the X-Beam Superflux MF excitation source (X-ray Optical Systems Inc, Albany, USA), employing a $50\,\mathrm{W}$ Mo-target microfocus tube, with integrated DCC optic for beam focusing and monochromatisation. The sample is mounted on a XYZθ motor stage, which can be positioned parallel or at 45° with respect to the primary X-ray beam. The fluorescent X-rays are detected by an SSD detector (E2v Scientific Instruments) having a $450\,\mu\mathrm{m}$ thick Si crystal with an active area of $60\,\mathrm{mm}^2$ which is internally collimated to $50\,\mathrm{mm}^2$ and shielded by an $8\,\mu\mathrm{m}$ thick Be window. The detector settings were adjusted to deliver optimum spectral performance in combination with the used X-ray tube. Due to the monochromatic excitation, below the (multiple) Compton/Rayleigh scatter peak region, the XRF spectra obtained by this laboratory spectrometer has similarly high peak-to-background ratios as can be obtained at synchrotron sources. Therefore sub-ppm minimum detection limits (MDL) for transition metals are obtained for a variety of sample matrices when measured for $1000\,\mathrm{s}$. For quantification purposes a (reverse) Monte Carlo simulation based algorithm was developed, based on the in-house developed MC code XMI-MSIM, making this spectrometer the ideal tool for applications of quantitative scanning micro-XRF in the field of Earth and environmental sciences.

1 General Outline

This dissertation presents methodological developments in the field of micro-X-ray Fluorescence (XRF) imaging. The main focus lays on the use on the characterisation and applications of a novel energy dispersive (ED) X-ray pixel detector, having a high quantum efficiency up to $20\,\mathrm{keV}$. It is able to obtain nearly 70,000 XRF spectra simultaneously with a maximal spatial resolution of $8\,\mu\mathrm{m}$, allowing faster 2D and 3D elemental imaging without the need to use focused X-ray beam excitation. In the second part of the dissertation a novel laboratory micro-XRF spectrometer based on monochromatic excitation that was developed during this PhD work is presented.

Chapter 2 gives an introduction to X-ray sources, X-ray optics and X-ray matter interactions encountered in XRF-spectrometry, relevant for the full understanding of the work presented in this thesis. Special importance is given to X-ray detectors, not only by explaining the general principle of detection, but by also presenting the different components of the pulse processing units, allowing the reader to understand the different parameters and characteristics involved in the characterisation and optimisation of a detector system.

After a brief description of the general detector technology employed in case of the SLcam® in Chapter 2, chapter 3 gives a more comprehensive explanation of the detector principles and their impact on the experimentally obtained results. Chapter 3 also includes a full characterisation of the detector properties, such as noise levels as well as energy and spatial resolution.

The subsequent chapter demonstrates the application of the SLcam® for 2D elemental imaging on a wide variety of samples, including sample types of archaeological, geological and palaeontological origin.

A novel methodology towards 3D micro-XRF is presented in Chapter 5, combining a linearly focused X-ray sheet beam and spatially resolved XRF detection by the SLcam® to obtain elemental images directly from the illuminated cross-sections. This novel approach for elemental imaging is demonstrated by the 2D/3D micro-XRF analysis of inclusion clouds trapped in natural deep Earth diamonds. The results show the complexity of these inclusions and the need to obtain three dimensional elemental information, which was in the past only possible by time consuming three-dimensional scanning. A second example in the field of environmental science shows the application on a biological model organism studying the influence of Ni contaminated sediment on Earth worms.

The combination of pencil beam based excitation with spatially resolved detection by the SLcam®, equipped with a vertically oriented detector collimator slit, is the topic of Chapter 6, describing a new methodology for XRF computed tomography (CT) imaging. An example application in the field of palaeontology demonstrates elemental imaging on teeth of Chimpanzees and Neanderthals.

The final Chapter, Chapter 7, illustrates the development of a laboratory spectrometer utilising a monochromatised X-ray source using Doubly Curved Crystal (DCC) optics. Due to the monochromatic excitation, sub-ppm detection limits are obtained for transition metals due to the excellent peak-to-background ratios. Next to the excellent detection limits, the monochromatic nature of the incident beam allows for much easier modelling of the excitation spectrum using Monte Carlo simulations. This is the basis of an algorithm which is used to obtain quantitative information of the sample utilising reverse (iterative) Monte Carlo simulations. The quantification scheme was cross validated using a NIST Standard Reference Materials(SRMs) and was applied for the quantitative elemental analysis of a rare iron meteorite as a demonstration example.

2

Introduction to X-ray Fluorescence

2.1 X-ray sources

2.1.1 Introduction

X-rays were discovered by Wilhelm Conrad Röntgen in 1895 while studying the properties of cathode rays[1]. Constituting part of the electromagnetic spectrum, X-rays cover the spectral wavelength (energy) range extending from approximately $10\,\mathrm{nm}$ ($\sim 100\,\mathrm{eV}$) to $0.01\,\mathrm{nm}$ ($\sim 100\,\mathrm{keV}$)[2]. Another way of classifying X-rays is based on their generation, described as the radiation generated by high-energy electrons which are slowed down in the outer field of a nucleus or by changes of the bound states of electrons in the inner electronic shells of an atom. X-rays defined by this convention with energies above 100 keV overlap with gamma rays, which are commonly generated by radioactive decay processes. The radiation generated by the deceleration of electrons is called "Bremsstrahlung" and constitutes of a continuum with a sharp termination at the high energy side, corresponding to the maximum kinectic energy (E_{kin}) of the electron. Electron transitions between inner electron shells of the atom may generate x-rays with an energy characteristic to a given element.
Commonly used X-ray sources are generally based on two different principles. First, based on spontaneous radioactive decay of certain radio isotopes, and second, based on either the interaction of artificially accelerated elementary charged particles with matter, as in case of X-ray tubes, or the

acceleration of relativistic charged particles within magnetic fields in accelerators or storage rings.

2.1.2 Radio Isotopes

Natural or artificial radioactive isotopes are compact, low cost, continuously radiating X-ray sources which do not need any power and are independent of the surrounding environment. The major downside of this type of X-ray source is their radiation hazard requiring very strict safety regulations. Despite this downside they are still widely used in applications which provide engineering challenges, such as space missions[3]. The ^{55}Fe electron capture source is widely used as a standard source for the calibration of X-ray detectors and emits the characteristic Mn lines. The activity (A) of a radio isotope is defined as its rate of decay and is expressed in Becquerel (Bq).

$$A = \frac{dN}{dt} \tag{2.1}$$

where N is the number of radionuclide particles and t time.

2.1.3 X-ray Tubes

The first type of X-ray generator, used by W.C. Röntgen, was based on an electric discharge or cathode ray tube (Hittorf-Crooks-tube) where electrons were produced by ion bombardment of a cold cathode in a low pressure gas placed under high voltage[1]. The high kinetic energy electrons (typically having energies of tens of keV), accelerated in the high-voltage electric field of the tube, generate X-rays when impacting and interacting with the anode material. Although similar in working principle, most modern X-ray tubes are based on a design introduced by W.D. Coolidge, who introduced the hot filament electron emitter in a high vacuum tube, shown in figure 2.1[4].

Physical Principles Several physical processes lay at the basis of X-ray generation via X-ray tubes. First, electrons emitted from a heated filament, serving as the cathode, are accelerated towards the anode by applying an electric field created by a positive potential of the anode relative to the cathode. When striking the anode, the electrons interact with its atoms and lose their energy through a number of processes. First process which electrons can undergo is scattering on the target nuclei. The majority will undergo elastic scattering while only a relatively small part undergoes inelastic scattering, gradually losing their energy in the Coulomb field of the

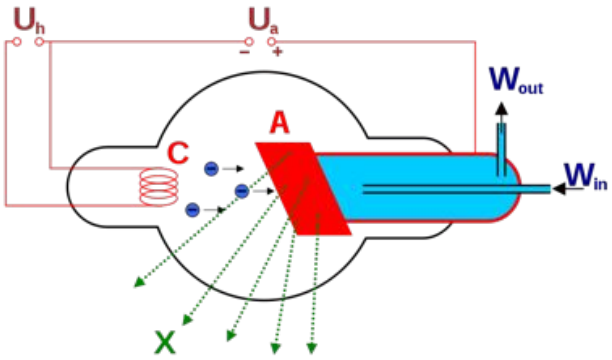

Figure 2.1: General design of a Coolidge X-ray tube with a side window: filament (C), anode (A), and cooling by water. Reproduced from [5].

nuclei. During this deceleration process, their energy is partially converted to polychromatic X-ray radiation, resulting in a continuous spectral component of the tube's emission spectrum which is commonly referred to as Bremsstrahlung, or braking radiation, Figure 2.2. The second process is characterised by the interactions of the incident electrons with bound electrons of the target (anode) atoms through so-called impact ionisation. Collisions with outer electrons, which give rise to small energy losses, dominate over collision with in inner electron. However, once an inner electron has been removed from its orbital a vacancy is created which can be filled by an electron from another orbital with a lower binding energy. This process gives rise to the characteristic lines in the X-ray emission spectrum of the anode material, superimposed on the continuous Bremsstrahlung component (Figure 2.2). The total radiation power can be calculated using the following formula since $v_{e^-} < c$[2]:

$$P = \frac{1}{4\pi\epsilon_0}\frac{2e^2}{3c^2}a^2 \tag{2.2}$$

where v_{e^-} is the electron velocity, a is the acceleration of the charge, ϵ_0 the permittivity of vacuum, e the electron charge, and c the velocity of light in vacuum. The typical efficiency coefficient (η) of the X-ray excitation using an X-ray tube is very low, in the order of $0.1 - 1\,\%$ and can be estimated as follows:

$$\eta \equiv \frac{P}{I \cdot U} \approx 10^{-6} \cdot Z \cdot U \tag{2.3}$$

where Z is the atomic number of the anode material, I is the anode current (A) and where U is the applied high voltage (kV). The main part of the energy of the electrons that bombard the anode is converted into heat. The

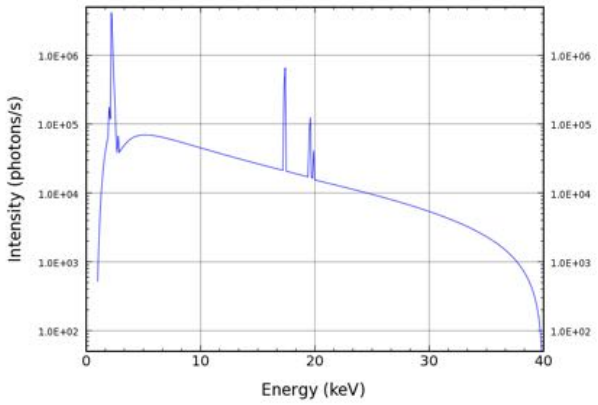

Figure 2.2: Typical spectrum of a Mo based X-ray tube with a Be exit window. ($U = 40\,\mathrm{kV}$, $I = 0.4\,\mathrm{mA}$). Produced using XMI-MSIM[6].

output power of an X-ray tube is often limited by the heat dissipation of the anode. Therefore, high power X-ray tubes often use rotating anode designs distributing the generated heat over a significantly larger area than the electron beam focal spot size.

2.1.4 Technical advances

Next to the X-ray tube based on thermo-electron emitters, recent advances are made to use Field Emission (FE) emitters to replace the hot filament. Promising results are obtained when using carbon nanotubes (CNT) as FE emitters and the first applications seem to be in reach[7–9]. A radically new design of X-ray tube based on liquid metal technology was introduced and makes use of a liquid-metal jet to form a $30\,\mu\mathrm{m}$ diameter gallium anode stream having a flow speed of $20\,\frac{\mathrm{m}}{\mathrm{s}}$ and is bombarded with electrons originating from a $30\,\mathrm{W}$, $50\,\mathrm{kV}$ electron gun[10, 11]. This approach yields the ability to produce small focal spots, typically $10\,\mu\mathrm{m}$, with a brilliance of $> 2 \cdot 10^{10}\,\frac{\mathrm{photons}}{\mathrm{s} \cdot \mathrm{mm}^2 \cdot \mathrm{mrad}^2 \cdot 0\,1\,\%\mathrm{BW}}$.

2.2 Synchrotron Radiation

2.2.1 The Synchrotron

Figure 2.3: A photograph of the European Synchrotron Research Facility (ESRF), Grenoble, France.

X-ray generation via relativistic charged particles in a storage ring, a synchrotron (Figure 2.3), is achieved by forcing elementary charged particles, electrons or positrons, in a curved trajectory by means of various magnetic field structures. Accelerated elementary charged particles, as described by Maxwell's equations, emit electromagnetic radiation. At highly relativistic particle speeds, the emission field is strongly confined in the tangential direction to the acceleration vector, producing the naturally collimated beam of synchrotron radiation within a so-called synchrotron storage ring. A storage ring is a particle accelerator, encompassing a high-vacuum environment (vacuum tube) surrounded by complex magnetic structures in order to guide and store the accelerated electrons or positrons in a closed orbit. While some magnetic structures (e.g. quadrupole magnets) serve exclusively to guide the charged particles in the storage ring vacuum, other magnets, i.e. bending magnets, serve as both guiding devices (to keep the particles on a closed orbit) and synchrotron radiation sources. Alternating pole magnet structures, wigglers or undulators, inserted in the straight sections of the storage ring, serve exclusively as intense sources of synchrotron radiation. Some of the characteristics from the used synchrotron sources are listed in Table 2.1. Bending magnets(BMs) cause the charged particles to change direction thus modulating the orbit and are altered with quadrupole magnets(QMs) whom act as magnetic lenses to focus or defocus the particle beam in horizontal and vertical direction. Undulators and wigglers, generally called insertion devices(IDs), induce oscillations in the particle beam's

Facility (first beam) location / country	Circumference (m)	Beam Energy (GeV)	Current (mA)	Hor. Emittance (nm rad)
ESRF (1992) Grenoble / France	844	6	200	4
PETRA III (2009) Hamburg / Germany	2304	6	100	1

Table 2.1: Characteristics of the synchrotrons used.

trajectory. Therefore the storage ring's magnetic structure is designed to minimise the transversal oscillations, known as betatron oscillations (β). Despite the effort to minimise these oscillations, high and low β sections still remain distributed across the storage ring. The high β sections (large particle beam or source size/low divergence) are optimised for undulator beamlines while the low β sections (small source size/large divergence) are compatible for both undulator as wiggler IDs.

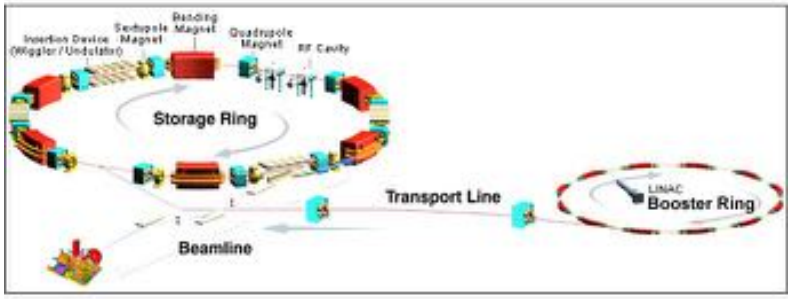

Figure 2.4: Schematic overview of a synchrotron, showing the LINAC, booster ring, storage ring (consisting out of bending magnets, multipole magnets, instertion devices, and RF cavity) and beamline. Adapted from [12].

The emittance (ε) at a certain position in the storage ring can be determined using the following equation where i represents either the horizontal or vertical direction[13]:

$$\varepsilon_i = \frac{\sigma_i^2}{\beta_i} \tag{2.4}$$

	ESRF		Petra III	
	High β	Low β	High β	Low β
β_y (m)	35.20	0.50	20.01	1.20
β_z (m)	2.52	2.73	2.36	3.95
σ_y (µm)	402	59	141.5	34.6
σ_z (µm)	7.9	8.3	34.6	6.3
σ'_y (µrad)	10.7	90	7.1	28.9
σ'_z (µrad)	3.2	3	2.1	1.6

Table 2.2: Accelerator optics functions, electron beam sizes and divergences given as a function of betatron function for the ESRF and Petra III storage ring. Source: ESRF and Petra III

2.2.1.1 Theoretical Aspects

Synchrotron radiation is based on the property that relativistic particles cause highly collimated and extremely bright emission of electromagnetic radiation when accelerated by an external magnetic field. The total power radiated by an accelerated relativistic particle is represented by the Lorentz invariant representation of the Larmore formula[13]:

$$P = \frac{e^2 c}{6\pi\epsilon_0} \frac{1}{(m_0 c^2)^2} \left[\left(\frac{d\vec{p}}{d\tau} \right)^2 - \frac{1}{c^2} \left(\frac{dE}{d\tau} \right)^2 \right] \tag{2.5}$$

where e is the charge of an electron, c the speed of light, m_0 the electron rest mass, $\frac{d\vec{p}}{d\tau}$ and $\frac{dE}{d\tau}$ the momentum and energy derivative to time $d\tau = {}^1/_{\gamma dt}$ respectively, with the Lorentz contraction factor $\gamma = \frac{E}{m_0 c^2}$. When relativistic particles are accelerated in a circular trajectory, as is the case at a synchrotron, Equation 2.5 can be expressed as[13]:

$$P = \frac{e^2 c}{6\pi\epsilon_0} \frac{1}{(m_0 c^2)^2} \frac{E^4}{R^2} \tag{2.6}$$

with E the particle energy and R the bending radius. The relativistic nature of this process causes the dipole pattern to be a forward point cone instead of the isotropic dipole pattern expected from non-relativistic theory.

2.2.1.2 Synchrotron Radiation Characteristics

Flux and Brilliance Flux (F) is defined as number of photons per second per energy bandwidth, typically $\frac{\delta E}{E} = 10^{-3}$. Brilliance (B) specifies the

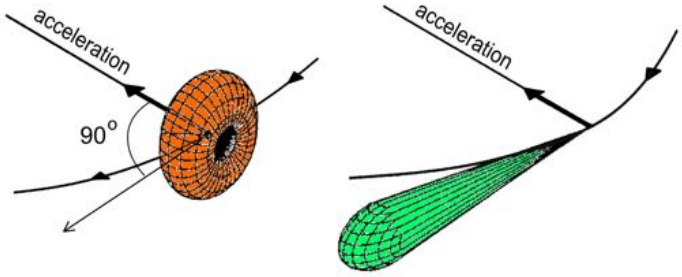

Figure 2.5: Radiation dipole pattern of a relativistic particle forced around a circular trajectory in both particle (left) and lab (right) frame. Adapted from [14].

radiated spectral flux, within a relative energy bandwidth (BW), normalised by the four dimensional phase space spanned by the source size $\left(\sum_{x,y}\right)$ and divergence $\left(\sum'_{x,y}\right)$[13]:

$$B(z) = \frac{F(E,z)}{BW \cdot \sum_x(z) \sum_y(z) \sum'_x(z) \sum'_y(z)} = \frac{photons}{s \cdot mm^2 \cdot mrad^2 \cdot 0.1\,\%} \tag{2.7}$$

with z the coordinate along the particle beam propagation.

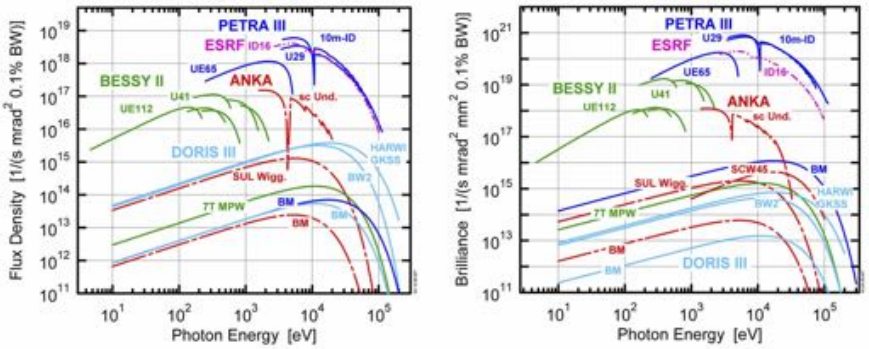

Figure 2.6: Comparison of flux density and brilliance of different accelerator facilities. Adapted from [14].

Polarisation An important property of synchrotron radiation with respect to X-ray fluorescence spectroscopy is its linear polarisation in the particle orbit plane while outside of this plane the synchrotron light is elliptically polarised. Polarisation degrees in the orbit plane of nearly $100\,\%$ can be

achieved at 3rd generation synchrotron facilities. This high degree of polarisation minimises scattering effects when detecting radiation perpendicularly to the primary photon beam in the plane of linear polarisation (i.e. in the horizontal plane).

Coherence Coherence is a fundamental property of a radiation source. Synchrotron radiation sources and free electron lasers(FELs) posses a certain degree of coherence. The quantitative description of partial coherence is given by the so-called mutual coherence function[15]. Two classes of coherence are defined, longitudinal and transverse coherence. Longitudinal coherence, also referred to as temporal coherence, specifies the extent to which the radiation maintains a definite phase relationship at two different times and is characterised by the coherence time. The longitudinal coherence is expressed using the following equation:

$$C_l = \frac{\lambda^2}{2\Delta\lambda} \tag{2.8}$$

with λ the wavelength of the X-ray beam and $\Delta\lambda$ the maximal difference in wavelength between two photons. Transverse coherence on the other hand, also referred to as spatial coherence, describes the degree to which the phase of the wave is correlated at two distinct point in the transverse plane:

$$C_t = \frac{\lambda L}{2\sigma} \tag{2.9}$$

with L the source object distance, and σ the source spot size. For a high coherence beamline, like ID19 at the ESRF, the coherence is of the following order of magnitude: $C_l = 0.5\,\mu\mathrm{m}$ and $C_t = 100\,\mu\mathrm{m}$ vertically.

Time Structure synchrotron radiation (SR) can also be used for time resolved experiments due to the time structure of the X-ray pulses originating from the electron bunches in the storage ring. The filling mode of the storage ring will determine the timing mode since it determines how many electron bunches will be used and what the spacing between each bunch is. However, the filling mode does not only determine the timing mode of the storage ring but it also determines the maximum usable current and thus flux of the storage ring. Therefore, several filling modes have been made available to satisfy the different needs of the experimentalists, Table 2.3. When the highest flux is needed, the storage ring will be filled uniformly, equally distributing the bunches over the entire circumference of the storage ring. Lower bunch modes, like 16 bunch mode (ESRF) yield a lower

flux, since the maximum current is lower, but yield a different time structure. Besides these pure filling modes, one also has hybrid filling modes which combine a time resolved characteristic with a high flux. One of the hybrid filling modes available at the ESRF is the 24*8 + 1 filling mode. When this filling mode is operational, the storage ring is filled with $196\,\mathrm{mA}$ multi-bunch beam which is composed of 24 bunch groups spread over ¾ of the circumference. A clean $4\,\mathrm{mA}$ single bunch is positioned exactly in the centre of the remain quarter of the storage ring. The pulse length is typically in the range of 40 to $400\,\mathrm{ps}$ depending on the filling mode[16–18].

ESRF				
Filling pattern	Uniform	Hybrid 24*8 + 1	16 bunch	4*10
Current (mA)	200	196 + 4	90	40
Bunches	996	24 + 1	16	4
Lifetime	60	40	10	6
Petra III				
Filling pattern	Multi bunch	Single bunch		
Current (mA)	100	100	80	
Bunches	960	60	40	
Lifetime	24		2	

Table 2.3: Common filling modes at the ESRF and Petra III and their properties. Source: ESRF and Petra III

2.2.2 Generation of Synchrotron Radiation

2.2.2.1 Bending Magnets

Bending magnets are mandatory components of a synchrotron, since they enable the closed orbit operation of the storage ring. Besides their role as e^-/e^+ guide to define a closed orbit, they can also serve as sources of synchrotron radiation, as they generate a smooth continuous emission spectrum ranging up to several tens of keV, see Figure 2.7. For practical purposes, many synchrotrons are based on the use of permanent magnets, ESRF, $0.85\,\mathrm{T}$ / Petra III, $0.872\,\mathrm{T}$, which yield a critical energy (E_c) of 19.2 and $20.9\,\mathrm{keV}$ respectively at the machine energy of $6\,\mathrm{GeV}$. The critical energy (E_c) divides the bending magnet emission spectrum into two equal

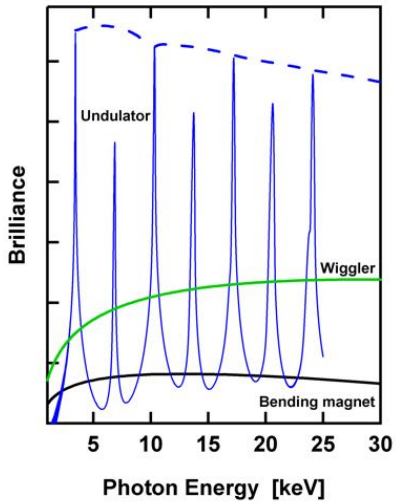

Figure 2.7: Schematic comparison of the brilliance as a function of photon energy for a bending magnet, multipole wiggler, and an undulator source. Reproduced from Photon Science, 2009.

halves in terms of radiative power and is expressed as follows:

$$E_c(keV) = 0.665 \cdot E^2(GeV) \cdot B(T) \tag{2.10}$$

where E is the electron energy and B the magnetic field flux. The total irradiated power (Figure 2.6 and 2.7) can be calculated using equation 2.11.

$$P_{tot}(kW) = 26.6 \cdot E^3(GeV) \cdot B(T) \cdot I(A) \tag{2.11}$$

The photon beam generated by a relativistic electron can be described as a narrow cone of radiation originating from the point of emission, characterised by the emission angle equal to $\frac{1}{\gamma}$ around the critical energy.

2.2.3 Insertion Devices

Insertion devices (IDs) are an assembly of alternating magnetic pole elements, which are inserted in the straight sections of the storage ring, deflecting the beam periodically in opposite directions. The distance between identical magnetic element poles is called the period (λ_p) of the ID. The main advantage of using IDs is the increased total emitted flux due to the many undulations of the e^--beam in the alternating magnetic field of the

IDs. In contrast to BMs, IDs can vary their magnetic field values by changing the gap between the magnetic poles, enabling a large spectral range and tuneability (Figure 2.7). This makes them ideal to optimally meet the needs of the experimentalist by tuning the radiation characteristics. Therefore, IDs are not described by their magnetic field, like in the case of BMs, but using their remanent field $\mathrm{B_r}\,(\mathrm{T})$. The main insertion devices (IDs) are the wavelength shifter, the multipole wiggler, and the undulator. Only the latter two will be described here since they are most frequently used.

2.2.3.1 Multipole Wigglers

Wigglers are IDs which induce fairly large deviations of the electron beam from their reference trajectory. Since wigglers are an assembly of alternating magnetic elements they influence the e^--beam like a series of BMs whom generate incoherent photons, see Figure 2.8. Thus, the total intensity generated by N poles, separated by the period λ_p, is equal to that of 2N inline bending magnets (BMs), see Figure 2.7. IDs are characterised by

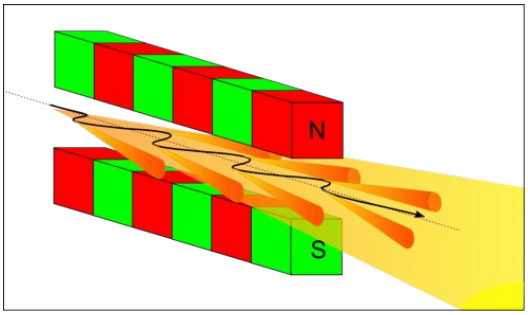

Figure 2.8: Schematic depiction of the radiation emitted by a wiggler (not to scale). Adapted from [14].

deflection parameter (K) which is defined as the maximum deflection angle in comparison to the reference trajectory.

$$K = \gamma \cdot \vartheta = \frac{[c] \cdot e \cdot B_0}{m \cdot c^2} \cdot \frac{\lambda_p}{2\pi} = 0.934 \cdot B_0 \cdot \lambda_p(cm) \tag{2.12}$$

Generally, an ID is called a wiggler when the deflection parameter is much larger than one ($K \gg 1$) and the following condition is met:

$$\int_{-\infty}^{+\infty} B_y(y = 0, z)dz = 0 \tag{2.13}$$

The magnets used in wigglers can be of electromagnetic or permanent magnet type. Electromagnetic magnet based wigglers can reach high magnetic

field strengths but are used less frequently due to the bulkiness of the coils, therefore limiting the period. It is obvious that the magnetic field strength can be easily varied when using electromagnets but this is also possible using permanent magnets, although less obvious. By mechanically varying the gap between the permanent magnet poles, the magnetic field strength changes. The remanent field does not only depend on the type of magnet used and the gap (g) but also on the period, as shown in Equation 2.14.

$$B_r(T) \approx 3.33 \exp\left[-\frac{g}{\lambda_p}\left(5.47 - 1.8 \cdot \frac{g}{\lambda_p}\right)\right] \tag{2.14}$$

$$\text{for } 0.1\,\lambda_\mathrm{p} \lessapprox \mathrm{g} \lessapprox 10\,\lambda_\mathrm{p} \tag{2.15}$$

One can immediately see that the remanent field strength drops off dramatically once the gap becomes of the order of the period length or greater. On the other hand, when closing the gap, significant field strengths can be obtained. This effect is shown in Figure 2.9. Therefore, it is important to

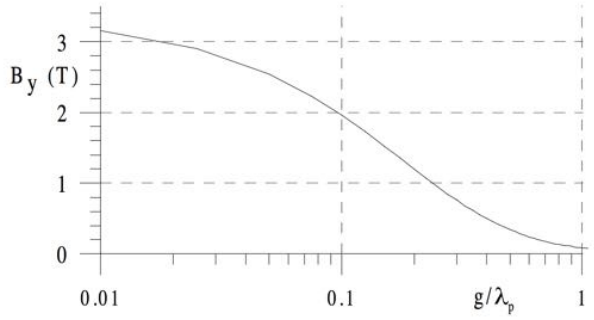

Figure 2.9: The influence of the gap aperture on the on-axis field strength in a wiggler[13].

install wigglers at a location where the beam dimension normal to the deflection plane is small, which are located at the low β sections of the storage ring. The total radiation power can be calculated as follows[19]:

$$P_\gamma(W) = \frac{1}{3} r_c m c^2 c \gamma^2 K^2 \frac{4\pi^2}{\lambda_p^2} = 632.7 E^2 B_0^2 I N_p \lambda_p \tag{2.16}$$

where I is the e^--beam current, and N_p the number of periods of the wiggler in question.

2.2.3.2 Undulators

The main difference between an undulator and the previously explained wiggler is that in the case of an undulator the deflection parameter K is smaller than 1 and consists out of a larger number of poles, see Figure 2.10. Since the deflection parameter is small, the on-axis deviations of the e^--

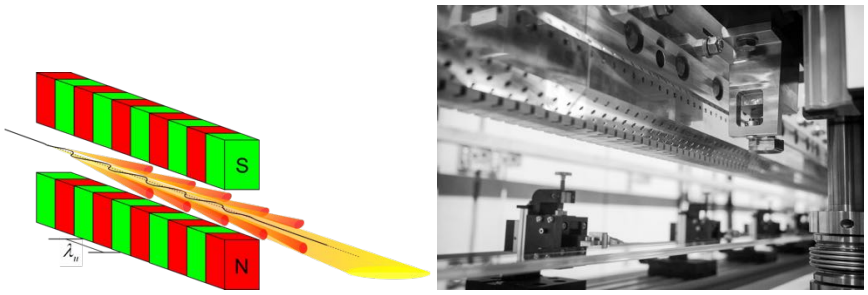

(a) *(b)*

Figure 2.10: ***(a)*** *Schematic depiction of the radiation emitted by an undulator (not to scale) (Adapted from [14]).* ***(b)*** *A photograph an opened undulator.*

beam are small but frequent due to the large number of magnetic poles. Therefore, the emission cones from the whole trajectory overlap, enabling the emitted photons to constructively interfere at certain wavelength/energy values (harmonics), proportional to N_p^2. Due to this interference effect, the obtained spectrum is not as broad as of a bending magnet (BM) or a wiggler but exhibits well-defined maxima at specific energies, undulator harmonics, corresponding to the periodicity of the photon emission in the time domain (Figure 2.7). For an undulator with period λ_p, and deflection parameter K, at an angle θ off the undulator axis is given by:

$$E_i(\theta) = \frac{2i\gamma^2}{\lambda_p}\left(1 + \frac{K^2}{2} + \gamma^2\theta^2\right)^{-1}, \text{ i = 1, 2, 3, ...} \tag{2.17}$$

where i is the harmonic number.

2.3 Photon Matter Interactions

This chapter describes the principles of photon-matter interactions on which XRF analysis are based. X-rays is a term commonly used for electromagnetic radiation with an energy between 0.1 and 100 keV. The elementary particle which represents a quantum of electromagnetic radiation is called

a photon and may interact with matter in a variety of ways. The processes, relevant in the energy range used in the experiments described in this manuscript, (1 - 100 keV), are photoelectric effect, Rayleigh and Compton scattering. The likelihood of these processes to occur is quantified by the interaction cross sections (σ).

2.3.1 Photoelectric effect

This type of interaction can only occur when the energy of the incident X-ray photon E_{ph} is higher than the binding energy of the electron E_{ion}. The processes involves the transfer of the photon energy to one of the core electrons of an atom, resulting in its ejection from the atom. The ejected electron, called photo-electron, has a kinetic energy equal to the difference in energy between the incident X-ray photon and electron binding energy. The photoelectric effect cross section (τ), sometimes referred to as the photoionisation cross section, is a function of the atomic number (Z) and the incident photon energy (E) and can be approximated using:

$$\tau \approx C\frac{Z^4}{E^3} \tag{2.18}$$

with constant C.

2.3.2 Rayleigh Scattering

An X-ray photon passing through matter has a certain chance to interact with the electrons, which are bound to the nucleus. If the result of such an interaction is a change in the propagation direction without a change in photon energy, one calls this interaction elastic scatter or Rayleigh scattering. The Thomson scattering phenomenon, which describes photon / free electron interactions, is the basis for the expression describing the microscopic Rayleigh scattering cross section[2].

$$\sigma_T = r_e^2\left(1 - \sin^2(\theta)\cos^2(\phi)\right) \tag{2.19}$$

with r_e the classical electron radius, scattering angle θ, and azimuthal angle ϕ (Figure 2.11). However, the observed scattering effect is the superposition of all scattering interaction with electrons and thus coherent but not in phase since not every photon - electron interaction happens at the same position. The atomic form factor F(Z,E) describes the influence of the spatial distribution of the electrons in the atom and is equal to the Fourier transform of the electron density $\rho(\mathbf{r})$ of the atom[2]:

$$F(Z,E) = \int \rho(\mathbf{r})e^{i\mathbf{Q}r}d^3\mathbf{r} \tag{2.20}$$

Q represents the energy-dependent momentum transfer between photon and electron. The Rayleigh cross section σ_R is expressed as the product of the Thompson cross section and the square of the atomic form factor[2].

$$\frac{\mathrm{d}\sigma_R}{\mathrm{d}\Omega} = \frac{\mathrm{d}\sigma_T}{\mathrm{d}\Omega} \cdot F^2(Z,E) = r_e^2 \left(1 - \sin^2(\theta)\cos^2(\phi)\right) F^2(Z,E) \quad (2.21)$$

with F(Z,E) the atomic form factor and $\frac{\mathrm{d}\sigma_T}{\mathrm{d}\Omega}$ the Thompson differential scattering cross section. The atomic form factor takes the phase difference between the waves scattered by the electrons in the atom into account. It is maximal for scattering in the forward direction and proportional to Z^2[20]. The anisotropic nature of the angular distribution of Rayleigh scattering is determined by the degree of polarisation of the photon and by its energy. Figure 2.12 shows the Rayleigh differential cross section as a function of the scattering angle and the azimuth angle for two different energies. The Rayleigh scattering cross section is the highest at low photon energies and decreases with increasing energies or for lighter elements, as shown in Figure 2.19.

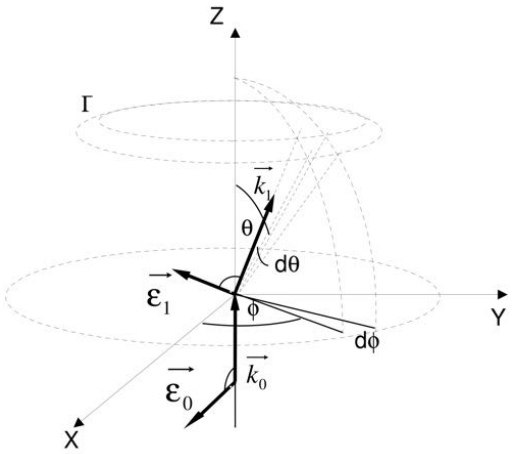

Figure 2.11: Coordinate system for scattering interactions. Adapted from [21].

2.3.3 Compton Scattering

Photons with a high enough energy have the potential to be scattered by a free electron transferring part of its energy to the electron and, at the same time, change its propagation direction. This type of scattering is called inelastic or Compton scattering, after the discovery by Arthur Compton.

After this interaction the energy of the photon can be calculated by using the Compton equation:

$$E_C = \frac{E_0}{1 + \frac{E_0}{m_e c^2}(1 - \cos\theta)} \tag{2.22}$$

where E_0 is the incident photon energy, m_e the electron rest mass, and θ the scattering angle. The change in energy is a function of the scattering but is independent of the incident photon energy, as well as the scattering atom. The shape of the Compton peak in an XRF spectrum is in general broader, with an exponential tail on the lower energy side, than a characteristic elemental line due to the relative motions of the electrons involved, causing a Doppler broadening of the peak which can be described as follows[22]:

$$4\beta\lambda \sin\left(\frac{\theta}{2}\right) \tag{2.23}$$

with $\beta = \frac{v}{c}$ for electrons moving in a random direction with the velocity v. In case of polarised monochromatic radiation, the angle dependent probability for Compton scattering can be described by the differential cross section[23]:

$$\frac{\mathrm{d}\sigma_C}{\mathrm{d}\Omega} = \frac{\mathrm{d}\sigma_{KN}}{\mathrm{d}\Omega} S(q, Z) \tag{2.24}$$

$$= \frac{r_e^2}{2}\left(\frac{K}{K_0}\right)^2 \left(\frac{K}{K_0} + \frac{K_0}{K} - 2\sin^2(\theta)\cos^2(\phi)\right) S(q, Z) \tag{2.25}$$

with $S(q, Z)$ the incoherent scattering function, q the momentum transfer, $d\sigma_{KN}/d\Omega$ the Klein-Nishina differential scattering cross section, r_e the classical electron radius and

$$\frac{K}{K_0} = 1 + \frac{E}{m_e c^2}(1 - \cos(\theta)) \tag{2.26}$$

where θ is the scattering angle and ϕ the angle between the electric field vector of the incoming photon and the scattered photon, see Figure 2.11. Figure 2.12 shows the Compton differential cross section as a function of the scattering angle and the azimuth angle for two different energies. The quantity $\frac{K}{K_0}$ determines the ratio of the photon energy E before and after the Compton scattering interaction. The incoherent scattering function accounts for the phase difference between the waves scattered by the electrons in the atom and the fact that not all electrons are bound equally to the atom core.

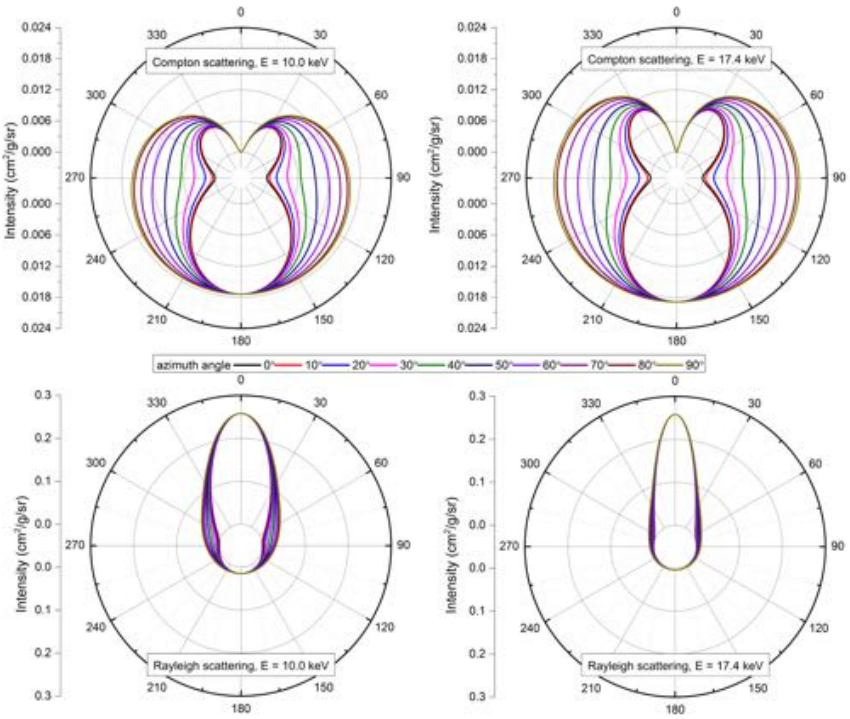

Figure 2.12: Compton and Rayleigh differential cross sections for polarised radiation as a function of scattering and azimuth angle for two different energies. Produced using Xraylib.

2.3.4 Attenuation

The term attenuation is defined as the reduction of the X-ray intensity as a result of the x-rays passing through an object. The physical processes responsible for the attenuation are absorption as well as scattering. Absorption may be induced by photoelectron absorption or by electron-positron pair production. Scattering processes may be Rayleigh or Compton scattering. Attenuation is quantitatively described by the linear attenuation coefficient (μ) and the Lambert Beer law (Eq. 2.27). In addition to the linear attenuation coefficient, the mass attenuation coefficient $\frac{\mu}{\rho}$ is defined and often used in databases like xraylib[24].

$$I_{\Delta z}(x,y) = I_0(x,y) \cdot \mathrm{e}^{-\int_{z=0}^{\Delta z} \mu(x,y,z)dz} \tag{2.27}$$

With the assumption that the individual processes, described earlier, contribute to the overall attenuation independently from each other, the total

attenuation coefficient μ can than be written as a sum of the attenuation coefficients of the individual contributors:

$$\mu(E) = \sum_{i=1}^{n} (w_i \sigma_{rayleigh}(Z, E) + w_i \sigma_{compton}(Z, E) + w_i \sigma_{photo}(Z, E)) \tag{2.28}$$

with the attenuating sample consisting of n elements, each with a weight fraction w_i.

2.3.5 X-ray Fluorescence

While Compton and Rayleigh scattering provide an estimate of the illuminated mass and the mean atomic number of the sample matrix, the photoelectric effect has the potential to provide qualitative and quantitative information on the elemental composition, oxidation state and coordination of the sample in question[23, 25]. This information is obtained through the emission of characteristic X-ray photons, called X-ray fluorescence, which originate from an electron transition from a higher shell electron to the created vacancy by the photoelectric effect[2]. The emitted characteristic fluorescent photon has an energy equal to the difference in binding energy of the atomic shells involved in the electron transition. The emission of fluorescent photons is however in competition with a phenomenon referred to as the Auger effect, where the fluorescent photon is absorbed by another electron of the atom before leaving the atom. The Auger effect is thus characterised by the emission of an Auger electron and the creation of an extra electron vacancy. A special case of the Auger effect comprises of the Auger effect on the subshell level and form an important relaxation mechanism in atoms with shells having subshells, such as L and M shells. Via so-called Koster-Crönig transitions, the initial excitation of an L_1 shell may lead to the transition of an electron of the L_2 or L_3 subshells due to their lower binding energies. If the transition is non-radiative, the resulting L_1L_2 or L_1L_3 Auger electron may be absorbed in one of the shells having a lower binding energy, such as the M shell. The thus created L_2 or L_3 vacancy can in turn cause a radiative transition. The likelihood of the emission of a fluorescent photon after photoionisation is expressed using the fluorescent yield factor ω which is dimensionless and dependent on the atom and the excited shell. The cross section associated with X-ray fluorescence is called the XRF production cross section Q, which is equal to the result of the multiplication of all the phenomena involved with fluorescent photon emission, being the partial photoionisation cross section (τ), fluorescent yield (ω), and radiative rate F. The radiative rate is defined as the fraction

of radiative transitions that lead to the production of a fluorescent photon with a particular energy. For the $KL3$ electron transition the expression for the XRF production cross section is as follows:

$$Q_{KL3}(Z,E) = \tau_K(Z,E)\omega(Z)F_{KL3}(Z) \tag{2.29}$$

2.3.6 Pair Production

At higher energies than $1.022\,\mathrm{MeV}$, twice the rest mass energy of an electron, the interaction of a photon with a nucleus can cause the creation of an electron-positron pair, which is called pair production. Since the energy needed for this interaction is higher than what falls within the scope of this thesis, it will not be discussed further.

2.4 X-ray optics

The fact that the refractive index of X-rays differ only slightly from one ($\delta \approx 10^{-5}$) and the high absorption of the photons in the lens material, makes focussing of X-rays using refraction based optics a challenge. On the other hand, optics based on mirrors are only efficient when they operate in external total reflection mode, i.e., having an angle of incidence below the critical angle of total reflection ($\theta_c = \sqrt{2\delta} < 1^\circ$). Despite these difficulties, refractive lenses (compound parabolic refractive lenses, nano focussing lenses) and mirror optics (Kirkpatrick-Baez mirrors) have been developed and successfully implemented[26, 27]. Other available optics used in X-ray focussing are: capillary optics, bent crystals, waveguides, Fresnel zone plates, multilevel zone plates, multilayer laue lenses, Bragg-Fresnel optics, and photon sieves[28–32]. Due to the scope of this work only a few focussing optics will be explained.

2.4.1 Kirkpatrick-Baez Mirrors

Conventional mirrors, as used for visible light, at normal incidence angles can not be used because the reflectivity of photons in the hard X-ray regime is too low. However, a high reflectivity can be obtained at grazing incidence angles $\left(\theta < \sqrt{2\delta}\right)$. To reduce astigmatism, Kirkpatrick and Baez proposed the use of the spherical or cylindrical mirrors in a crossed configuration[26]. Figure 2.13 shows the geometrical arrangement of a Kirkpatrick-Baez (KB) mirror system. In some systems, the numerical aperture is further enhanced by the use of multilayer coated mirrors. These mirrors are build by evaporating or sputtering alternating layers with a relatively high refractive index

and a relatively low refractive index. The rays reflected at the interfaces of the multilayers are superimposed coherently and in phase, which gives a considerable increase in photon flux. Technological advances in surface preparation/treatment have made it possible to achieve focal spot sizes in the range of several nm[33, 34]. As, within a given energy interval, the optical properties for total reflecting optics are independent of the photon energy, making them ideal for spectroscopy experiments while maintaining the focal size constant. KB systems can either be static, with mirrors polished to a predefined shape optimised for a given incidence angle and focus, or can be dynamic with actuators bending flat mirrors into the shape which is required by the experiment. Although the dynamic systems, for example used at the ESRF, are the most versatile, they also require the most time to achieve an optimised system since bending the mirrors to form an exact ellipse is a complicated procedure. Secondly, the mirror surfaces of dynamic systems show more imperfections in comparison to fixed curvature systems. Exactly for this reason, institutes like DESY, Spring8 and APS and later also the ESRF opted to use KB systems with a fixed curvature[33, 35, 36].

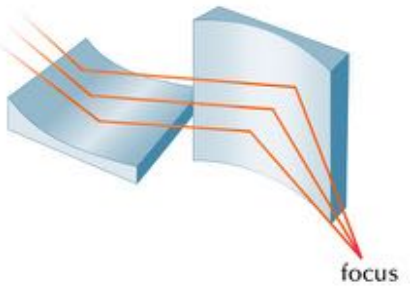

Figure 2.13: Schematic view of the two-mirror Kirkpatrick-Baez system. Image adopted from [37].

2.4.2 Capillary Optics

Capillary optics are based on the transportation of photons by total external reflection on the inner walls of hollow glass capillaries[38]. Total external reflection is possible when the incoming angle of the photon in comparison to the capillary wall is smaller than the critical angle θ_c and that the surface is smooth enough to enable reflections with a high reflection coefficient. The critical angle of total reflection $\theta_{\mathrm{c}}\,\mathrm{mrad}$ can be approximated using the

following formula:

$$\theta_c = \frac{0.02\sqrt{\rho}}{E} \tag{2.30}$$

with ρ the density of the reflecting material in $\frac{g}{cm^{-3}}$ and E the photon energy in keV. The simplest capillary used as an X-ray optic is a straight cylindrical monocapillary. From the moment that the first reflection can take place ($\theta < \theta_c$), all consecutive reflections will be able to occur due to the axial symmetry of cylindrical capillaries. Since most X-ray sources produce divergent X-ray beams, their intensity drops with the inverse square of the distance, one can gain a considerable amount of flux at the sample position when using capillary optics to transport X-ray radiation. The angular aperture of a capillary is $2\theta_c$ while for a pinhole this is equal to $\frac{d}{R}$. Therefore, the intensity gain, in comparison to a pinhole optic, can be expressed using the following equation[39]:

$$gain \approx \left(\frac{2\theta_c R}{d}\right)^2 \tag{2.31}$$

where R is the is the source-capillary distance, and d the capillary diameter. The spot size at sample distance s_2 can be estimated using:

$$s_2 \approx d + 2\theta_c F_2 \tag{2.32}$$

where F_2 is equal to the capillary-sample distance. As is clear from equation 2.31 and 2.32, if one wants to obtain smaller spot sizes in the sample plane, the flux obtained at the sample distance will become less. In contrast to straight capillaries, bent capillaries do not only transport radiation but also guide it into a certain direction, which can be used to focus X-rays. For bent capillaries however there is an extra parameter that determines the efficiency, and that is the radius of curvature. If radius of curvature becomes too small in comparison to the diameter of the capillary, part of the photons coming from a quasi parallel photon beam will not meet the $\theta < \theta_c$ criterion. This is expressed by the following equation[40]:

$$\gamma \equiv \frac{r\theta_c^2}{2d} \geq 1 \tag{2.33}$$

where r is the curvature radius. γ decreases fast with an increase of the photon energy since $\theta_c^2 \sim E^{-2}$, causing the low transmission efficiency for high energy photons. Polycapillary optics consist of thousands of bundled mono capillaries with different curvature (see Figure 2.14), which define the characteristics of the polycapillary in question, and were first proposed in 1986[41]. Two main categories can be defined to group the different

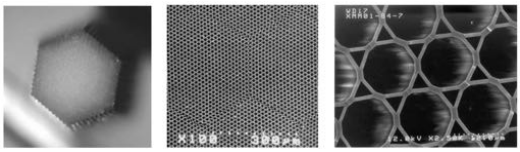

Figure 2.14: Photograph and SEM images of a polycapillary optic, showing the stacking of the individual mono capillaries and their typical size. Adapted from [42].

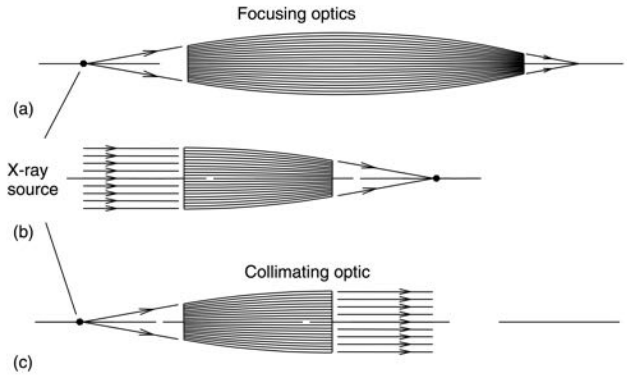

Figure 2.15: Polycapillary X-ray optics that produce a focused (a,b) or parallel beam (c), starting from a X-ray point source (micro-focus X-ray tube (a, c)) or a quasi-parallel X-ray source (synchrotron (b)). (a) Is referred to as a Full Lens while (b) and (c) are referred to as Half Lenses. Adapted from [42].

optics, full lenses and half lenses, shown in Figure 2.15. Polycapillary full lenses collect radiation from a focal point and focuses the photons in another focal spot of a different size. The relation between the two focal sizes is given by:

$$\frac{\Delta s_2}{\Delta s_1} = \frac{F_2}{F_1} \tag{2.34}$$

Half lenses transform a divergent beam into a parallel beam or focus a parallel beam into a focal spot. As shown using Formula 2.32 and 2.34, one can theoretically determine the spot sizes of a capillary optic, however one often needs to determine the obtained spot size experimentally. The measurement procedure to determine the focal spot size of an X-ray focusing system is non trivial. There are different methods available, with advantages and disadvantages. Several groups used the method of a knife edge[42]. This method provides a high spatial resolution. However, one should apply this method with caution when using a high intensity collimated beam as one does not obtain a two-dimensional intensity distribution in the focal plane. Other often used methods are a wire scan of known thickness or a 2D scan by a pinhole optic. In case of the wire scan, the obtained curve represents the convolution of the wire thickness and the beam size. The latter can thus be estimated as follows:

$$s \approx \sqrt{s_m^2 - d_w^2} \tag{2.35}$$

where s_m is the FWHM of the Gaussian that represents the measurement and d_w the diameter of the wire.

2.4.3 Doubly Curved Crystal Optics

Unlike the two previously described X-ray optics, DCC optics are based on Bragg diffraction and provide a monochromatic beam (apart from the higher diffraction orders). For this reason, they are often referred to as monochromatic X-ray optics. DCC optics were only systematically studied in the 1980s and 1990s using ray tracing methods for their fabrication and application[43–45]. However, their widespread use as primary optic for monochromatic beam applications were impeded by the difficult production process. The point-to-point focusing geometry of a DCC optics is shown in Figure 2.16. In this geometry, the diffracting planes of the crystal remain parallel to the curved crystal surface. The crystal surface, which has a toroidal shape, has the Johann geometry in the focal circle plane and axial symmetry in the perpendicular direction[46]. In the case of a toroidally curved crystal, the bending radius of the crystal perpendicular to the Rowland circle is (cfr. Figure 2.16):

$$R_V = 2R \sin^2 \theta_B \tag{2.36}$$

This geometry provides point-to-point focusing on the Rowland circle, in Figure 2.16 imaging the source spot S onto the image spot I. The ability

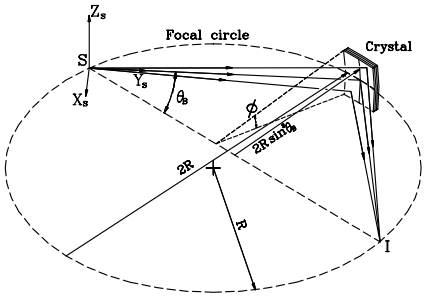

Figure 2.16: Point-to-point focusing geometry of a doubly curved crystal optic (DCC). Adapted from [47].

to obtain high monochromatic X-ray fluxes from even low-power compact X-ray sources is possible due to the large collection solid angle of a DCC optic. The collection solid angle of a DCC optic is determined by the capture angle in the dispersive plane and the included rotational angle ϕ. To increase the obtained intensity, multiple crystals can be used, effectively enlarging the collection solid angle (Figure 2.17). The used geometry, also referred to as the Johann geometry, requires the optics to be placed non-symmetrically on the Rowland circle, making it necessary to tilt the crystal planes with respect to the crystal surface by γ, see Figure 2.18. This type of DCC optics was used in case of our self-developed laboratory micro-XRF setup (see Chapter 7).

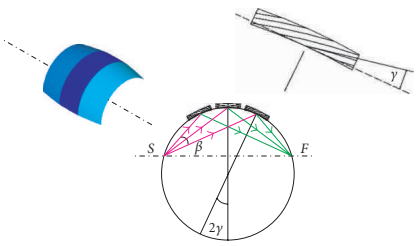

Figure 2.17: Illustration of the use of multiple DCC crystals to increase the obtained monochromatic photon flux at the focal spot[47].

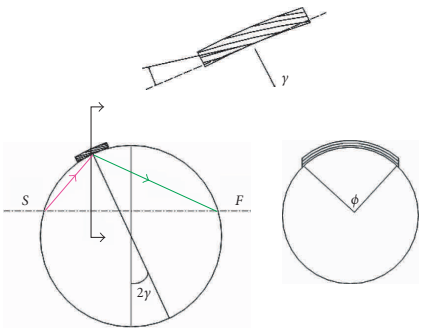

Figure 2.18: Asymmetric placement of DCC crystals[47].

2.4.4 Monochromators

Experiments at 3rd generation synchrotron sources are often performed using monochromatic X-rays for a variety of reasons. The monochromatic X-ray beams are mostly obtained by making use of monochromator crystals. Although multiple types of monochromators exist, most are based on the diffraction principles. Bragg's law, Eq. 2.37, describes the relation between the crystal angle θ and the selected wavelength λ

$$2d \sin\theta = n\lambda \tag{2.37}$$

$$E(keV) = \frac{12.39}{\lambda(\text{Å})} \tag{2.38}$$

with d the crystal lattice spacing which determines the energy resolution and the energy working range of the crystal. Therefore, depending on the application or the general purpose of the beamline, different crystals can be installed, e.g. Si(111) and Si(311), providing monochromatic X-ray beams with an energy resolution in the order of $\frac{\delta E}{E} = 10^{-4}$.

Two general designs are used, channel cut monochromator (CCM) and double crystal monochromator (DCM), the former being a monocrystal with a channel cut through, thus having the advantage of being very compact with simple mechanical controls causing it to be very stable but having a variable offset depending on the photon energy. A DCM on the other hand has a fixed offset, when properly calibrated, and the ability to steer the X-ray beam by utilising 2 independent crystals, making it more complex and more prone to vibrations. Since it utilises 2 independent crystals it also allows to suppress the higher orders by slightly detuning the second crystal which results in a lower flux since one is working on a slope of the rocking curve.

Some experiments, like emission experiments, do not require X-ray beam with a high energy resolution but can benefit from a higher flux than what is achievable with perfect crystal monochromators. Therefore, monochromators were designed that offer a wider energy bandwidth, typically in the order of $\frac{\delta E}{E} = 10^{-2}$, with an increase in flux of 30-100×. These multilayer monochromators are based on synthetic multilayer structures, consisting of alternating of high and low density layers, grown on top of a Si substrate[48]. The double multilayer monochromator installed at the Hard X-ray Micro/Nano Probe P06, Petra III has 3 different multilayer stripes, Pd/B_4C, Ni/C, and Ir. The Ir stripe is used for total reflection with a high reflectivity ($\geq 80\,\%$) in the $[5-20]\,\mathrm{keV}$, the Ni/C stripe can be used with high reflectivity in the $[5-8]\,\mathrm{keV}$ and $[15-90]\,\mathrm{keV}$ range, while the Pd/B_4C stripe can be used with high reflectivity in the $[12-24]\,\mathrm{keV}$ and $[36-90]\,\mathrm{keV}$ range.

2.5 X-ray detection

The discovery of X-rays was based on the observation of visible fluorescence from a barium platinocyanide screen positioned well away from the Crookes - tube Wilhem Contrad Röntgen was using. In fact, this barium platinocyanide screen can be regarded as the first X-ray detector. Soon after that, the discovery was made that also photographic plates and ionisation chambers were sensitive to X-rays[49]. The primary interaction of X-rays in the detector material is mainly determined by the photoelectric effect, Compton scattering, and Rayleigh scattering. For the energy range discussed in this manuscript, the photoelectric effect is dominant, see Figure 2.19. The photon energy is converted in the detector material by the photon-matter interaction to an electrical signal via an indirect or direct process. A straightforward way to detect X-rays is to use an ionisation chamber, which consist of a compartment filled with gas on which an electric field is applied. X-rays passing through the chamber will ionise the gas which will cause a measurable current by a galvanometer. Ionisation chambers are widely used due to their uniform response to radiation over a wide range of energies but only provide data on the X-ray intensity and not on their energy. The main downside of gas type detectors is their low efficiency inherent of the low density of gas. An alternative with a much higher detection efficiency for high energy photons is the scintillation detector, which couples a scintillating material to photo multipliers, photodiodes or CCDs for the detection of fluorescent light. These detectors can be made very small and with a high efficiency for high energy photons when coupled with scintillating crystals made of heavy elements. The combination of a

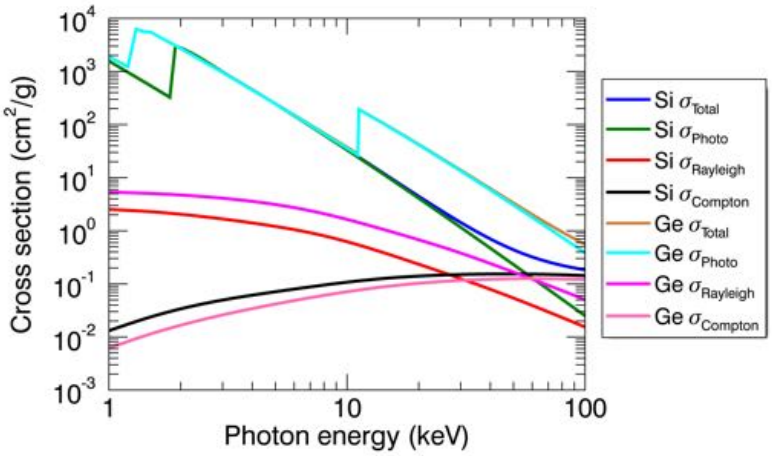

Figure 2.19: Total, Rayleigh, Compton, and photoionisation cross sections for Si and Ge. Obtained via xraylib.

large scintillating material with a large number of light detectors, one can create a high-efficiency detector which can be used for, e.g. medical applications. Due to the continuous technological advances, these detectors become faster and provide improved energy resolution, however, the latter is still one of the disadvantages of this type of detector.

2.5.1 Si(Li) and HPGe detectors

In the 1960s, shortly after high purity Si and Ge single crystals became available, the first Si(Li) and Ge(Li) detectors were developed, offering a much higher energy resolution than the other detector types available at that time. The reason of this leap forward in energy resolution is based on the fact that the mean energy needed to create one primary elementary charge in a semiconductor material is only a few eV while for gases this is about 20 to $30\,\mathrm{eV}$. In a single crystal of a semiconductor material, such as Si or Ge, the sharply defined atomic electron states are broadened into bands of energy state, the valence band and the conduction band, see Figure 2.20. An electron can be promoted from the valence band to the conduction band if it receives an energy at least equal to that of the band gap, 1.12 and $0.74\,\mathrm{eV}$ for Si and Ge respectively. Once promoted to the conduction band, the electron can move under the influence of an externally applied electrical field and can be collected at an electrode. The holes, which are left in the valence band, can also be moved by the applied field in the opposite direction of the electrons. The speed at which electrons and holes migrate through a crystal

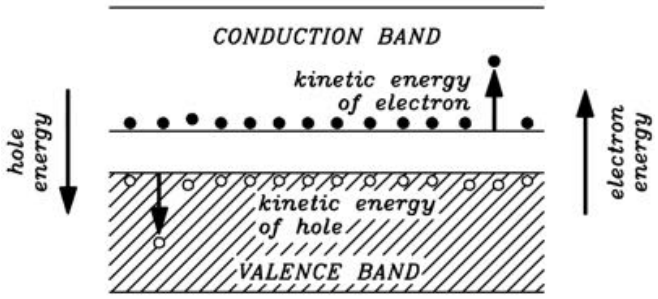

Figure 2.20: Showing potential and kinetic energy of electrons and holes in the valence and conduction band. Figure from [50].

are different, e.g. $1450\,\mathrm{cm^2V^{-1}s^{-1}}$ for electrons and $505\,\mathrm{cm^2V^{-1}s^{-1}}$ for holes in Si at room temperature[51]. When an X-ray photon interacts in a semiconductor crystal, the primary photoelectron created by the ionisation process excites bound electrons to the conduction band. These secondary electrons, if sufficiently energetic, can further create additional electrons by a cascading process which finally leads to a large number of electron-hole pairs that can be collected at the electrodes of the device.

The basic principle of a Si diode detector is based on a junction between two p and n semiconductor materials. When the pn-diode is reverse biased, the bulk material is depleted from the free charge and the carriers produced by the interaction of photons with the bulk material can be collected by the electrodes by means of the applied electric field. A dark current, which is thermally generated within the bulk material, is also collected by the electrodes and contributes to the statistical spread in the measurement of the signal charge. However, the contribution of dark current can be greatly reduced by suitably cooling the detector chip. The depletion depth, determined by the applied bias, is for Si based pn-detectors usually limited to $1\,\mathrm{mm}$. However, the depletion depth is heavily influenced by dopants like Li and making depletion depths of several millimetres possible. Lithium drifted silicon detectors Si(Li), lithium ions, which act as a donor, are driven through a large volume of a high purity silicon crystal which tends to be p-type, in order to keep an intrinsic like bulk material by means of the compensation of the donors and acceptors impurities concentration. The excess lithium on the surface of deposition on the crystal results in a highly doped n+ layer which acts as an electrical contact, while the uncompensated p region on the opposite side is equipped with either a metallic contact or a thin p+ layer. At room temperature, the lithium continues to drift significantly, which should be avoided at all times. Therefore, it needs to be

cooled, usually with liquid nitrogen (LN2), to avoid the redistribution of the Li ions. The Si(Li) detector has long been the most popular detector for X-rays up to $40\,\mathrm{keV}$ with a typical energy resolution of about $135\,\mathrm{eV}$ at $5.9\,\mathrm{keV}$.

For the higher energy photons, high purity germanium (HPGe) detectors are used since Ge offers a better detection efficiency at these higher energies due to its higher density ($2.33\,\frac{\mathrm{g}}{\mathrm{cm}^3}$ Si / $5.46\,\frac{\mathrm{g}}{\mathrm{cm}^3}$ Ge) and larger ionisation cross section due to its higher atomic number. HPGe detectors also offer a better statistical energy resolution since the mean energy required for an electron-hole pair generation ($2.96\,\mathrm{eV}$ Ge / $3.62\,\mathrm{eV}$ Si) and the fano factor (0.08 Ge / 0.11 Si) are lower for Ge than they are for Si. Since typically this statistical energy resolution term (see section 2.5.3.2) is dominant at photon energies higher than $10\,\mathrm{keV}$, their performance is about $25\,\%$ better than Si(Li) detectors. Once the photon energy is above the Ge K-edge of $11.1\,\mathrm{keV}$, the obtained spectrum will be disturbed by the presence of escape peaks which are much more intense than is the case for Si based detectors. The higher intensity of the escape peaks is due to the smaller penetration depth in the Ge crystal, higher fluorescence yield and higher probability of the more energetic Ge photons to escape the crystal.

Due to the 10 times higher amount of primary elementary charges compared to gas detectors, the statistical fluctuations were reduced by a factor of three and because of the higher charge created, made it possible to use low-noise electronics. The main downside of Si(Li) and Ge(Li) based detectors is their need for liquid nitrogen (LN2) cooling, which makes them bulky and thus difficult to handle. The reason for the LN2 cooling is the high leakage current at room temperature combined with a rather high read-out capacitance, which is proportional to the area. The high capacitance results in a high contribution of the serial noise component that requires longer shaping times. However, for these longer shaping times, the shot-noise contribution from the leakage current increases.

2.5.2 Silicon Drift Detectors

Silicon Dirft Detectors(SDDs), introduced in 1983 by Gatti and Rehad, are characterised by the very low capacitance of the electrode collecting the signal charge which is independent of the active area of the device[52]. The separation of the active area and the collecting electrode diminishes the contribution of electronic noise due to the use of short shaping times. The working principle of an SDD can be understood starting from the sidewards depletion concept shown in Figure 2.21. With respect to a conventional pn-diode detector, shown in Figure 2.21a, where the n+ contact extends over

the full area on one side of the wafer, depletion of the bulk can also be achieved by positively biasing a small n+ electrode in comparison to p+ electrodes which cover both side, shown in Figure 2.21. Full depletion of the bulk in between the p+ electrodes, Figure 2.21c, can be obtained by applying a high enough n+ voltage. This design allows the depletion of the bulk with a four times lower voltage than which is needed for the conventional diode design. In an SDD, an additional electric field, parallel to the

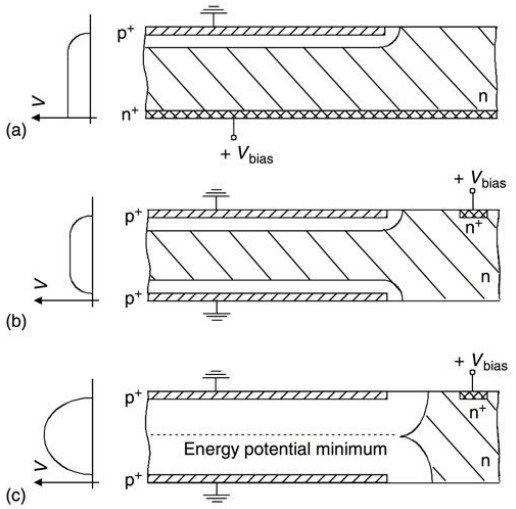

Figure 2.21: Explaining the sideward depletion concept. Figure from [52].

surface of the wafer, is applied in order to force the electrons in the energy potential minimum to drift towards the n+ anode. This collecting anode has a very low value of capacitance in comparison to a conventional pn-diode and is moreover independent of the active area of the device. This has the consequence that electronic noise is minimised and the value of the shaping time can be reduced. To be able to fully exploit these benefits arising from the low capacitance, the connection between detector and pre amplifier has to be kept short. This is achieved by means of the integration of the front-end transistor (FET) of the amplifying electronics directly on the detector wafer, see Figure 2.22[53, 54]. Moreover, the detector-preamplifier sensitivity to microphonic noise (mechanical vibrations) and electrical pickup is highly reduced. In addition to the FET, all devices required for the discharge of the signal charge and leakage current have to be integrated on the detector chip to fully exploit the benefits gained by implementing the FET on chip[55]. A new layout of the SDD allows the optimisation of the peak-to-background ratio by placing the anode and the integrated JFET at

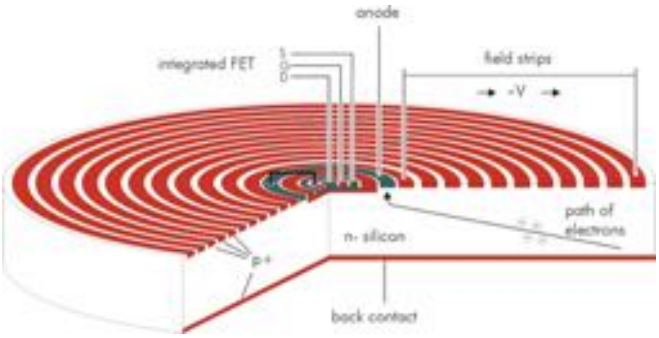

Figure 2.22: Design of an SDD, showing the n- Si bulk, p+ electrodes and the n- anode and integrated FET. Figure from [56].

the margin of the active area where they can be shielded from direct irradiation by the use of a collimator, eliminating the contribution of the charges created directly underneath the FET by the transistor electrodes instead of the anode (Figure 2.23)[57]. The gain in peak-to-background ratio can go as high as a factor of 6000. Besides this gain, the new layout allows for a smaller anode area, further decreasing the capacitance of the anode and thus improving the obtained energy resolution.

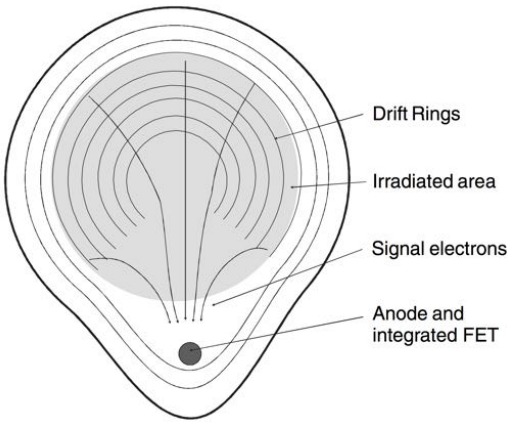

Figure 2.23: Layout of the SDD Droplet (SD^3) detector. The paths of the signal electrons towards the anode placed at the border of the detector are shown while only the gray overlay area is irradiated. Figure from [57].

2.5.3 Detector Characteristics

2.5.3.1 Detection efficiency

The detection efficiency is defined as the fraction of the total number of photons emitted by the source which actually interact with the detector volume and is completely absorbed by it. The efficiency is determined by several factors defined by geometrical and material parameters. The geometrical efficiency expresses the efficiency defined by the limited active area of the detector at a given distance of the source. In the case of a point source it can be calculated as follows:

$$\eta_G = \frac{\Omega}{4\pi} \tag{2.39}$$

where Ω is the detector solid angle under which the detector, a thin cylindrical detector, is seen from the source. The intrinsic efficiency is determined by the absorption coefficient of the detector material for a given photon energy and the thickness of the active material, limiting the number of photons which can be actually absorbed. It can thus be easily expressed by the following formula:

$$\eta_i = 1 - \exp\left(-\mu\rho x\right) \tag{2.40}$$

where μ is the mass attenuation coefficient at the given photon energy, ρ the detector active material density, and x the active layer thickness.

The photopeak efficiency is the fraction of the photons that deposit their entire energy in the detector material after the interaction with the detector material. Since the photoelectric effect is dominant with respect to the Compton effect for photons up to $100\,\mathrm{keV}$, and thus the reabsorption probability of the Compton scattered photon in the detector itself is high, the Compton continuum can extend from[50]:

$$\left[0, \frac{2E\alpha}{1+2\alpha}\right] \tag{2.41}$$

with $\alpha = \frac{E}{m_0c^2}$, where E is the primary X-ray energy, and m_0c^2 the electron rest mass. A second effect that limits the photopeak efficiency (η_{photo}) arises from the escape process. When an electron fills the vacancy left in an atom as a consequence of the interaction with a photon, another X-ray photon can be emitted with an energy equal to the difference in energy between the two electron states. There is a high probability that this photon will be reabsorbed by the detector material, leading to the detection of the

entire energy exchanged by the initial interaction[50]. However, if the initial interaction takes place close to the surface of the detector material, the likelihood that this secondary photon can escape the detector active material without being absorbed increases. This process gives rise to the presence of an escape peak in the obtained spectrum at an energy equal to the difference of the primary photon energy and the energy of the escaped photon. In the case of Si and Ge based detectors, the energy difference between the detected primary peak and the main escape peak is 1.74 and $9.89\,\mathrm{keV}$ respectively.

A fourth factor that influences the efficiency is the used detector window (η_w), often made of Be, and the thickness of the detector dead layer (η_{dl}) and can be described as:

$$\eta_w = \exp\left(-\mu_w \rho_w x_w\right) \tag{2.42}$$

$$\eta_{dl} = \exp\left(-\mu_{dl} \rho_{dl} x_{dl}\right) \tag{2.43}$$

The product of the intrinsic efficiency and the efficiency caused by the detector window and dead layer is called the quantum efficiency (QE) of the detector:

$$QE = \eta_i \cdot \eta_w \cdot \eta_{dl} \cdot \eta_{photo} \tag{2.44}$$

While the absorption of higher energy photons by the detector window and the detector dead layer is negligible, the effect on low energy photons ($E < 2\,\mathrm{keV}$) is not. Therefore, detector manufacturers also produce detectors equipped with thin polymer windows, which absorb less of the low energy photons. The downside of these detectors is their need to be operated in the dark since they are also sensitive to photons in the energy range of visible light. There are even windowless detection modules available which are only limited by the unavoidable detector dead layer but have the additional disadvantage that they need to be operated in the dark as well as in a vacuum environment.

2.5.3.2 Energy Resolution

For many spectroscopic applications, the accuracy of the energy of the detected photon is important. The energy resolution (ΔE) of a spectroscopy system (detector coupled with readout electronics) represents the capability of the system to distinguish photons with different energies. The pulse height distribution in a typical measurement of photons with energy E_0 is deviating from the ideal Dirac δ function due to several sources of statistical fluctuations affecting the accuracy. Typically, the energy resolution is expressed as the Full Width At Half Maximum (FWHM) of the measured

distribution. Alternatively, it can be expressed as percentage R, defined as the ratio between the FWHM and the centroid value of the distribution[2]:

$$R = \frac{\Delta E_{FWHM}}{E_0} \tag{2.45}$$

The obtained distribution can often be described by means of a Gaussian function:

$$G(E) = \frac{N_0}{\sigma\sqrt{2\pi}} \exp\left(-\frac{(E-E_0)^2}{2\sigma^2}\right) \tag{2.46}$$

where N_0 is the peak area, σ the standard deviation, and E_0 the peak centroid. The FWHM can be calculated as follows:

$$\Delta E_{FWHM} = 2\sqrt{2\ln 2}\sigma \tag{2.47}$$

As previously mentioned, the energy resolution is not only determined by the detector but also by the pulse processing electronics. Therefore, the ΔE_{meas} can be expressed as:

$$\Delta E^2_{meas} = \Delta E^2_{statistical} + \Delta E^2_{elec.noise} + \Delta E^2_{muliplication} + \Delta E^2_{collection} \tag{2.48}$$

The statistical resolution ($\Delta E_{statistical}$) is related to the statistical fluctuations in the conversion process of the photon energy into charge carriers and is thus inherent to the system, given detector material. Since Poisson statistics applies, one would expect the standard deviation to be equal to $\sigma = \sqrt{\bar{n}}$ but because of the correlation in the processes of generation of the individual carriers in semiconductor detectors, the distribution deviates from a pure Poisson statistics. To take this deviation into account, the so called Fano factor (F) was introduced[58].

$$\sigma = \sqrt{F\bar{n}} \tag{2.49}$$

The Fano factor can be experimentally defined for several frequently used detector materials, e.g. 0.11 for Si and 0.08 for Ge.

The $\Delta E_{elec.noise}$ term is the contribution of the detector amplifier system, which is expressed as equivalent noise charge (ENC), defined as the charge delivered by the detector which produces at the end of the electronic chain a pulse amplitude equal to the noise RMS value.

$$\Delta E_{elec.noise} = 2\sqrt{2\ln 2}\epsilon\frac{ENC}{q} \tag{2.50}$$

with q the electron charge. $\Delta E_{muliplication}$ is only applicable for detectors with internal multiplication. $\Delta E_{collection}$ is related to the partial collection of the signal charge created in the detector active material.

2.5.3.3 Peaking Time

To understand the concept of peaking time, also referred to as shaping time, one needs to take a closer look at one of the components of the pulse processing equipment of a detector, the pulse shaper. The pulse shaper transforms the narrow detector current pulse to a broader pulse, to reduce electronic noise, with a gradually rounded maximum at the peaking time to facilitate the measurement of the amplitude, see Figure 2.24. Therefore, to be able to handle pulses in rapid succession, cfr. a high photon flux on the detector, the duration of the shaped pulse must be limited to avoid overlapping of the signals which give rise to the appearance of sum peaks in the obtained spectrum. However, shortening the peaking time too much will give rise to an increased electronic noise signal, degrading the obtained energy resolution. One can thus calculate the optimal shaping time, is fully dependant on the ENC, for a certain system. The obtained ENC of a pulse processing system is defined as follows:

$$ENC^2 = (C_D + C_G)^2 \, a\frac{1}{\tau}A_1 + (C_D + C_G)^2 \, cA_2 + b\tau A_3 \qquad (2.51)$$

with C_D and C_G the detector and gate capacitance respectively, a,b, and c the noise power spectra (a detailed explanation lays outside of the scope of this manuscript), A_1, A_2, and A_3 are constants, and τ the peaking time. The three contributions shown in equation 2.51 are usually referred to as the series noise contribution, 1/f series noise contribution, and the parallel noise contribution. One can also see that the series noise contribution is inversely proportional to the peaking time τ while the contribution of the parallel noise contribution is directly proportional to τ. Therefore, the optimal peaking time, τ_{opt} can be found when the serial and parallel noise contributions are equal. To allow the user to tune the detection system to their specific needs, manufacturers often allow the peaking time to be selected within the interval of $0.5\tau_{opt} < \tau < 2\tau_{opt}$.

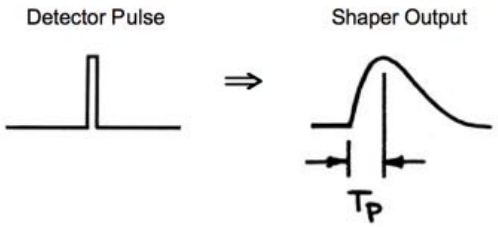

Figure 2.24: Showing the transformation caused by the pulse shaper on a narrow detector current pulse. Figure from [59].

2.5.4 High Resolution Imaging X-ray CCD Detectors

High Resolution Imaging X-ray CCD Detectors have been initially developed due to the scientific needs from astronomers and were first used on the X-ray Multi Mirror (XMM) satellite in December 1999[60]. Conceptually, the pn-CCD is based upon the silicon drift detector, incorporating an integrated n-channel JFET but delivering not only information on the energy of the photon but also on its location and time of detection[61]. Figure 2.25 shows a schematic cross-section of the pn-CCD wafer, showing the double-sided polished high resistivity n-type silicon wafer with both surfaces covered with p^+ implants. At the edge, an n^+ implant acts as readout anode while keeping an ohmic connection to the non depleted bulk of the silicon. A reverse bias is applied to both the p^+ junctions and the n^+ anode. The potential minimum for the electrons is now located in the middle of the wafer. However, an additional negative voltage on the p^+ back diode shift the potential minimum for the electrons from the centre towards the surface which contains the pixel structure. To form a CCD-type detector, the upper p^+ implant must be divided in p^+ strips which will serve as shift registers, shown in Figure 2.25. When applying adequate voltages to the three shift registers, local potential minima for the e^- are formed at a surface depth of about $10\,\mu\mathrm{m}$, at the intersection of the high resistivity bulk and the epi-layer. The epi-layer is an additional phosphorus doped opi-taxial layer that houses the p^+ shift registers which make up the pixel division in the transfer directions while channel stop implantations define the pixel boundaries orthogonally to the transfer direction. Three p^+ strips, with potentials ϕ_1, ϕ_2 and ϕ_3, comprise one pixel. Charges are initially collected under ϕ_3, the potential minimum for the electrons. A periodic modulation of the potentials shifts the potential minimum in a discrete way towards the n^+ readout node, Figure 2.26. Initially the charges are stored under ϕ_3 (Figure 2.26a), after the modulation of capacitance ϕ_2 so it has the same value as ϕ_2, the charges are shared over the potential minimum defined by ϕ_2 and ϕ_3 (Figure 2.26b). Raising potential ϕ_3 to the level of ϕ_1, results in a net shift of the charges from the potential minimum created by ϕ_3 to the minimum created by ϕ_2. Each shift register row is terminated by a readout amplifier, a JFET, which acts as a first signal amplifier and has already been described in section 2.5.2. The JFET output is wire bonded to the readout ASIC[1], called CMOS amplifier and multiplexer (CAMEX), performing further amplification, gain selection, signal filtering, sample and hold, and multiplexing onto an output line which is connected to an Anolgue Digital Converter (ADC)[63].

[1] application-specific integrated circuit

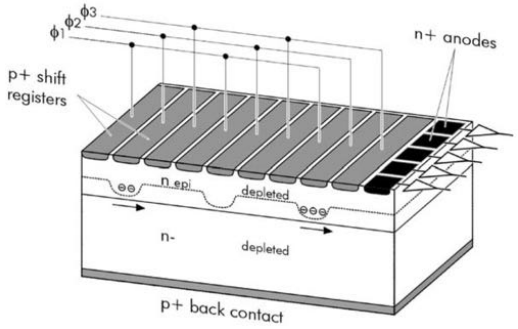

Figure 2.25: A schematic cross-section through the pn-CCD along a transfer channel. Adapted from [62].

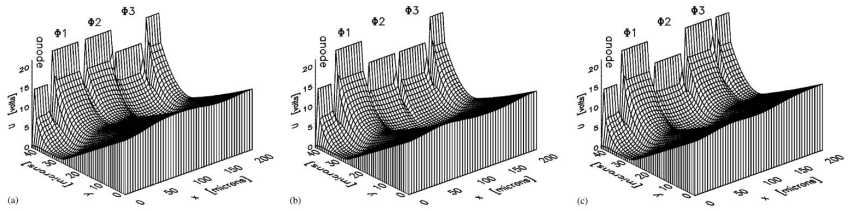

(a) *(b)* *(c)*

Figure 2.26: Showing the storing and shift register principle: (a) Charges are stored under ϕ_3, (b) sharing a larger volume when the potential of ϕ_2 gets modulated to the same value as ϕ_3, (c) when the potential of ϕ_3 gets raised to an equal value as ϕ_1, the charges are stored under ϕ_2. (Depleted bulk is only shown partially). (Adapted from [62])

Advantages of a pn-CCD

- Backside illumination causes the detector to be less sensitive to radiation damage while having a high quantum efficiency. The radiation hardness is further improved by the absence of MOS structures for per pixel on-chip control of charge transfer and amplification[60].

- The design allows for a full depletion of the detector bulk maximising the active thickness of the chip, thus maximising the quantum efficiency of the detector.

- pn-CCD chips can be designed with their application in mind, offering different sensitive thickness, pixel sizes and entrance windows.

- High transfer efficiency due to the enriched layer of the shift registers which allows the transfer of the electrons at a depth of about $10\,\mu\mathrm{m}$.

Limitations of a pn-CCD

- In charge coupled devices, where the signal electrons are transferred over many pixels, the charge shifting mechanism from pixel to pixel must be excellent. Leaving charges behind during the transfer means a reduction in signal amplitude. This loss can be corrected for but adds noise to the signal amplitude measurement. In a simple model, the lost charges can be parametrised according to Equation 2.52.

$$ENC^2_{trans} \approx \frac{E}{w}\,(1 - CTE)\,N_{trans} \tag{2.52}$$

  where E is the photon energy, w the energy to generate an electron-hole pair ($w = 3.7\,\mathrm{eV}$), CTE the charge transfer efficiency, and N_{trans} denotes the number of pixels transfers in the pn-CCD chip. The CTE is in the order of 10^{-5} but depends on the type of chip, temperature, accumulated dose, etc.

- The signal charges of one single X-ray photon will not always be collected in a single pixel, so the electronic content of several pixels must be summed. This increases for the so-called split event the electronic noise with $\sqrt{N}$, with N the number of pixels that accumulated the signal charge.

Applications Besides their application for satellite telescopes[60], pn-CCDs have been used for a variety of applications such as a scanning transmission X-ray microscopy (STXM)[64], plasma diagnostics[65], quantum optics[66], X-tray transmission radiography and tomography[67], and many other.

2.6 Quantitative X-ray Fluorescence

XRF does not only provides qualitative but also quantitative information on your sample. The ability to quantify matter using XRF is a two step process, first the net line intensities need to be derived from a spectrum, and second the net line intensities need to be converted into concentrations. Algorithms to achieve both steps involve the representation of several physical processes taking place in the sample material, as well as in the detector.

2.6.1 Spectrum Deconvolution

Deviation between experimental and theoretical XRF spectra is caused by two types of noise, amplitude and energy noise[2]. The former is caused by the statistical nature of the counting process, described by Poisson statistics:

$$P(N, N_0) = \frac{N_0^N}{N!} \mathrm{e}^{(-N_0)} \tag{2.53}$$

Showing the probability between the true amount of photons events (N_0) and the detected amount (N). The expected width of characteristic elemental lines in an XRF spectrum is 5 to $10\,\mathrm{eV}$, experimentally obtained spectra however show a typical line width ranging from 120 to $> 300\,\mathrm{eV}$ due to the nature of the conversion from photon to signal electrons and their conversion into a digital signal via amplifiers and pulse processing units, causing the addition of noise to the original signal. The effect of amplitude noise can be diminished by performing longer measurements or using X-ray beams with a higher flux density. Energy noise on the other hand can be altered by changing detector settings like peaking time, avoiding electrical interference, but is mainly an intrinsic characteristic of a detector and system electronics combination.

Characteristic lines exhibit a Lorentzian distribution which is then convoluted with the Gaussian profile of the detector response function, resulting in a Voigt profile. Since the Gaussian profile is dominant for lower energies ($\lessapprox 90\,\mathrm{keV}$), many deconvolution algorithms approximate the Voigt profile using a Gaussian function. An asymmetric profile, lower energy tailing, can arise due to incomplete charge collection in the detector due to the inactive layer found in every X-ray detector. In some cases the incomplete charge collection can even cause plateau formation at the low energy side of the peak, contribution to the background signal.

The background signal is on the other hand determined by the coherent and incoherent scattering of the primary X-rays in the sample. The incoherent scattering contribution is in general broader and non Gaussian shaped by the large range of scattering angles and Doppler effect[68].

The rise of escape peaks in a spectrum results from the escape of photons, characteristic for the detector material, after photoelectric absorption of the impinging photon near one of the edges of the detector crystal, therefore decreasing the detected energy of the absorbed photon by the energy of the escaping photon. The escape fraction f can be calculated using the following formula (for Si-K)[69]:

$$f = \frac{N_e}{N_p + N_e} = \frac{1}{2}\omega_K \left(1 - \frac{1}{J_K}\right)\left[1 - \frac{\mu_K}{\mu_I}\ln\left(1 + \frac{\mu_K}{\mu_I}\right)\right] \tag{2.54}$$

with N_e and N_p the number of photons representing the escape and originating fluorescence peak respectively, μ_I and μ_K the mass attenuation coefficients for the incoming and escaping photon, ω_K the K-shell fluorescence yield, and J_K the K shell jump ratio. A more complicated method was proposed by Schoonjans et al. [6], making use of Monte Carlo simulations to calculate the escape peak ratios since it simultaneously provides them for the Compton peak. These escape peaks become more important at higher energies, manifesting as two peaks corresponding to the forward and backscattered Compton photons.

Pulse pileup arises when two or more photons are detected during the shaping time of the detector, counting them as one photon with an energy equal to the sum. The probability on sum peak are thus influenced by the shaping time and photon flux on the detector.

All the described effects give rise to the need to deconvolute the spectrum to obtain the net line intensities by addressing peak overlap and background contributions.

AXIL[70] estimates the background contribution simultaneously with all other spectral features, who fits the net peak intensities by least-squares fitting of an algebraic function. The object function (χ^2) is defined as the weighted sum of squares of the difference between model ($y(i)$) and the experimental spectrum (y_i) over a Region Of Interest (ROI) of the spectrum:

$$\chi^2 = \sum_{i=1}^{n} \frac{1}{\sigma_i^2} \left[y_i - y\left(i, a_1, \ldots, a_m\right) \right]^2 \tag{2.55}$$

with σ_i^2 the variance of data point i, and a_j are the parameters of the model function. The goal of the algorithm is minimising χ^2, optimising the parameters of the model function. This is achieved by setting the partial derivative of χ^2 to the parameters to zero:

$$\frac{\partial \chi^2}{\partial a_j} = 0,\ j = 1, \ldots, m \tag{2.56}$$

The construction of the model function is of paramount importance, taking into account all the spectral aspects described earlier, not to end up with systematic errors in the estimation of the net peak intensities. In general the fitting function is kept simple, with as few parameters as possible, which in general looks like:

$$y(i) = y_B(i) + \sum_P y_P(i) \tag{2.57}$$

with $y(i)$ the calculated counts for channel i, $y_B(i)$ the description of the spectral background, and $y_P(i)$ the peak intensity contribution. The back-

ground contribution is difficult to describe due to the large number of processes that contribute to it, often leading to the use of polynomial expressions, as there are linear polynomials and exponential polynomials[2, 70]:

$$y_B(i) = a_0 + a_1(E_i - E_0) + a_2(E_i - E_0)^2 + \ldots + a_n(E_i - E_0)^n \tag{2.58}$$

$$y_B(i) = a_0 + \exp\left(a_1(E_i - E_0) + a_2(E_i - E_0)^2 + \ldots + a_n(E_i - E_0)^n\right) \tag{2.59}$$

with n the degree of the polynomial and a_k the fitting parameters.

As mentioned previously, in general spectral peaks can be described as a Gaussian function:

$$\frac{A}{\sigma\sqrt{2\pi}} \exp\left[-\frac{(x_i - \mu)^2}{2\sigma^2}\right] \tag{2.60}$$

with A the peak area, σ the width of the Gaussian and μ the peak centroid, resulting in an optimisation of 3 parameters per spectral feature. The minimisation of χ^2 thus requires an iterative approach due to the exponential function in Equation 2.60. One can see that the amount of parameters in the model function is substantial, for a spectrum of 10 elements, one has 20 peaks in the ideal case, resulting in a total amount of 60 parameters. However, the physical nature of the fluorescence lines can be used to optimise the model function since the energies of these lines is well known. Equation 2.60 can thus be written as a function of energy instead of channel number by defining E_0 the energy of channel 0 and expressing a gain (ΔE) in $^{\text{eV}}/_{\text{channel}}$:

$$E(i) = E_0 + \Delta E \times i \tag{2.61}$$

substitution in Equation 2.60 gives:

$$G(i, E_j) = \frac{\Delta E}{s\sqrt{2\pi}} \exp\left[-\frac{(E_j - E(i))^2}{2s^2}\right] \tag{2.62}$$

with E_j the energy of the characteristic line and s the peak with given by:

$$s^2 = \sigma_{noise}^2 + \epsilon F E_j \tag{2.63}$$

with F the fano factor, and ϵ the mean energy required to produce a single electron-hole pair (3.62 eV for Si). By introducing these four new parameters, E_0, ΔE, σ_{noise}, and F, which will be optimised during the fitting process, a reduction of the dimensionality of the problem is achieved. Our fitting of 10 elements with initially 60 parameters is thus reduced to 24 by

the extra information given by the user (E_0, ΔE, and the present peaks). A further optimisation of the fitting function can be obtained when considering the linkage between a number of lines, like KL_2 and KL_3 doublets, or even all K-lines of an element. Therefore fitting the entire group with a single area parameter (A):

$$y_P(i) = A \sum_{j=1}^{N_P} R_J G(i, E_j) \tag{2.64}$$

where G represents the Gaussian for the various lines with energy E_j, with relative intensities R_j. Although $\sum R_j = 1$, and the transition probabilities of all lines are constant, the actual relative intensities may be influenced by absorption or enhancement effects. The tabulated value is therefore only used as an initial estimate in the iteration procedure, enhancing the resolving power of the algorithm when dealing with peak overlap. Further enhancements of the algorithm include dealing with escape peaks, pule pile-up and modified peak shapes. Solving the non-linear least-squares problem can be done in several mathematical algorithms like the gradient method, first-order expansion, or the Marquardt algorithm.

An alternative approach to solving the non-linear least-squares fitting operation was proposed by Ryan et al. [71], whom called it Dynamic Analysis (DA)[72]. The approach is based on the fact that in the multidimensional χ^2 parameter space, the partial derivatives of all parameters a_k at the location of the minimum equals zero, $\frac{\partial \chi^2}{\partial a_k} = 0$, leading to:

$$\sum_k \sum_i w_i \left(\frac{\partial f_i}{\partial a_j} \right) \left(\frac{\partial f_i}{\partial a_k} \right) a_k = \sum_i w_i \left(\frac{\partial f_i}{\partial a_j} \right) S_i \tag{2.65}$$

with j the X-ray line of element k. This set of simultaneous linear equations can be expressed in a matrix equation:

$$\alpha a = \beta S \tag{2.66}$$

where α and β are matrices in terms of the partial derivatives, and S the spectrum vector:

$$\alpha_{ij} = \sum_i W_i^{-1} \beta_{ji} \beta_{ki} \tag{2.67}$$

$$\beta_{ji} = w_i \left(\frac{\partial f_i}{\partial a_j} \right) \tag{2.68}$$

The vector A, which contains all linear intensity factors a_k, can thus be calculated:

$$A = \Gamma S \tag{2.69}$$

$$\text{with} \quad \Gamma_{ki} = \sum_j \alpha_{kj}^{-1} \beta_{ij} \tag{2.70}$$

with Γ the DA matrix.

Since a matrix multiplication is more computationally efficient, this fitting algorithm is much faster than non-linear least-square fitting but offers less flexibility since the DA matrix is determined on a single spectrum.

2.6.2 Quantification Procedures

Previous section showed how net line intensities can be extracted from an XRF spectrum. This section will explain how these intensities can be converted into concentrations. While the easiest way of quantification is done based on the measurement of a Standard Reference Material (SRM) with a similar matrix to the sample, it is the most prone to errors. Two other, more complex methods will be explained as well, fundamental parameter and reverse Monte Carlo simulations based quantification algorithms.

2.6.2.1 Basic quantification

The basic quantification scheme allows quantification using the measurement of a SRM. Since no absorption effects are taken into account and in principle just does a scaling of the illuminated mass, the matrices of sample and SRM should be matched as closely as possible. One can estimate the concentration of the unknown using the following formula:

$$c_{U_i} = \frac{I_{U_i}}{S_{C_U}} \cdot \frac{S_{C_{SRM}}}{I_{SRM_i}} \cdot c_{SRM_i} \tag{2.71}$$

with c_{U_i} the concentration of element i of the unknown, I_{U_i} and I_{SRM_i} the net line intensity of element i of the unknown and SRM respectively, S_{C_U} and $S_{C_{SRM}}$ the Compton scatter intensity for the unknown and SRM, and c_{SRM_i} the concentration of element i in the SRM.

2.6.2.2 Fundamental Parameter Method

Sherman proposed this method in the 1950s and exploits the theoretical relationship between the net line intensities and the elemental concentrations[73].

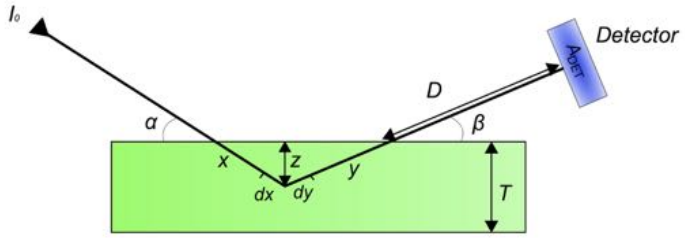

Figure 2.27: Illustrating the simplest case of fundamental parameter method where a homogeneous sample is illuminated by a monochromatic beam with intensity I_0 at an angle α. The fluorescent X-rays produces in the sample, with thickness T, is detected by a detector with an active area of A_{DET} at a distance D and angle β

The simplest form describes a homogeneous sample that is being illuminated by a monochromatic X-ray beam, shown in figure 2.27. The sample is defined as an infinitely wide layer with thickness T, density ρ, and consists out of n elements with a weight fraction w_i $\sum_{i=1}^{\infty} w_i = 1$ and is irradiated by a monochromatic beam with a flux I_0, energy E_0, and incidence angle α. The fluorescent X-rays are detected at an angle β by a detector with an active area A_{DET} at distance D. The formula derivations are based on the following definition of the coordinate system: X-ray beam (x-axis), detector axis (y-axis), and the sample normal (z-axis).

$$x = \frac{z}{\sin\alpha} \tag{2.72}$$

$$y = \frac{z}{\sin\beta} \tag{2.73}$$

$$\mathrm{d}x = \frac{\mathrm{d}z}{\sin\alpha} \tag{2.74}$$

$$\mathrm{d}y = \frac{\mathrm{d}z}{\sin\beta} \tag{2.75}$$

$$\tag{2.76}$$

The derivation processes from Fundamentel Parameter Method (FPM) consists out of three steps. Firstly, the net intensity of the fluorescent intensity of element i that is generated within the interval $[x, x + \mathrm{d}x]$ using the Lambert-Beer formula (example given for Kα line):

$$\mathrm{d}I^*_{i,K\alpha} = I_0 \exp\left(-\mu_0\rho x\right) \mu_0\rho\mathrm{d}x \frac{w_i\tau_{i,K}}{\mu_0} p_{K\alpha}\omega_K \tag{2.77}$$

$$= I_0 \exp\left(-\mu_0\rho x\right) w_i Q_{i,K\alpha}\rho\mathrm{d}x \tag{2.78}$$

with:

- w_i = the weight fraction of element i;
- $\mu_0 = \mu(E_0) = \sum_{j=1}^{n} w_j \mu_{j,E_0}$ = the attenuation coefficient of the sample of the primary X-ray beam (E_0);
- $\tau_{i,K}$ = K-shell partial photoionisation cross section of element i;
- $p_{K\alpha}$ = transition probability;
- ω_K = fluorescence yield;
- $Q_{i,K\alpha} = \tau_{i,K} p_{K\alpha} \omega_K$ = XRF production cross section.

Secondly, one needs to determine the detected $K\alpha$ intensity of element i that was generated in the depth interval $[z, z + \mathrm{d}z]$:

$$\mathrm{d}I_{i,K\alpha} = \mathrm{d}I^*_{i,K\alpha} \frac{\Omega_{DET}}{4\pi} \exp\left(-\mu_1 \rho y\right) \tag{2.79}$$

$$= I_0 \frac{\Omega_{DET}}{4\pi} \exp\left(-\mu_0 \rho y\right) \exp\left(-\mu_1 \rho y\right) w_i Q_{i,K\alpha} \rho \mathrm{d}x \tag{2.80}$$

$$= I_0 \frac{\Omega_{DET}}{4\pi} \exp\left[-\left(\frac{\mu_0}{\sin\alpha} + \frac{\mu_1}{\sin\beta}\right) \rho z\right] w_i Q_{i,K\alpha} \rho \mathrm{d}x \tag{2.81}$$

$$= I_0 \frac{\Omega_{DET}}{4\pi \sin\alpha} w_i Q_{i,K\alpha} \exp\left(-\chi \rho z\right) \rho \mathrm{d}z \tag{2.82}$$

$$= I_0 G w_i Q_{i,K\alpha} \exp\left(-\chi \rho z\right) \rho \mathrm{d}z \tag{2.83}$$

with:

- Ω_{DET} = detector solid angle;
- $\mu_1 = \mu(E_{i,K\alpha}) = \sum_{j=1}^{n} w_j \mu_{j,i,K\alpha}$ = the attenuation coefficient of the material at energy $E_{i,K\alpha}$;
- $G = \frac{\Omega_{DET}}{4\pi \sin\alpha} \approx \frac{A_{DET}}{4\pi D^2 \sin\alpha}$ = geometry factor.

The last step includes integrating over the total sample thickness yielding the total detected intensity:

$$I_{i,K\alpha} = \int_0^T \mathrm{d}I_{i,K\alpha} \tag{2.84}$$

$$= I_0 G w_i Q_{i,K\alpha} \rho \int_0^T \exp\left(-\chi \rho z\right) \rho \mathrm{d}z \tag{2.85}$$

$$= I_0 G w_i Q_{i,K\alpha} \rho T \left(\frac{1 - \exp\left(-\chi \rho T\right)}{\chi \rho T}\right) \tag{2.86}$$

$$= I_0 G w_i Q_{i,K\alpha} \rho T A_{corr} \tag{2.87}$$

Where A_{corr} is the so-called *absorption correction factor*, representing the absorption caused by the sample matrix, ranging from 0 to 1. Since A_{corr} depends on w_i, the system of equations (n = number of elements) needs to be solved iteratively, except for when dealing with infinitesimally thin samples. In this special case one can assume A_{corr} to be equal to 1. Although much more advanced versions of the FPM exist, the presented form has the following limitations:

- The primary X-ray beam is assumed to be monochromatic;
- The sample is assumed to be flat and homogeneous;
- Only first order interactions are taken into account, ignoring secondary effects such as enhancement effects. Although extensions exist, taking higher order interactions into account, they increase the complexity tremendously;
- The XRF production cross-sections Q are often not well known, especially for L and M-lines;
- The detector is assumed to be ideal, having a quantum efficiency of $100\,\%$ independently on the energy.

Some of these issues can be avoided by making use of a SRM based approach to cancel out some of the unknown factors. When using Equation 2.87 for both unknown and SRM one gets following equation:

$$\frac{I^u_{i,K\alpha}}{I^{SRM}_{i,K\alpha}} = \frac{I^u_0 G w^u_i Q_{i,K\alpha} \rho^u T A^u_{corr}}{I^{SRM}_0 G w^{SRM}_i Q_{i,K\alpha} \rho^{SRM} T A^{SRM}_{corr}} \tag{2.88}$$

Thus when measuring the unknown and the SRM using the same setup, the geometry factor G can be eliminated as well as the XRF production cross section $Q_{i,K\alpha}$, simplifying Equation 2.88 to:

$$\frac{I^u_{i,K\alpha}}{I^{SRM}_{i,K\alpha}} = \frac{I^u_0 w^u_i \rho^u T A^u_{corr}}{I^{SRM}_0 w^{SRM}_i \rho^{SRM} T A^{SRM}_{corr}} \tag{2.89}$$

2.6.3 Monte Carlo Simulations for Quantitative X-ray Fluorescence

Monte Carlo simulations are generally used to solve problems that are too complex to solve analytically. Solving these mathematical problems is based on statistical sampling performed using random numbers on a probability density function that describes the problem. It was first published in

1949 and was initially used to perform calculations to investigate radiation protection against ionising radiation during the Manhattan project[74]. Due to the power of Monte Carlo simulations, it widely spread over different scientific disciplines. Since describing Monte Carlo simulations used for XRF simulation falls out of the scope of this dissertation, only the 2 major components will be explained. For a more detailed description the author would like to refer to the work of Vincze, L. and Schoonjans, T[6, 21, 23, 25, 75, 76].

2.6.3.1 Pseudo Random Numbers

During the early stages, tabulated random numbers were used for Monte Carlo simulations. With the rise of computers, these were replaced my the generation of Pseudo Random Number Generators(PRNGs), which are produced by mathematical algorithms, thus having a finite period. Most PRNGs are based on a linear congruential random number generation[77]:

$$X_{n+1} = (aX_n + c) \mod 2^{32} \tag{2.90}$$

with X being a pseudo random number, a and c are integers. It is clear that a starting value X_0, called a seed, is needed, producing an array with a cycle length of 2^{32}. Since the random character of the produced pseudo random numbers depends on this starting value, it has to be chosen with great care.

2.6.3.2 Distribution Functions

Considering an experiment having N possible values of a discrete random variable x are observed, where f_i expresses the frequency of each possible value x_i. The probability p_i of observing a discrete value X equal to x_i is expressed as:

$$p_i = p\left(X = x_i\right) = f_i \tag{2.91}$$

with $\sum_{i=1}^{N} f_i = 1$. The cumulative distribution function describes the probability that X equals a value lower than or equal to x_j:

$$P\left(X \leq x_j\right) = \sum_{i=1}^{j} p_i \tag{2.92}$$

$$\text{with} j \leq N \tag{2.93}$$

where $P\left(x \leq x_1\right) = 0$ and $P\left(x \leq x_N\right) = 1$. Continuous random variables r, uniformly distributed over $[0, 1]$, can be related to P since it also takes

on values in $[0, 1]$. This allows the retrieval of a discrete value x_j which corresponds to r:

$$x_j = P^{-1}(r) \tag{2.94}$$

This method is referred to as random sample from the inverse cumulative probability distribution, constituting the basis of the Monte Carlo method. In general, for a random value x which is continuous and distributed in the interval $[x_{min}, x_{max}]$ with the probability function $p(x)$, the cumulative probability distribution function $P(x)$ is given by:

$$P(x) = \frac{\int_{x_{min}}^{x} p(z)\mathrm{d}z}{\int_{x_{min}}^{x_{max}} p(z)\mathrm{d}z} \tag{2.95}$$

Values for x are thus obtained by reverse sampling by means of a random number r according to $P(x)$:

$$x = P^{-1}(x) \tag{2.96}$$

References

[1] W.C. Röntgen. Über eine neue Art von Strahlen. *Annalen der Physik und Chemie*, 64:1–37, 1898.

[2] R. Van Grieken and A. Markowicz. *Handbook of X-Ray Spectrometry, Second Edition*. CRC PRESS, 2001.

[3] J.P. Grotzinger, J. Crisp, A. R. Vasavada, R.C. Anderson, C.J. Baker, R. Barry, D.F. Blake, P. Conrad, K.S. Edgett, B. Ferdowski, R. Gellert, J.B. Gilbert, M. Golombek, J. Gomez-Elvira, D.M. Hassler, L. Jandura, M. Litvak, P. Mahaffy, J. Maki, M. Meyer, M.C. Malin, I. Mitrofanov, J.J. Simmonds, D. Vaniman, R.V. Welch, and R.C. Wiens. Mars Science Laboratory Mission and Science Investigation. *SPACE SCIENCE REVIEWS*, 170(1-4):5–56, SEP 2012. ISSN 0038-6308.

[4] W.D. Coolidge. A powerful röntgen ray tube with a pure electron discharge. *Physical Review*, 2(6):409–430, 1913.

[5] 12 2014. URL `http://en.wikipedia.org/wiki/X-ray_tube`.

[6] T. Schoonjans, L. Vincze, V.A. Sole, M.S. del Rio, P. Brondeel, G. Silversmit, K. Appel, and C. Ferrero. A general Monte Carlo simulation of energy dispersive X-ray fluorescence spectrometers - Part 5 Polarized radiation, stratified samples, cascade effects, M-lines. *SPECTROCHIMICA ACTA PART B-ATOMIC SPECTROSCOPY*, 70:10–23, APR 2012. ISSN 0584-8547.

[7] C.-K. Park, J.-P. Kim, S.-J. Yun, S.-H. Lee, and J.-S. Park. Field emission properties of carbon nanotubes grown on a conical tungsten tip for the application of a microfocus x-ray tube. *THIN SOLID FILMS*, 516(2-4):304–309, DEC 3 2007. ISSN 0040-6090. 34th International Conference on Metallurgical Coatings and Thin Films, San Diego, CA, APR 23-27, 2007.

[8] H. S. Kim, D. Q. Duy, J. H. Kim, H. J. Lee, D. M. Yoon, S. S. Shin, J. W. Ha, K. J. Lee, Y. G. Hwang, C. H. Lee, and C.-Y. Park. Field-emission electron source using carbon nanotubes for X-ray tubes. *JOURNAL OF THE KOREAN PHYSICAL SOCIETY*, 52(4):1057–1060, APR 2008. ISSN 0374-4884.

[9] F. Sprenger, X. Calderon, E. Gidcumb, J. Lu, X. Qian, D. Spronk, A. Tucker, G. Yang, and O. Zhou. Stationary digital breast tomosynthesis with distributed field emission X-ray tube. In Pelc, NJ and

Samei, E and Nishikawa, RM, editor, *MEDICAL IMAGING 2011: PHYSICS OF MEDICAL IMAGING*, volume 7961 of *Proceedings of SPIE*, 1000 20TH ST, PO BOX 10, BELLINGHAM, WA 98227-0010 USA, 2011. Dynasil Corp/RMD Res; Amer Assoc Physicists Med; DQE Instruments, Inc; Ocean Thin Films, Inc; Univ Cent Florida, CREOL - Coll Opt & Photon; VIDA Diagnost, Inc; SPIE, SPIE-INT SOC OPTICAL ENGINEERING. ISBN 978-0-8194-8503-8. Conference on Medical Imaging 2011 - Physics of Medical Imaging, Lake Buena Vista, FL, FEB 13-17, 2011.

[10] O. Hemberg, M. Otendal, and H.M. Hertz. Liquid-metal-jet anode electron-impact x-ray source. *APPLIED PHYSICS LETTERS*, 83(7): 1483–1485, AUG 18 2003. ISSN 0003-6951.

[11] M. Otendal, T. Tuohimaa, U. Vogt, and H. M. Hertz. A 9 keV electron-impact liquid-gallium-jet x-ray source. *REVIEW OF SCIENTIFIC INSTRUMENTS*, 79(1), JAN 2008. ISSN 0034-6748.

[12] 12 2014. URL `http://www.nsrrc.org.tw`.

[13] H. Wiedemann. *Synchrotron Radiation*. SPRINGER, 2003.

[14] 12 2014. URL `www.desy.de`.

[15] W.J. Goodman. *Statistical Optics*. WILEY, 2000.

[16] M. Wulff, F. Schotte, G. Naylor, D. Bourgeois, K. Moffat, and G. Mourou. Time-resolved structures of macromolecules at the ESRF: Single-pulse Laue diffraction, stroboscopic data collection and femtosecond flash photolysis. *NUCLEAR INSTRUMENTS & METHODS IN PHYSICS RESEARCH SECTION A-ACCELERATORS SPECTROMETERS DETECTORS AND ASSOCIATED EQUIPMENT*, 398 (1):69–84, OCT 11 1997. ISSN 0168-9002. doi: {10.1016/S0168-9002(96)01226-0}. Symposium on Future Electron Accelerators and Free Electron Lasers - Prospects and Opportunities in Natural Sciences, UPPSALA, SWEDEN, APR 25-26, 1996.

[17] P. Wessels, M. Schlie, M. Wieland, J. Ewald, G. Abbati, S. Baumbach, J. Overbuschmann, T. Nisius, A. Vogel, A. Neumann, A. Meents, J. Viefhaus, H. P. Oepen, G. Meier, T. Wilhein, and M. Drescher. XMCD microscopy with synchronized soft X-ray and laser pulses at PETRA III for time-resolved studies. In Xu, H and Wu, Z and Tai, R, editor, *11TH INTERNATIONAL CONFERENCE ON X-RAY*

MICROSCOPY (XRM2012), volume 463 of *Journal of Physics Conference Series*, DIRAC HOUSE, TEMPLE BACK, BRISTOL BS1 6BE, ENGLAND, 2013. Natl Synchrotron Radiat Lab; Chinese Acad Sci; Natl Nat Sci Fdn China; BRUKER; xradia, IOP PUBLISHING LTD. doi: {10.1088/1742-6596/463/1/012023}. 11th International Conference on X-ray Microscopy (XRM), Shanghai Synchrotron Radiat Facil, Shanghai, PEOPLES R CHINA, AUG 05-10, 2012.

[18] P. Wessels, J. Ewald, M. Wieland, T. Nisius, G. Abbati, S. Baumbach, J. Overbuschmann, A. Vogel, A. Neumann, J. Viefhaus, H. P. Oepen, G. Meier, T. Wilhein, and M. Drescher. Time-resolved soft X-ray microscopy of magnetic nanostructures at the P04 beamline at PETRA III. In *22ND INTERNATIONAL CONGRESS ON X-RAY OPTICS AND MICROANALYSIS*, volume 499 of *Journal of Physics Conference Series*, DIRAC HOUSE, TEMPLE BACK, BRISTOL BS1 6BE, ENGLAND, 2014. DESY; TU Dresden; Helmholtz Zentrum Geesthacht, IOP PUBLISHING LTD. doi: {10.1088/1742-6596/499/1/012009}. 22nd International Congress on X-Ray Optics and Microanalysis (ICXOM), Univ Hamburg, Hamburg, GERMANY, SEP 02-06, 2013.

[19] K.J. Kim. Angular-Distribution of Undulator Power for an Arbitrary Deflection Parameter-K. *NUCLEAR INSTRUMENTS & METHODS IN PHYSICS RESEARCH SECTION A-ACCELERATORS SPECTROMETERS DETECTORS AND ASSOCIATED EQUIPMENT*, 246(1-3): 67–70, MAY 15 1986. ISSN 0168-9002.

[20] R. Tertian and F. Claisse. *Principles of Quantitative X-ray Fluorescence Analysis*. (Heyden), 1982.

[21] L. Vincze, K. Janssens, B. Vekemans, and F. Adams. Monte Carlo simulation of X-ray fluorescence spectra: Part 4. Photon scattering at high X-ray energies. *SPECTROCHIMICA ACTA PART B-ATOMIC SPECTROSCOPY*, 54(12):1711–1722, NOV 22 1999. ISSN 0584-8547.

[22] J. W. M. Dumond. The linear momenta of electrons in atoms and in solid bodies as revealed by x-ray scattering. *Rev. Mod. Phys.*, 5:1–33, Jan 1933.

[23] L. Vincze, K. Janssens, F. Adams, M.L. Rivers, and K.W. Jones. A General Monte-Carlo Simulation of ED-XRF Spectrometers .2. Polarized Monochromatic Radiation, Homogeneous Samples. *SPEC-*

TROCHIMICA ACTA PART B-ATOMIC SPECTROSCOPY, 50(2): 127–147, MAR 1995. ISSN 0584-8547.

[24] T. Schoonjans, A. Brunetti, B. Golosio, M.S. del Rio, V.A. Sole, C. Ferrero, and L. Vincze. The xraylib library for X-ray-matter interactions. Recent developments. *SPECTROCHIMICA ACTA PART B-ATOMIC SPECTROSCOPY*, 66(11-12):776–784, NOV-DEC 2011. ISSN 0584-8547.

[25] L. Vincze, K. Janssens, and F. Adams. A General Monte-Carlo Simulation of Energy-Dispersive X-ray-Fluorescence Spectrometers .1. Unpolarized Radiation, Homogeneous Samples. *SPECTROCHIMICA ACTA PART B-ATOMIC SPECTROSCOPY*, 48(4):553–573, MAR 1993. ISSN 0584-8547.

[26] P. Kirkpatrick and A.V. Baez. Formation of optical images by x-rays. *J. Opt. Soc. Am.*, 38(9):766–773, Sep 1948.

[27] O. Hignette, G. Rostaing, P. Cloetens, A. Rommeveaux, W. Ludwig, and A. Freund. Submicron focusing of hard X-rays with reflecting surfaces at the ESRF. In McNulty, I, editor, *X-RAY MICRO- AND NANO-FOCUSING: APPLICATIONS AND TECHNIQUES II*, volume 4499 of *PROCEEDINGS OF THE SOCIETY OF PHOTO-OPTICAL INSTRUMENTATION ENGINEERS (SPIE)*, pages 105–116, 1000 20TH ST, PO BOX 10, BELLINGHAM, WA 98227-0010 USA, 2001. SPIE, SPIE-INT SOC OPTICAL ENGINEERING. ISBN 0-8194-4213-5. Conference on X-Ray Micro- and Nano-Focusing - Applications and Techniques II, SAN DIEGO, CA, JUL 30, 2001.

[28] D.H. Bilderback, S.A. Hoffman, and D.J. Thiel. Nanometer Spatial-Resolution Achieved in Hard X-ray-Imaging and Laue Diffraction Experiments. *SCIENCE*, 263(5144):201–203, JAN 14 1994. ISSN 0036-8075.

[29] U. Lienert, C. Schulze, V. Honkimaki, T. Tschentscher, S. Garbe, O. Hignette, A. Horsewell, M. Lingham, H.F. Poulsen, N.B. Thomsen, and E. Ziegler. Focusing optics for high-energy X-ray diffraction. *JOURNAL OF SYNCHROTRON RADIATION*, 5(3):226–231, MAY 1 1998. ISSN 0909-0495. 6th International Conference on Synchrotron Radiation Instrumentation (SRI'97), HIMEJI, JAPAN, AUG 04-08, 1997.

[30] J.H. Underwood, T.W. Barbee, and C. Frieber. X-Ray Microscope

with Multilayer Mirrors. *APPLIED OPTICS*, 25(11):1730–1732, JUN 1 1986. ISSN 0003-6935.

[31] B. Lai, W.B. Yun, D. Legnini, Y. Xiao, J. Chrzas, P.J. Viccaro, V. White, S. Bajikar, D. Denton, F. Cerrina, E. Difabrizio, M. Gentili, L. Grella, and M. Baciocchi. Hard X-Ray Phase Zone Plate Fabricated by Lithographic Techniques. *APPLIED PHYSICS LETTERS*, 61 (16):1877–1879, OCT 19 1992. ISSN 0003-6951.

[32] E. Di Fabrizio, F. Romanato, M. Gentili, S. Cabrini, B. Kaulich, J. Susini, and R. Barrett. High-efficiency multilevel zone plates for keV X-rays. *NATURE*, 401(6756):895–898, OCT 28 1999. ISSN 0028-0836.

[33] H. Mimura, S. Matsuyama, H. Yumoto, H. Hara, K. Yamamura, Y. Sano, M. Shibahara, K. End, Y. Mori, Y. Nishino, K. Tamasaku, M. Yabashi, T. Ishikawa, and K. Yamauchi. Hard X-ray diffraction-limited nanofocusing with Kirkpatrick-Baez mirrors. *JAPANESE JOURNAL OF APPLIED PHYSICS PART 2-LETTERS & EXPRESS LETTERS*, 44(16-19):L539–L542, 2005. ISSN 0021-4922.

[34] O. Hignette, P. Cloetens, C. Morawe, C. Borel, W. Ludwig, P. Bernard, A. Rommeveaux, and S. Bohic. Nanofocusing at ESRF using graded multilayer mirrors. In Choi, JY and Rah, S, editor, *Synchrotron Radiation Instrumentation, Pts 1 and 2*, volume 879 of *AIP CONFERENCE PROCEEDINGS*, pages 792–795, 2 HUNTINGTON QUADRANGLE, STE 1NO1, MELVILLE, NY 11747-4501 USA, 2007. Pohang Accelerator Lab; Japan Synchrotron Radiat Res Inst; Korea Minist Sci & Technol; Korea Synchrotron Radiat Users Assoc; Japanese Soc Synchrotron Radiat Res; Daegu Metropolitan City; Daegu Convent & Visitors Bur; Korea Tourism Org; Korean Phys Soc, AMER INST PHYSICS. ISBN 978-0-7354-0373-4. 9th International Conference on Synchrotron Radiation Instrumentation (SRI 2006), Daegu, SOUTH KOREA, MAY 28-JUN 02, 2006.

[35] Y. Mori, K. Yamauchi, K. Yamamura, H. Mimura, Y. Sano, A. Saito, K. Ueno, K. Endo, A. Souvorov, M. Yabashi, K. Tamasaku, and T. Ishikawa. Sub-micron focusing of hard X-ray beam by elliptically figured mirrors for scanning X-ray microscopy. In Freund, AK and Macrander, AT and Ishikawa, T and Wood, JL, editor, *X-RAY MIRRORS, CRYSTALS, AND MULTILAYERS II*, volume 4782 of *PROCEEDINGS OF THE SOCIETY OF PHOTO-OPTICAL INSTRUMENTATION ENGINEERS (SPIE)*, pages 58–64, 1000 20TH

ST, PO BOX 10, BELLINGHAM, WA 98227-0010 USA, 2002. SPIE; Boeing Co; Pacific NW Natl Lab; Washington State Univ, Coll Sci; Washington State Univ, Coll Engn & Architecture; Washington Technol Ctr; Univ Washington, Coll Engn; Univ Washington, Ctr Nanotechnol, SPIE-INT SOC OPTICAL ENGINEERING. ISBN 0-8194-4549-5. Conference on X-Ray Mirrors, Crystals and Multilayers II, SEATTLE, WA, JUL 10-11, 2002.

[36] G.E. Ice, J.S. Chung, J.Z. Tischler, A. Lunt, and L. Assoufid. Elliptical x-ray microprobe mirrors by differential deposition. *REVIEW OF SCIENTIFIC INSTRUMENTS*, 71(7):2635–2639, JUL 2000. ISSN 0034-6748.

[37] 12 2014. URL `https://news.slac.stanford.edu/features/k-b-mirrors-harness-x-rays-science`.

[38] F. Jentzsch and E. Nähring. Die fortleitung von licht- und röntgenstrahlen durch röhren. *ZEITSCHRIFT FÜR TECHNISCHE PHYSIK*, 12(3):185–189, 1931.

[39] A. Erko, M. Idir, Th. Krist, and A.G. Michette. *Modern Developments in X-Ray and Neutron Optics*. SPRINGER, 2008.

[40] V. A. Arkadiev, A. I. Kolomitsev, M. A. Kumakhov, V. V. Labuzov, and I. Y. Ponomarev. Focusing system using multiple reflection of radiation from curved surfaces. *Soviet Technical Physics Letters*, 14 (1):42, 1988.

[41] M. A. Kumakhov. Radiation of Channeled Particles in Crystals. *Energoatomizdat*, 1986.

[42] K. Tsuji, J. Injuk, and R. Van Grieken. *X-ray Spectrometry: Recent Technological Advances*. WILEY, 2004.

[43] D.B. Wittry and D.M. Golijanin. Large Aperture Point-Focusing Diffractor for X-Rays. *APPLIED PHYSICS LETTERS*, 52(17):1381–1382, APR 25 1988. ISSN 0003-6951.

[44] D.B. Wittry and W.Z. Chang. Evaluation of Crystal Diffractor Parameters for Curved Diffractors. *JOURNAL OF APPLIED PHYSICS*, 72(8):3440–3446, OCT 15 1992. ISSN 0021-8979.

[45] D.B. Wittry and W.Z. Chang. Evaluation of Crystal Diffractor Parameters for Curved Diffractors. *JOURNAL OF APPLIED PHYSICS*, 73(2):601–607, JAN 15 1993. ISSN 0021-8979.

[46] D.B. Wittry and D. M. Golijanin. Alignment and characterization of doubly-curved X-ray diffractors. *Microbeam Analysis*, pages 51–55, 1987.

[47] Z.W. Chen. Recent development of doubly-curved crystal focusing optics and their applications for micro XRF. In MacDonald, CA and Goldberg, KA and Maldonado, JR and ChenMayer, HH and Vernon, SP, editor, *EUV, X-RAY, AND NEUTRON OPTICS AND SOURCES*, volume 3767 of *PROCEEDINGS OF THE SOCIETY OF PHOTO-OPTICAL INSTRUMENTATION ENGINEERS (SPIE)*, pages 114–120, 1000 20TH ST, PO BOX 10, BELLINGHAM, WA 98227-0010 USA, 1999. SPIE, SPIE-INT SOC OPTICAL ENGINEERING. ISBN 0-8194-3253-9. Conference on EUV, X-Ray, and Neutron Optics and Sources, DENVER, CO, JUL 21-23, 1999.

[48] C. Morawe, E. Ziegler, J.C. Peffen, and I.V. Kozhevnikov. Design and fabrication of depth-graded X-ray multilayers. *NUCLEAR INSTRUMENTS & METHODS IN PHYSICS RESEARCH SECTION A-ACCELERATORS SPECTROMETERS DETECTORS AND ASSOCIATED EQUIPMENT*, 493(3):189–198, NOV 11 2002. ISSN 0168-9002. doi: {10.1016/S0168-9002(02)01570-X}.

[49] E. Rutherford and H. Geiger. On the scattering of the α-Particles by matter. *PROCEEDINGS OF THE ROYAL SOCIETY OF LONDON A*, 81:174, 1908.

[50] G. Lutz. *Semiconductor Radiation Detectors*. SPRINGER, 1999.

[51] G. Knoll. *Radiation Detection and Measurement*. WILEY, 1999.

[52] E. Gatti, P. Rehak, and J.T. Walton. Silicon Drift Chambers - 1st Results and Optimum Processing of Signals. *NUCLEAR INSTRUMENTS & METHODS IN PHYSICS RESEARCH SECTION A-ACCELERATORS SPECTROMETERS DETECTORS AND ASSOCIATED EQUIPMENT*, 226(1):129–141, 1984. ISSN 0168-9002.

[53] V. Radeka, P. Rehak, S. Rescia, E. Gatti, A. Longoni, M. Sampietro, G. Bertuccio, P. Holl, L. Struder, and J. Kemmer. Implanted Silicon JFET on Completely Depleted High-Resistivity Devices. *IEEE ELECTRON DEVICE LETTERS*, 10(2):91–94, FEB 1989. ISSN 0741-3106.

[54] J. Kemmer, G. Lutz, U. Prechtel, K. Schuster, M. Sterzik, L. Struder, and T. Ziemann. Experimental Confirmation of a New Semiconductor Detector Principle. *NUCLEAR INSTRUMENTS & METHODS*

IN PHYSICS RESEARCH SECTION A-ACCELERATORS SPECTROMETERS DETECTORS AND ASSOCIATED EQUIPMENT, 288(1): 92–98, MAR 1 1990. ISSN 0168-9002. 5TH EUROPEAN SYMP ON SEMICONDUCTOR DETECTORS : NEW DEVELOPMENTS IN RADIATION DETECTORS, MUNICH, FED REP GER, FEB 21-23, 1988.

[55] C. Fiorini and P. Lechner. Continuous charge restoration in semiconductor detectors by means of the gate-to-drain current of the integrated front-end JFET. *IEEE TRANSACTIONS ON NUCLEAR SCIENCE*, 46(3, 3):761–764, JUN 1999. ISSN 0018-9499.

[56] European Space Agency, 12 2014. URL `http://sci.esa.int/ixo/43937-instruments/?fbodylongid=2060`.

[57] P. Lechner, A. Pahlke, and H. Soltau. Novel high-resolution silicon drift detectors. *X-RAY SPECTROMETRY*, 33(4):256–261, JUL-AUG 2004. ISSN 0049-8246. European Conference on EDXRS, BERLIN, GERMANY, JUN 16-21, 2002.

[58] U. Fano. Ionization yield of radiations. ii. the fluctuations of the number of ions. *Phys. Rev.*, 72:26–29, Jul 1947.

[59] H. Spieler. IEEE Short Course Radiation Detection and Measurement, Pulse Processing and Analysis. Pulse Processing and Analysis, 11 2002.

[60] H. Soltau, P. Holl, J. Kemmer, S. Krisch, C. vonZanthier, D. Hauff, R. Richter, H. Brauninger, R. Hartmann, G. Hartner, N. Krause, N. Meidinger, E. Pfeffermann, C. Reppin, G. Schwaab, L. Struder, J. Trumper, E. Kendziorra, and J. Kramer. Performance of the pn-CCD X-ray detector system designed for the XMM satellite mission. *NUCLEAR INSTRUMENTS & METHODS IN PHYSICS RESEARCH SECTION A-ACCELERATORS SPECTROMETERS DETECTORS AND ASSOCIATED EQUIPMENT*, 377(2-3):340–345, AUG 1 1996. ISSN 0168-9002. 7th European Symposium on Semiconductor Detectors, SCHLOSS ELMAU, GERMANY, MAY 07-JUL 10, 1995.

[61] E. Pinotti, H. Brauninger, N. Findeis, H. Gorke, D. Hauff, P. Holl, J. Kemmer, P. Lechner, G. Lutz, W. Kink, N. Meidinger, G. Metzner, P. Predehl, C. Reppin, L. Struder, J. Trumper, C. Vonzanthier, E. Kendziorra, R. Staubert, V. Radeka, P. Rehak, G. Bertuccio, E. Gatti, A. Longoni, A. Pullia, and M. Sampietro. The PN-CCD

On-chip Electronics. *NUCLEAR INSTRUMENTS & METHODS IN PHYSICS RESEARCH SECTION A-ACCELERATORS SPECTROMETERS DETECTORS AND ASSOCIATED EQUIPMENT*, 326(1-2): 85–91, MAR 1 1993. ISSN 0168-9002. 6TH EUROPEAN SYMP ON SEMICONDUCTOR DETECTORS, MILAN, ITALY, FEB 24-26, 1992.

[62] P. Lechner, R. Hartmann, P. Holl, G. Lutz, N. Meidinger, R.H. Richter, H. Soltau, and L. Struder. X-ray imaging spectrometers in present and future satellite missions. *NUCLEAR INSTRUMENTS & METHODS IN PHYSICS RESEARCH SECTION A-ACCELERATORS SPECTROMETERS DETECTORS AND ASSOCIATED EQUIPMENT*, 509(1-3): 302–314, AUG 21 2003. ISSN 0168-9002. 4th International Workshop on Radiation Imaging Detectors, AMSTERDAM, NETHERLANDS, SEP 08-12, 2002.

[63] L. Struder, H. Brauninger, M. Meier, P. Predehl, C. Reppin, M. Sterzik, J. Trumper, P. Cattaneo, D. Hauff, G. Lutz, K.F. Schuster, A. Schwarz, E. Kenziorra, A. Staubert, E. Gatti, A Longoni, M. Sampietro, V. Radeka, P. Rehak, S. Rescia, P.F. Manfredi, W. Buttler, P. Holl, J. Kemmer, U. Prechtel, and T. Ziemann. The MPI AIT X-ray Imager (MAXI) - High-Speed PN CCDS for X-ray-Detection. *Nuclear Instruments & Methods in Physics Research Section A-Accelerators Spectrometers Detectors and Associated Equipment*, 288(1):227–235, MAR 1 1990. ISSN 0168-9002. 5th European Symp on Semiconductor Detectors : New Developments in Radiation Detectors, Munich, Fed Rep Ger, FEB 21-23, 1988.

[64] U. Wiesemann, J. Thieme, P. Guttmann, B. Niemann, D. Rudolph, and G. Schmahl. The new scanning transmission x-ray microscope at bessy ii. *AIP Conference Proceedings*, 507(1):430–434, 2000.

[65] G. Bertschinger, W. Biel, O. Herzog, J. Weinheimer, H.J. Kunze, M. Bitter, and TEXTOR-94 Team. X-ray spectroscopy at the TEXTOR-94 tokamak. *PHYSICA SCRIPTA*, T83:132–141, 1999. ISSN 0281-1847. 6th International Colloquium on Atomic Spect and Oscillator Strengths (ASOS 6), UNIV VICTORIA, VICTORIA, CANADA, AUG 09-13, 1998.

[66] F. Lindner, W. Stremme, M.G. Schatzel, F. Grasbon, G.G. Paulus, H. Walther, R. Hartmann, and L. Struder. High-order harmonic generation at a repetition rate of 100 kHz. *PHYSICAL REVIEW A*, 68(1), JUL 2003. ISSN 1050-2947.

[67] M.N. Boone, J. Garrevoet, P. Tack, O. Scharf, D.P. Cormode, D. Van Loo, E. Pauwels, M. Dierick, L. Vincze, and L. Van Hoorebeke. High spectral and spatial resolution X-ray transmission radiography and tomography using a Color X-ray Camera. *Nuclear Instruments & Methods in Physics Research Section A-accelerators Spectrometers Detectors and Associated Equipment*, 735:644–648, JAN 21 2014. ISSN 0168-9002.

[68] M. Van Gysel, P. Lemberge, and P. Van Espen. Description of Compton peaks in energy-dispersive x-ray fluorescence spectra. *X-RAY SPECTROMETRY*, 32(2):139–147, MAR-APR 2003. ISSN 0049-8246. doi: {10.1002/xrs.628}.

[69] S.J.B. Reed and N.G. Ware. Escape Peaks and Internal Fluorescence in X-ray-Spectra Recorded with Lithium Drifted Silicon Detectors. *JOURNAL OF PHYSICS E-SCIENTIFIC INSTRUMENTS*, 5(6):582–&, 1972. ISSN 0022-3735. doi: {10.1088/0022-3735/5/6/029}.

[70] B. Vekemans, K. Janssens, L. Vincze, F. Adams, and P. Vanespen. ANALYSIS OF X-RAY-SPECTRA BY ITERATIVE LEAST-SQUARES (AXIL) - NEW DEVELOPMENTS. *X-RAY SPECTROMETRY*, 23(6):278–285, NOV-DEC 1994. ISSN 0049-8246.

[71] C.G. Ryan, D.N. Jamieson, C.L. Churms, and J.V. Pilcher. A New Method for Online True-Elemental Imaging Using PIXE and the Proton Microprobe. *NUCLEAR INSTRUMENTS & METHODS IN PHYSICS RESEARCH SECTION B-BEAM INTERACTIONS WITH MATERIALS AND ATOMS*, 104(1-4):157–165, SEP 1995. ISSN 0168-583X. doi: {10.1016/0168-583X(95)00404-1}. 4th International Conference on Nuclear Microprobe Technology and Applications, SHANGHAI INT HOUSE EDUC, SHANGHAI, PEOPLES R CHINA, OCT 10-14, 1994.

[72] C.G. Ryan. Quantitative trace element imaging using PIXE and the nuclear microprobe. *INTERNATIONAL JOURNAL OF IMAGING SYSTEMS AND TECHNOLOGY*, 11(4):219–230, 2000. ISSN 0899-9457. doi: {10.1002/ima.1007}.

[73] J Sherman. The Theoretical Derivation of Fluorescent X-ray Intensities from Mixtures. *SPECTROCHIMICA ACTA*, 7(5):283–306, 1955. doi: {10.1016/0371-1951(55)80081-1}.

[74] N. Metropolis and S. Ulam. The Monte Carlo Method. *Journal of American Statistical Association*, 11(247):335–341, 1949.

[75] L. Vincze, K. Janssens, F. Adams, and K.W. Jones. A general monte carlo simulation of energy-dispersive X-ray fluorescence spectrometers .3. Polarized polychromatic radiation, homogeneous samples. *SPECTROCHIMICA ACTA PART B-ATOMIC SPECTROSCOPY*, 50 (12):1481–1500, OCT 1995. ISSN 0584-8547.

[76] T. Schoonjans, V.A. Sole, L. Vincze, M. S. del Rio, K. Appel, and C. Ferrero. A general Monte Carlo simulation of energy-dispersive X-ray fluorescence spectrometers - Part 6. Quantification through iterative simulations. *SPECTROCHIMICA ACTA PART B-ATOMIC SPECTROSCOPY*, 82:36–41, APR 1 2013. ISSN 0584-8547.

[77] D. Roet. *Monte carlo simulation of the electron-solid interaction with emphasis on scanning electron microscopy*. PhD thesis, University of Antwerp, 2011.

3

SLcam®: An Energy Dispersive pnCCD Pixel Detector

This chapter describes the SLcam®, a pixelated energy dispersive Si based X-ray detector named after the two people in charge of the companies which are responsible for the development of the detector, Strüder and Langhoff. Although first developed for space studies on board of space crafts, the detector chips were quickly altered for laboratory or synchrotron based X-ray experiments. The detector is based on a pnCCD chip which was explained in detail in Section 2.5.4. The development of a pixelated energy dispersive detector opens up new possibilities towards XRF elemental imaging by the simultaneous acquisition of several thousands pixels, speeding up the typical scanning type process. Although photon counting detectors can have several discrete energy intervals by using an energy threshold, the described detector can collect a full energy dispersive spectrum per individual pixel. First, a general overview of the SLcams design and hardware is given. Secondly, the characteristics will be discussed, showing the capabilities and limitations of this detector in order to used it to its full potential.

3.1 Detector Design and Hardware

As in a conventional CCD, a pnCCD can also be designed in a frame store format. This design allows for faster readout times by optimising the ratio of exposure to transfer time at the cost of a smaller active area since part of the chip serves as an analogue storage region. The chip used in the SLcam® contains 528 columns by 264 rows of which 264 columns and 264 rows are used as imaging area while the remaining area is used as frame store area which is located at both sides of the chip to speed up the readout, see Figure 3.1. To avoid illumination of the frame store area, the radiation shield is constructed slightly larger, shielding part of the imaging area (8 pixel rows at either side in the transfer direction and 4 pixel rows at either side in the perpendicular direction to the transfer direction). The so comprised image area consists of 248 by 256 pixels of $48^2\,\mu\mathrm{m}^2$. Each half image is thus transferred to its X-ray shielded storage area located at opposites side of the imaging area. Charge transfer, which takes $50\,\mu\mathrm{s}$, of the electrons to the neighbouring pixel occurs with a charge transfer efficiency of > 0.99995. The pnCCD performs the readout for all pixels of a single row simultaneously while an integrated JFET provides the first signal amplification of the charge signals. Further processing is performed by four CAMEX chips (two per side) which are wire bonded to the output of the JFET amplifiers, seen on Figure 3.2. Due to the presence of four CAMEX chips, therefore the chip is virtually divided into four independent quadrants. A frame rate of $400\,\mathrm{Hz}$ is achieved with the SLcam® discussed in this dissertation, while an update was released that provides a frame rate of $1000\,\mathrm{Hz}$ using a special CAMEX reset mode[2]. Due to the detector's sensitive thickness of $450\,\mu\mathrm{m}$ and $50\,\mu\mathrm{m}$ thick Be window, the quantum efficiency is above $95\,\%$ in range of 3 to $10\,\mathrm{keV}$ and above $30\,\%$ up to $20\,\mathrm{keV}$, see Figure 3.3[3]. A virtual cross-section of the SLcam® is shown in Figure 3.4. On the front (top of Figure 3.4) of the housing a flange is located so different available optics can be mounted. Currently available optics are polycapillary optics, pinholes, and slits, although future technological advances might make Fresnel zone plate optics a valuable candidate. The pnCCD of the SLcam® is housed in a vacuum housing ($< 1\,\mathrm{mbar}$) to avoid condensation by thermal decoupling. A Be window of $50\,\mu\mathrm{m}$ thick is used as an X-ray transparent window as a separator between the vacuum inside the housing and the atmospheric pressure from the experimental surrounding. The pnCCD itself is located $6.2\,\mathrm{mm}$ below the Be window an is illuminated from the back side (not visible in Figure 3.2. To minimise dark current, the pnCCD is operated at approximately $-20^{\circ}\mathrm{C}$ for optimal performance, which results in a noise contribution due to dark current of $ENC < 1\,\mathrm{e}^-/_{\mathrm{pixel}}$. Cool-

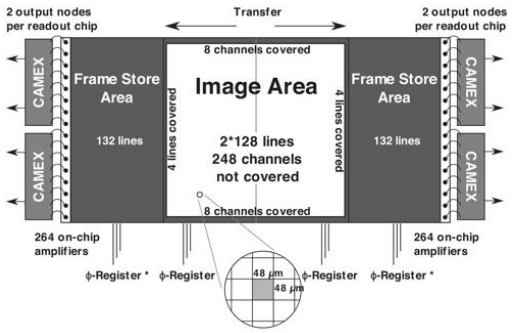

Figure 3.1: A schematic cross-section through the pnCCD along a transfer channel. Adapted from [1].

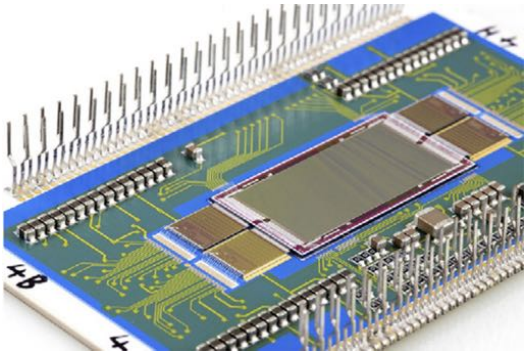

Figure 3.2: Photograph showing the front side of the pnCCD along with the four CAMEX chips mounted on a ceramic multilayer module. Adapted from [3].

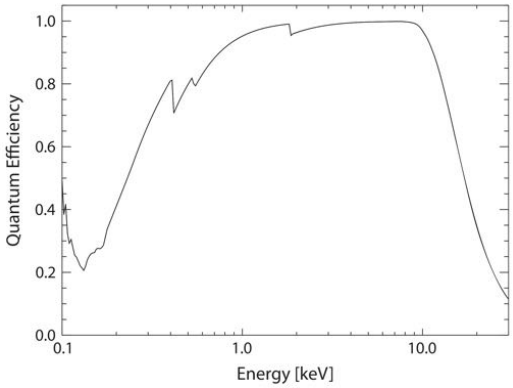

Figure 3.3: Quantum efficiency of the SLcam® 450 µm thick Si chip. Adapted from [3].

ing is provided by two double-stage Thermoelectric Modules (TEC) each with a cooling capacity of $45\,\mathrm{W}$. The small spacing between the pnCCD and the housing as well as the spacing between the ceramic board and the electronics boards, provided by 110 pins, requires that the Peltier modules are placed at the sides of the ceramic and thermally connected using three cooling masks. The heat of the warm sides of the Peltier coolers is dissipated by cooling water of $\leq 8^{\circ}\mathrm{C}$ running through a copper block. The housing is equipped with several sensors, providing information on Peltier cold and hot side temperature, cooling water temperature, vacuum pressure and humidity. On the back of the vacuum housing, an electronics housing is located (not shown on Figure 3.4, which also provides the necessary electronic connections to the electronic system, located in a 19" rack. The 19" rack houses power supplies, the sequencer, and the data acquisition system and is hooked up to an Uninterruptable Power Supply (UPS) to protect the system to damages due to possible power failures. The power supplies are digitally programmable to allow for voltage ramping and voltage customisations for different operating modes of the pnCCD and CAMEX. The before mentioned sequencer is a fully software-programmable pattern generator which is responsible for the digital pulses needed for the shift registers in the pnCCD chip, clocks which control the signal amplification in the CAMEX chips, and clocks for the ADC boards. The analogue output signals of the four CAMEX chips are processed in parallel by four ADC boards to a 16 bit word with a 14 bit resolution. The now digital signal (approximately $450\,\mathrm{Mb/s}$) is transmitted via a fibre optic serial connection to the control computer for further processing.

3.2 Acquisition Software

The acquisition software is responsible for the control of the power supplies, the readout electronics, monitoring systems, data analysis, preliminary visualisation, and data storage. Due to this wide variety of functionality the software consists out of 3 main components: Housekeeping, iXcc driver, and the Imaging Software. The software is written in C++ using the Qt[5] and the Qwt[6] while the event analysis is based upon XOnline[7].

3.2.1 Housekeeping

The Housekeeping software is responsible for startup, monitoring and shut down of the SLcam®. During startup, the pnCCD chip needs to be cooled down first before the different voltage can be applied. The temperature needs to be decreased gradually to prolong the lifetime of Peltier elements.

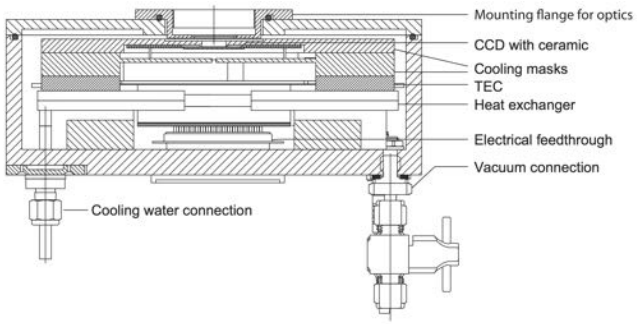

Figure 3.4: Virtual cross-section of the SLcam® vacuum housing showing the chip location, cooling geometry using masks, Peltier elements TEC and a water cooled heat exchanger. Adapted from [3].

Parameter	Value
pnCCD type	Split frame readout
Pixel Size	$48^2\,\mu\mathrm{m}^2$
Number of Pixels	(264×264) 69696
Imaging Area	$12.7 \times 12.7\,\mathrm{mm}^2$
Sensitive Thickness	$450\,\mu\mathrm{m}$
Frame Rate	$400\,\mathrm{Hz}$ (Type 1) / $1000\,\mathrm{Hz}$ (Type 2)
Pixel Readout Speed	$27.9\,{}^{\mathrm{MP}}/_{\mathrm{s}}$ (Type 1) / $69.7\,{}^{\mathrm{MP}}/_{\mathrm{s}}$ (Type 2)
Quantum Efficiency	$> 95\,\%$ at $3 - 10\,\mathrm{keV}$; $> 30\,\%$ at $20\,\mathrm{keV}$
Readout Noise (RMS)	$< 3\,{}^{\mathrm{e}^-}/_{\mathrm{pixel}}$
Charge Transfer Efficiency	> 0.99995
Full Well Capacitance	$10^5\,\mathrm{e}^-$

Table 3.1: Main characteristics of the SLcam® [3, 4].

Depending on the working window, 10 - 15 - 20 - 40 keV, the amplifier bandwidth and the analogue gain is set. During operation it monitors voltages, temperatures and humidity to ensure correct operation of the pnCCD chip. When one of the values drifts outside the working window the detector is shut down automatically to avoid damage to the detector.

3.2.2 iXcc driver

The iXcc driver is the software link between the hardware readout and the imaging software and is responsible for the event analysis. The received data is temporarily stored in what is called a frame buffer to enable the event analysis which is needed since the charge cloud generated by X-rays with energies above 3 keV have a high probability to spread along its drift path towards the front of the device. Therefore, the charge cloud originating from a single event will be recorded by multiple neighbouring pixels without any loss in charge, depicted in Figure 3.5. The size of the charge cloud can be explained by diffusion and electrostatic repulsion, which causes a Gaussian sphere with sigma σ_{diff} and a sphere with radius r_{ER}[8].

$$\sigma_{diff}(t) = \sqrt{\frac{2kT}{e} \cdot \mu_n t} \tag{3.1}$$

$$r_{ER}(t) = \sqrt[3]{\frac{3\mu_n N_e}{4\pi\epsilon} \cdot t} \tag{3.2}$$

with k the Boltzmann constant, T the temperature of the material, e the elemental charge, μ_n the mobility, ϵ the permittivity in the chip material (Si in the case of the SLcam®), and t the drift time, which is given by[8]:

$$t(\Delta x) = \frac{-1}{\mathcal{E}'(x_0) \cdot \mu_n} \ln\left(\frac{\mathcal{E}(x_0) + \mathcal{E}'(x_0) \cdot \Delta x}{\mathcal{E}(x_0)}\right) \tag{3.3}$$

with $\mathcal{E}$ the electric field, and Δx the drift distance[1] The electron mobility μ_n is cancelled out in Equations 3.1 and 3.2, making the size of the charge cloud only a function of the drift distance (Δx), the electric field $\mathcal{E}$ and its derivative $\mathcal{E}'$. Due to the possible distribution of the charge cloud (signal electrons) over multiple pixels (depicted in Figure 3.5), the iXcc driver analyses each event which is detected by the detector and determines the centre of gravity of the charge cloud using the centroid method, Figure 3.6. Besides the determination of the centre of gravity of the charge cloud, the

[1] Since per definition the readout takes place at $x = 0$, the drift distance is always negative.

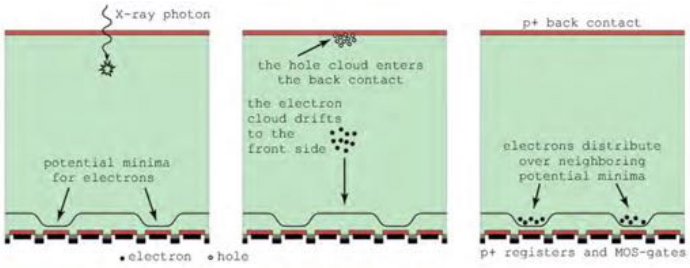

Figure 3.5: The charge collection in a pnCCD, the absorbed X-ray photon is absorbed in the detector active material and converted in an electron charge cloud. A potential causes the charge cloud to drift to the register side, distribution the charge cloud over neighbouring pixels when close to the pixel boarders. Adapted from [8].

total deposited energy needs to be calculated as well. The efficiency of this method is dependant on the photon count rate hitting the detector. Once the count rate reaches a certain threshold, event patterns will start overlapping, preventing the reconstruction of the centre of gravity and exact energy of the photon, leading to pulse pileup or skipped events. Since the accuracy of the determination of the centre of gravity is more spatially resolved than the size of the on chip pixels, one could obtain higher resolution elemental distribution images. An oversampling using sub-pixel resolution has already been shown promising results using a factor of 4, achieving a theoretical pixel resolution of $12\,\mu\mathrm{m}$, but was experimentally limited to $17\,\mu\mathrm{m}$ due to the capillary diameter[3]. Abboud et al. [9], showed the possibility to achieve sub-pixel resolution below $2\,\mu\mathrm{m}$ using a pnCCD with $72^2\,\mu\mathrm{m}^2$ pixels. Since the achievable sub-pixel resolution is solely dependant on the pixel size of the chip and the charge cloud size, the sub-pixel resolution will be photon energy dependant since the size of the charge cloud increases with photon energy[9]. However, an optimum exists between charge cloud size and pixel size due to the association with a certain ratio of split events. In particular, triple and quadruple events can be used to improve the positioning of a certain X-ray photon impact. Single and double events do not yield extra spatial information (doubles only provide one dimensional information). The reconstruction of the charge cloud is done using a rectangular model to approximate the Gaussian/circular convolution distribution (see Equation 3.1 And 3.2)[9, 10]. Based on this rectangular model of the charge cloud, the centre can then be calculated using the splitting ratios (A_1,A_2,A_3, A_4) of the charge cloud of the neighbouring pixel, see Figure

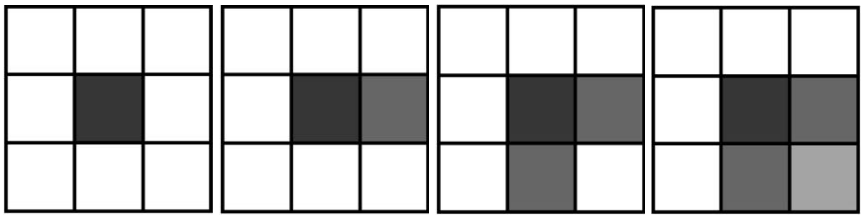

Figure 3.6: Topologies of valid photon event patterns, depicting following events: (a) single; (b) double; (c) triple; (d) quadruple. Each 90° *permutation about the centre of gravity is also valid. Darker shade of gray indicate a higher charge. Adapted from [8].*

3.7, using[9]:

$$x_{sub} = \sqrt{\frac{A_1 + A_2 + A_3 + A_4}{\pi}} \cos\left(\sqrt[3]{\frac{3}{2R^2}(A_3 + A_4)}\right) \tag{3.4}$$

$$y_{sub} = \sqrt{\frac{A_1 + A_2 + A_3 + A_4}{\pi}} \cos\left(\sqrt[3]{\frac{3}{2R^2}(A_2 + A_3)}\right) \tag{3.5}$$

The choice of number of sub-pixels is only limited by the computing time, memory and the total available photons. Especially this last parameter should be taken into account due to the rapid deterioration of the pixel statistics. Therefore, the sub-pixel resolution is often limited by the available photon flux or the count rate capabilities of the detector, which is directly correlated to the readout speed of the detector.

3.2.3 Imaging Software

The part of the software is the main graphical interface for the end user of the detector system, used for calibration, visualisation, analysis and saving of the data. The main features of the Graphical User Interface (GUI), located under several tabs, are:

- Guidance for dark field and constant gain correction and transfer efficiency measurements;
- Dectector status, showing additional information on the use of the detector: load, skip map, total energy map, RAW frame, total count rate, events per frame;

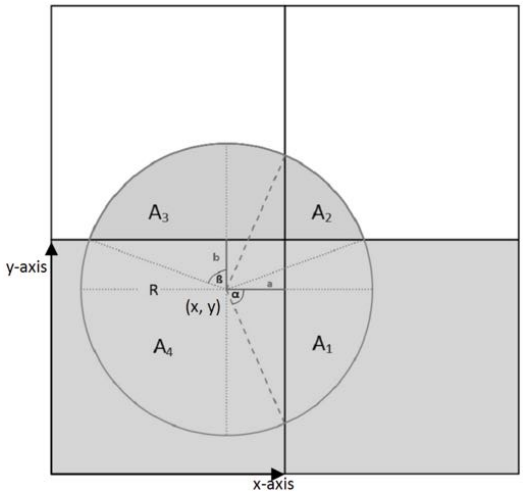

Figure 3.7: Charge cloud representation, showing the distribution, with radius R, for a split event over neighbouring pixels, A_1, A_2, A_3 and A_4 the splitting ratios, the X-ray photon impact point (x,y). Adapted from [9].

- The currently measured sum spectrum of the entire chip is shown, allowing the user to select ROIs, or select predefined ROIs using the periodic table, to allow ROI online imaging;
- Remote TCP/IP control so the detector can be controlled by other instrumentation or can for example be integrated into a beamline;
- Automated image recording and saving for a completely independent measurement setup.

3.2.4 Data format

The eventual measurement data is saved in Hierarchical Data Format 5 (HDF5) format (open source) for its versatility towards complex data models and support a wide variety of metadata and is unlimited in data objects or size. HDF5 has linkers and tools for most languages, is highly parallel and has optimisation algorithms to increase performance, making it a cross platform and versatile file format, which is becoming the standard file format at particle accelerators around the world. The first version of the Imaging Software roughly saved 1 GB files per measurement (depending on the total amount of events). However, after implementation of the HDF5 format, the file size decrease with a factor of ≈ 200. The saved HDF5 file

contains the 3D data array ($264 \times 264 \times 1024$) and contains several other useful additional data as:

- The sum spectrum over all pixels;
- The header which contains measurement time, duration, total number of events, total number of frames, calibration gain and offset, count rate and user defined comment;
- The energy integration image, showing a pixel map with the total registered energy per pixel, and is similar to an image acquired by an energy integrated detector, like a scintillator based detector;
- The hits image, containing the number of valid photons events were registered per pixel, which corresponds to an image which one would obtain from a photon counting detector, like the MAXIPIX[11];
- The skip image, showing an image containing information on the pixel level on the amount of events that were rejected by the centroid algorithm.

Besides the HDF5 data file, separate ROI image in jpg format can be saved alongside the header information in clear text format for the less advanced user.

3.2.5 New and Future Additions

3.2.5.1 Out of Time Events

Operating a pnCCD in frame store mode reduces the dead time between the integration periods but allows photons to hit the pnCCD during the readout phase. These photon events will be detected but their coordinate in the transfer direction will be incorrect, which has an impact on the energy information accuracy due to the incorrect charge transfer efficiency (CTE) correction, based on the position along the readout direction, which is applied. Photons events which occur during the readout are called Out of Time (OOT) Events and show up as stripes in images which contain local hot spots, shown in Figure 3.8. The principle is shown in Figure 3.9, where a source irradiates one pixel on the pnCCD chip. Figure 3.9a shows photons hitting the detector in one pixel during the integration time of the first frame. Therefore, the position information of the photon event is correct. In Figures 3.9b and 3.9c show photon impacts during the readout of frame one. Showing that the photon event will be registered but will have a wrong position coordinate along the readout direction. Figure 3.9d shows

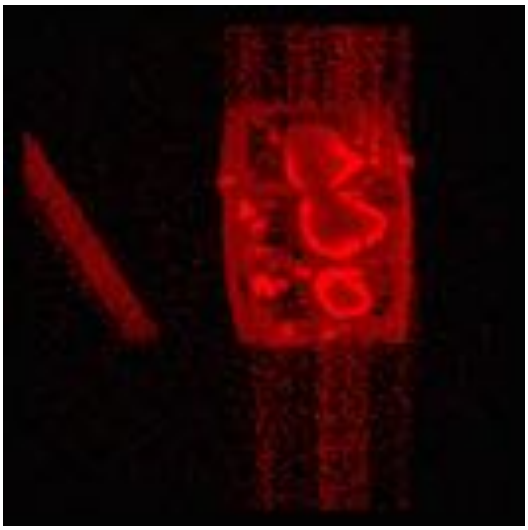

Figure 3.8: The presence of Out of Time Events in an image, characterised by the appearance of lines originating from local hot spots.

the acquisition of the next frame. The fraction of OOT Events is determined by the ratio of the transfer time and the total exposure time per frame, meaning that the SLcam® has the following OOT fraction[13]:

$$n_{OOT} = \frac{t_{transfer}}{t_{readout}} = \frac{2.5 \cdot 10^{-3}\,\mathrm{s}}{5 \cdot 10^{-6}\,\mathrm{s}} = 0.2\,\% \tag{3.6}$$

3.2.5.2 Sub-pixel Resolution

Sub-pixel resolution, which was explained in Section 3.2.2, will be added to the imaging software without the need of operating the detector in RAW frame mode. The RAW frame mode saves the raw data from the detector to the hard drive without any processing of the photon events. This means that the full data stream of about $75\,\mathrm{MB/s}$ for the $400\,\mathrm{Hz}$ model has to be written to the hard disk. Sustainable writes of this steam of data requires a redundant array of inexpensive disks (RAID) array of several TB in size to be able to provide enough storage for a typical measurement time at a synchrotron source ($4\,\mathrm{days} = 25\,\mathrm{TB}$). Because of the load on the measurement computer, sub-pixel analysis could only be performed offline. An online methodology is being sought for, to allow the user to both visualise the currently measured data and allowing sub-pixel resolutions to be achieved.

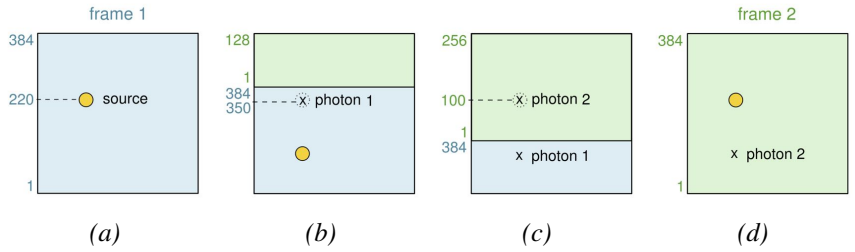

Figure 3.9: Illustrating the cause of OOT events. (a) A photon hits the chip during integration of the first frame. (b), (c) illustrate the readout of frame 1, while photons still hit the chip at the same location as in (a) but as can be seen will have a wrong coordinate along the readout direction. (d) integration of the next frame. Adapted from [12].

3.2.5.3 TCP/IP Communication

The TCP/IP communication will be extended to improve the incorporation of the system into beamlines and other measurement systems. Besides the current available features like Start, Stop and Save, options to set comments and the filename will be added.

3.3 Detector Characterisation

3.3.1 Count Rate

As reported by Ordavo et al. [3] and Scharf et al. [4], the $400\,\mathrm{Hz}$ model is capable of $450\,\mathrm{kcps}$ when homogeneously illuminated with a $17\,\mathrm{keV}$ beam. The main limiting factor to the achievable count rate is the necessity to be able to distinguish events, the statistical probability of two charge clouds to overlap. Partial saturation can already occur at much lower total count rates but where areal photon count rates are above the saturation threshold. Next to that, the count rate is also depending, although to a lesser extent, on the photon energy due to the Full Well Capacitance ($10^5\,\mathrm{e}^-$, see Table 3.1), which will be reached quicker for higher energy photons. Furthermore, the charge cloud will be smaller for lower energy photons, influencing the statistical probability of two charge clouds to overlap, see Equation 3.2. During XRF spectroscopy measurements, count rates of $450\,\mathrm{kcps}$ were almost never obtained due to the low concentrations in most samples but one should pay attention to locally overloading the chip when samples contain hot spots. Therefore, the experimentalist has to keep an eye on the skip

map, shown in the Imaging Software (Section 3.2.3). An elaborate study on the count rate response of the SLcam® has been performed by Boone [14], showing a linear correlation between deposited energy rate and X-ray tube current, however due to count rate limitations imposed by pulse pile-up and rejected events, the count rate as a function of the energy deposited rate is non linear. Similar detector behaviour is seen in SDDs when reaching their maximum count rate.

3.3.2 Event Distribution

As already reported by Scharf et al. [4], the most frequent pixel event is the quadruple event, which make up for more than $40\,\%$ of the total recorded events during normal operation of the detector. Once the detector is pushed to its maximum capabilities in respect of count rate or the average energy of the incoming photons increases, the larger the contribution of quintuple to octuple events are being detected[14].

3.3.3 Readout Quadrants

As mentioned before, the chip of the SLcam® is readout by 4 CAMEX chips, which each have slightly different properties. Before a measurement can be performed a calibration of these CAMEX chips is necessary to trim the gain of each CAMEX to give a homogeneous response. To test the homogeneous response of the detector chip it was homogeneously illuminated by an ^{55}Fe source for $120\,\mathrm{h}$. Figure 3.10 shows the presence of the slight offset between the different CAMEX chips, especially the region (line) in the middle of the chip where the readout zones meet. Due to the different calibration of the different readout zones, the centroid method used for the event reconstruction, is applied for each transfer zone separately. Shared events between different readout zones should therefore be treated with special care, applying different weights due to the different readout zones for an accurate reconstruction of the photon event. The difference between the readout zones becomes more apparent at higher energies, leading to the believe that the calibration of the four CAMEX chips and therefore used parameters in the event reconstruction algorithm are inaccurate. The parameters are determined using the calibration process of the detector, determining the dark noise, charge transfer efficiency and the gain/offset of each CAMEX chip. The control software provides the possibility to set the average events per pixel during this calibration process. Although this is currently not examined yet, or reported by any of the collaborators, one would expect less variance between pixels and quadrants

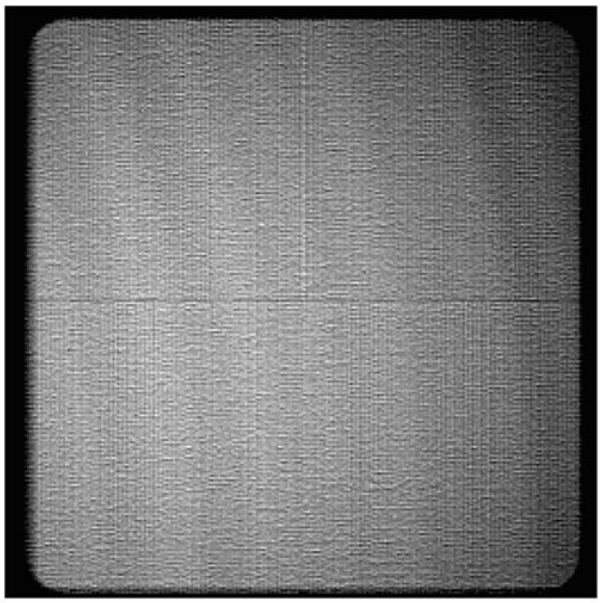

Figure 3.10: The Mn-Kα line image of the ^{55}Fe source, indicating the radiation shield that covers the readout nodes and the small offset between the different readout quadrants. Image was scaled to improve visibility.

when using a higher average number of events, improving the statistics of the calibration procedure.

The total number of counts of the Mn-Kα was used to determine the mean and standard deviation of each quadrant after calibration of the CAMEX chips, shown in Table 3.2. The pixels that were shielded by the radiation shield were not taken into account by using a ROI threshold. Although the variation is less than $5\,\%$ between the different quadrants, one still needs to correct for this effect. The inter pixel variation,a measure for the homogeneous response of the detector and the stability of each pixel, is about $4\,\%$. A more elaborate study of the pixel response is shown by Boone [14], focussing more on the application of the detector in spectral radiography.

3.3.4 Pulse Pile-up

Unlike for SDDs, where pulse pile-up is caused by the temporal overlap of two pulses anywhere on the active area, pulse pile-up only arises when the formed charge cloud meets a valid size and pixel distribution for the centroid method, determining the centre of gravity of the photon event. Once these criteria are met, pulse pile-up will be visible in the energy spec-

Quadrant	1	2	3	4
Mean	102.93	98.75	101.16	97.16
σ	3.37	3.86	3.79	3.95

Table 3.2: Normalised counts of the Mn-Kα peak after homogeneous illumination by an ^{55}Fe source, showing the variation between the 4 CAMEX chips after calibration.

trum. Due to the statistical nature of pulse pile-up, this effect can be incorporated into the spectrum deconvolution algorithm.

To study the response of the SLcam®, an ^{55}Fe source was mounted in front of the bare chip which was cooled to $-20°\mathrm{C}$, resulting in a Count Rate (CR) of about $13\,\mathrm{kcps}$, and was exposed for $120\,\mathrm{h}$, showing not only pulse pile-up but also escape peaks arising in the spectrum, see Figure 3.11. If pulse pile-up forms a problem due to overlap with elements of interest,

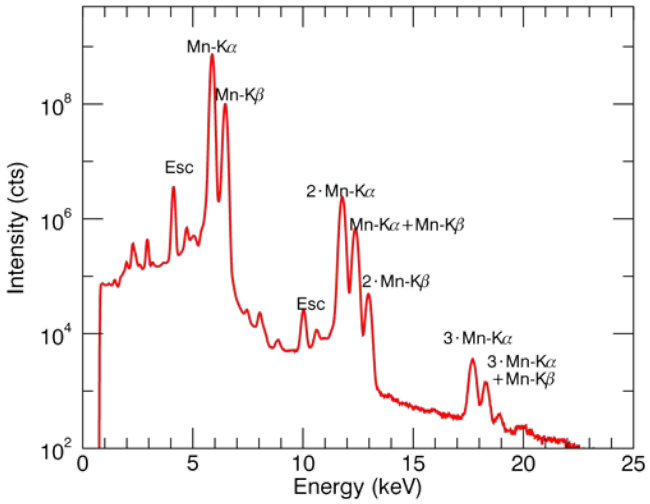

Figure 3.11: Spectrum of an ^{55}Fe acquired over $120\,\mathrm{hours}$, showing the characteristic Mn lines, escape peaks and pulse pile-up effect. Detailed info can be found in Table 3.3.

one has to reduce the incoming photon flux if the data is to be used for quantitative analysis. One could also change the event analysis to only take into account smaller charge clouds. Since this will lead to skipped events, there is no linear correlation any more between the net peak intensity and concentration of the elements in question, making the data only

Peak	Energy (keV)	Net Intensity	Relative Intensity
Mn-Kα	5.89	$4.61 \cdot 10^9$	–
Mn-Kβ	6.49	$4.74 \cdot 10^8$	–
2 $\cdot$ Mn-Kα	11.78	$2.40 \cdot 10^7$	$5.2 \cdot 10^{-3}$
Mn-Kα + Mn-Kβ	12.38	$4.94 \cdot 10^6$	$9.7 \cdot 10^{-4}$
2 $\cdot$ Mn-Kβ	12.98	$2.54 \cdot 10^5$	$5.4 \cdot 10^{-4}$
Mn-Kα esc	4.15	$1.93 \cdot 10^7$	$4.2 \cdot 10^{-3}$
Mn-Kβ esc	4.75	$1.58 \cdot 10^6$	$3.3 \cdot 10^{-3}$

Table 3.3: Pulse pile-up and escape peak analysis of the SLcam® of a spectrum of an ^{55}Fe source measured for $120\,\mathrm{h}$ *(CR =* $13\,\mathrm{kcps}$*), showing peak positions and relative intensities.*

usable for qualitative analysis. Future developments, by improving the chip readout time ($2.5\,\mathrm{ms}$ for the $400\,\mathrm{Hz}$ model) to below the millisecond range would drastically improve the pulse pile-up effect. The current version of the SLcam® has a $1000\,\mathrm{Hz}$ readout speed, improving the pulse pile-up response but decreasing the energy resolution (see Section 3.3.5) due to increased readout noise level, a similar effect as changing the Peaking Time (PT) of an SDD detector.

3.3.5 Energy Resolution

Ordavo et al. [3] and Scharf et al. [4] state an energy resolution (ER) of $152\,\mathrm{eV}$ at the Mn-Kα line ($5.90\,\mathrm{keV}$) for a sum spectrum of all the illuminated pixels by the used ^{55}Fe source. To study the ER per pixel and its distribution, the same measurement was used as explained in Section 3.3.4. A four factor Gaussian (see Appendix A) was used to fit the Mn-Kα peak (Figure 3.11). The ER is defined as the FWHM of the peak in question, see section 2.5.3.2. A pixel based ER image is shown in Figure 3.12, depicting the good energy response of this detector with an average ER of $156\,\mathrm{eV}$, which can be obtained by averaging of the ER based on a pixel spectrum or by Gaussian fit of the Mn-Kα peak from the sum spectrum of the entire detector. Figure 3.13 and Table 3.4 provide a statistical analysis of the obtained results, showing that more than $75\,\%$ of the pixels has an ER lower than $160\,\mathrm{eV}$, which is comparable to current SDDs operated at PTs of about $1\,\mu\mathrm{s}$.

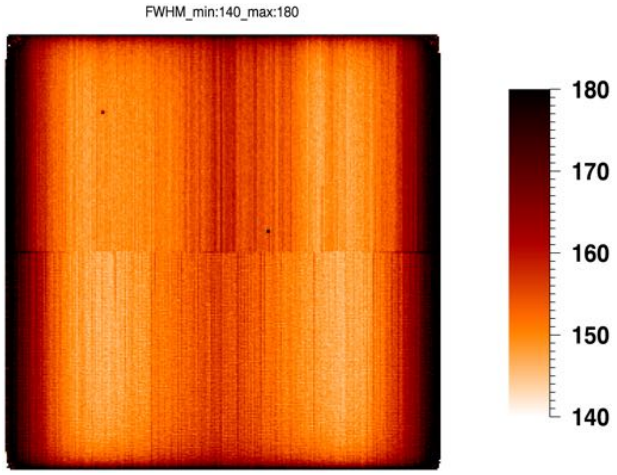

Figure 3.12: The energy resolution across the pnCCD chip based on the Mn-Kα peak.

ER Interval (eV)	# Pixels	Pixel %	Average (eV)	Error (eV)
$[140-200]$	68721	98.6	156	0.75
$[140-149]$	18300	26.3	148	0.56
$[150-159]$	36129	51.8	154	0.60
$[160-169]$	6868	9.9	164	0.76
$[170-179]$	4818	6.9	175	1.23
$[180-189]$	2052	2.9	185	2.51
$[190-199]$	554	0.8	194	6.68

Table 3.4: Detailed overview of the ER distribution at the Mn-Kα line ($5.90\,\mathrm{keV}$)

3.3.6 Energy Stability over Time

The energy response function of detectors can change over time due to fluctuations in their electrical systems, as temperature and voltage. The measurement of the ^{55}Fe source, described before, was used to study the centroid position of the Gaussian fitted to the Mn-Kα peak. The Gaussian centroid variation, shown in Figure 3.14, is not significant since the deviation is about equal to the energy width of a single channel ($\approx 25\,\mathrm{eV}$ in the $20\,\mathrm{keV}$ modus). The initial increase in centroid energy is probably due to the better fit of the Gaussian function, more accurately describing the

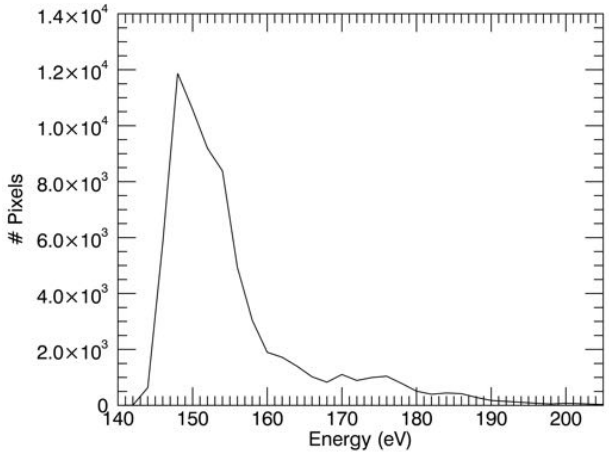

Figure 3.13: Histogram plot of the energy resolution (bin width = 2) based on the Mn-Kα peak.

Mn-Kα peak. Figure 3.15 shows the channel number of the peak centroid per pixel of the fitted Gaussian function, indicating the presence of a small calibration offset between each individual pixel. A remapping of the data cube, in the case of XRF measurements is not necessary since the deconvolution algorithm of AXIL[15] allows centroid shifting of the fitted function. In the case of spectral radiography, Boone [14] applied a remapping of the dataset to correct for these small offsets. The influence of the calibration step on the inter pixel variation is currently not investigated but as stated before, although one might expect a positive influence when using a higher average number of pixel events during the calibration step.

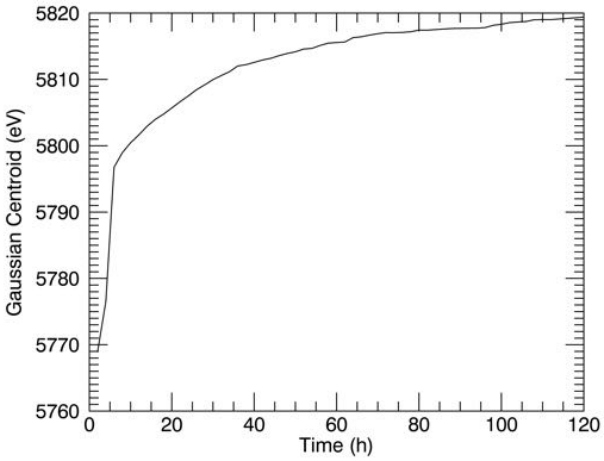

Figure 3.14: The evolution of the Mn-Kα peak centroid over time of which the variation is not significant since the deviation is about equal to the energy width of a single channel.

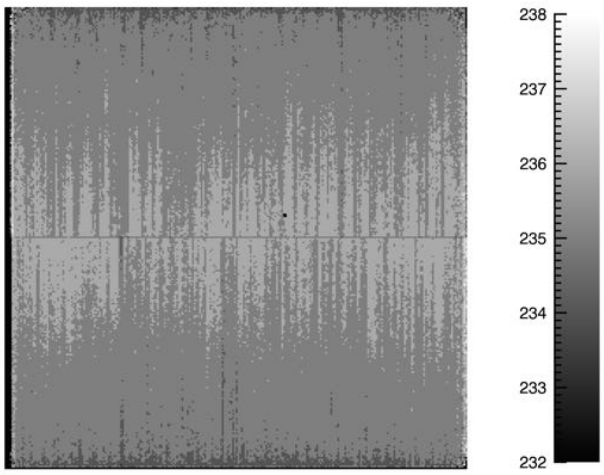

Figure 3.15: The channel number of the Mn-Kα peak centroid per pixel, showing a small offset between different pixels which is corrected for during the spectrum deconvolution algorithm.

References

[1] P. Lechner, R. Hartmann, P. Holl, G. Lutz, N. Meidinger, R.H. Richter, H. Soltau, and L. Struder. X-ray imaging spectrometers in present and future satellite missions. *NUCLEAR INSTRUMENTS & METHODS IN PHYSICS RESEARCH SECTION A-ACCELERATORS SPECTROMETERS DETECTORS AND ASSOCIATED EQUIPMENT*, 509(1-3): 302–314, AUG 21 2003. ISSN 0168-9002. 4th International Workshop on Radiation Imaging Detectors, AMSTERDAM, NETHERLANDS, SEP 08-12, 2002.

[2] S. Ihle, I. Ordavo, A. Bechteler, R. Hartmann, P. Holl, A. Liebel, N. Meidinger, H. Soltau, L. Strueder, and U. Weber. A compact, high-speed pnCCD camera for optical and X-ray applications. In Holland, AD and Beletic, JW, editor, *HIGH ENERGY, OPTICAL, AND INFRARED DETECTORS FOR ASTRONOMY V*, volume 8453 of *Proceedings of SPIE*, 1000 20TH ST, PO BOX 10, BELLINGHAM, WA 98227-0010 USA, 2012. SPIE, SPIE-INT SOC OPTICAL ENGINEERING. ISBN 978-0-8194-9154-1. doi: {10.1117/12.926997}. Conference on High Energy, Optical, and Infrared Detectors for Astronomy V, Amsterdam, NETHERLANDS, JUL 01-04, 2012.

[3] I. Ordavo, S. Ihle, V. Arkadiev, O. Scharf, H. Soltau, A. Bjeoumikhov, S. Bjeoumikhova, G. Buzanich, R. Gubzhokov, A. Guenther, R. Hartmann, P. Holl, N. Kimmel, M. Kuehbacher, M. Lang, N. Langhoff, A. Liebel, M. Radtke, U. Reinholz, H. Riesemeier, G. Schaller, F. Schopper, L. Strueder, C. Thamm, and R. Wedell. A new pnCCD-based color X-ray camera for fast spatial and energy-resolved measurements. *NUCLEAR INSTRUMENTS & METHODS IN PHYSICS RESEARCH SECTION A-ACCELERATORS SPECTROMETERS DETECTORS AND ASSOCIATED EQUIPMENT*, 654(1):250–257, OCT 21 2011. ISSN 0168-9002.

[4] O. Scharf, S. Ihle, I. Ordavo, V. Arkadiev, A. Bjeoumikhov, S. Bjeoumikhova, G. Buzanich, R. Gubzhokov, A. Guenther, R. Hartmann, M. Kuehbacher, M. Lang, N. Langhoff, A. Liebel, M. Radtke, U. Reinholz, H. Riesemeier, H. Soltau, L. Strueder, A. F. Thuenemann, and R. Wedell. Compact pnCCD-Based X-ray Camera with High Spatial and Energy Resolution: A Color X-ray Camera. *ANALYTICAL CHEMISTRY*, 83(7):2532–2538, APR 1 2011. ISSN 0003-2700.

[5] Trolltech. Qt graphical library. www.trolltech.com, 2010.

[6] U. Rathmann. Qwt graphical library. qwt.sourceforge.be, 2010.

[7] N. Kimmel and P. Holl. Driver and analysis software for pnCCDs. P.Online, 2009.

[8] N. Kimmel. *Analysis of the Charge Collection Process in Solid State X-ray Detectors*. PhD thesis, UNIVERSITY OF SIEGEN, 2008.

[9] A. Abboud, S. Send, N. Pashniak, W. Leitenberger, S. Ihle, M. Huth, R. Hartmann, L. Strueder, and U. Pietsch. Sub-pixel resolution of a pnCCD for X-ray white beam applications. *JOURNAL OF INSTRUMENTATION*, 8, MAY 2013. ISSN 1748-0221. doi: {10.1088/1748-0221/8/05/P05005}.

[10] K. Yoshita, H. Tsunemi, E. Miyata, K.C. Gendreau, and H.W. Bautz. Improvement of the position resolution of the CCD for X-ray use. *IEEE TRANSACTIONS ON NUCLEAR SCIENCE*, 46(2):100–106, APR 1999. ISSN 0018-9499. doi: {10.1109/23.757195}.

[11] C. Ponchut, J. M. Rigal, J. Clement, E. Papillon, A. Homs, and S. Petitdemange. MAXIPIX, a fast readout photon-counting X-ray area detector for synchrotron applications. *JOURNAL OF INSTRUMENTATION*, 6, JAN 2011. ISSN 1748-0221. doi: {10.1088/1748-0221/6/01/C01069}.

[12] G. Schmaler. *Characterisation of PNCCDs and Analysys of Pixel Defects*. PhD thesis, Technical University München, 2012.

[13] N. Meidinger, R. Andritschke, O. Haelker, R. Hartmann, S. Herrmann, P. Holl, G. Lutz, N. Kimmel, G. Schaller, M. Schnecke, F. Schopper, H. Soltau, and L. Strueder. Next generation of pnCCDs for X-ray spectroscopy and imaging. *NUCLEAR INSTRUMENTS & METHODS IN PHYSICS RESEARCH SECTION A-ACCELERATORS SPECTROMETERS DETECTORS AND ASSOCIATED EQUIPMENT*, 568(1):141–148, NOV 30 2006. ISSN 0168-9002. doi: {10.1016/j.nima.2006.05.286}. 10th European Symposium on Semiconductor Detectors, Wildbad Kreuth, GERMANY, JUN 12-16, 2005.

[14] Matthieu N. Boone. *New Imaging Modalities in High Resolution X-ray Tomography*. PhD thesis, Ghent University, 2013.

[15] B. Vekemans, K. Janssens, L. Vincze, F. Adams, and P. Vanespen. ANALYSIS OF X-RAY-SPECTRA BY ITERATIVE LEAST-

SQUARES (AXIL) - NEW DEVELOPMENTS. *X-RAY SPECTROMETRY*, 23(6):278–285, NOV-DEC 1994. ISSN 0049-8246.

4

2D Elemental Imaging Using the SLcam®

The last couple of years X-ray spectrometry developments have been focussed on achieving higher resolution imaging, down to the nano scale, by improving X-ray focussing optics. A second noticeable trend is the need, from users perspective, to obtain three dimensional elemental information about their sample, made possible by the evolutions made in detector technology, discussed more in detail in Chapter 5 and Chapter 6. Although ultra high resolution or three dimensional data can be a necessity, depending on the sample it is not always needed. There are still a lot of applications that benefit from medium resolution elemental information in two dimensions, while beamlines that focus on medium resolution elemental imaging become more scarce. This chapter focusses on the integration of the SLcam® into the beamlines such as P06 at the Petra III storage ring in Hamburg. The general setup and detector control will be discussed while illustrating its two dimensional imaging capabilities using examples.

4.1 Beamline Integration

4.1.1 Software

As stated in Section 3.2.3, the control software of the SLcam® can be operated remotely using a TCP/IP connection. To incorporate the detector into beamlines, a TANGO server was written to enable the communication between the beamline control software and the SLcam®.

4.1.1.1 TANGO Server

TAco Next Generation Objects (TANGO) is a free and open source object oriented control system based on Common Object Request Broker Architecture (CORBA) and is used to provide network access to hardware for large control systems, such as a synchrotron, at which it was also developed[1]. TANGO is based on the concept of *devices* which are controlled by a *TANGO server* that not only hosts the Mysql database storing all the properties, attributes and commands, but also takes care of the communication with the device. Clients can import devices from the database server to incorporate them into control software. The communication between clients and server and server and devices is done by wrapping the TANGO commands using CORBA since CORBA is multi-platform, network based and language independent. TANGO device servers are mostly written in C++ or Java, while for clients different bindings were written in C, C++, Java, Python, MATLAB, LabVIEW, and IGOR Pro. To improve performance of large control systems (e.g. 100,000 devices) running on a large number of hosts, TANGO supports multi threading and device caching.

The tango server for the SLcam® was written in C++ and can be found on SourceForge[1] or via the official TANGO website[2] under the Acquisition class and is called ISGcamera[3]. To incorporate the SLcam® into the beamline, the TANGO server needs to be installed on one of the beamline computers. The properties and attributes are listed in Appendix C and more detailed information can be found on the XMI wiki[4] since the each beamline requires different settings.

[1] `http://sourceforge.net/p/tango-ds/code/HEAD/tree/DeviceClasses/Acquisition/2D/ISGCamera/`

[2] `http://www.esrf.eu/computing/cs/tango/tango_doc/ds_doc/tango-ds/index.html`

[3] Given the wrong name during code commitment

[4] `http://we08nas1.ugent.be/XMI/index.php?title=SLcam#Beamline_integration`

4.1.2 Hardware

Hardware incorporation is relatively straight forward due to the form factor of the detector, although the position of the detector can vary depending on the aim of the experiment or the properties of the beamline. At the Hard X-ray Micro-Nano Probe P06, Petra III (Hamburg, Germany) the detector was installed in the plane of polarisation (shown in figure 4.1), while at BM26 the detector had to be mounted parallel to the plane of polarisation due to the available beam dimensions. At ID19 the detector was mounted both in or out of the plane of polarisation depending on the sample.

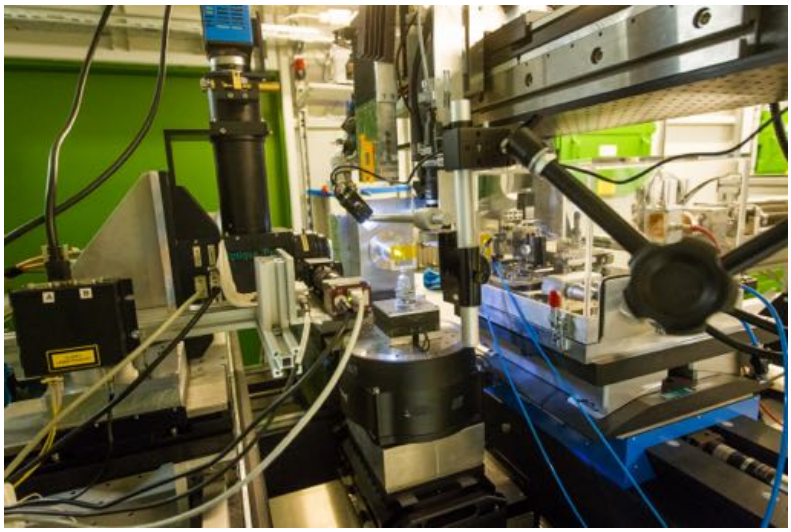

Figure 4.1: Photograph showing the "natural habitat" of the SLcam® at the P06 beamline, Petra III, Hamburg, Germany.

4.2 Application Examples for Elemental Imaging

This section will highlight a few applications showing the potential of the SLcam® for two dimensional elemental imaging.

4.2.1 Cultural heritage: Antwerp Majolica[5]

The majolica technique is characterised by earthenware decorated with various metal oxides which is covered with an opaque glaze (tin glaze),

[5]Manuscript in preparation.

obtaining a multi-coloured object[2]. The goal of our study was to obtain elemental, structural, and molecular information on the used pigments by using a combination of XRF and Raman spectroscopy. The obtained data is then used to build a database to enable the identification and comparison between different majolica samples. The differences between majolica samples are caused by the specific production process, enabling archaeologist to map the different production know-how in production processes. The presented sample is a fragment of Antwerp Majolica, more specifically a fragment of a floor tile which has been embedded into a resin and polished to obtain a smooth surface. This sample consists out of a collection of 30 archaeological fragments originating from four different locations. The samples were orientated in such a way a cross-sectional image could be obtained, showing the different layers of the production process. Due to the very inhomogeneous nature of this type of samples it is important to image large enough areas. Van de Voorde et al. [2], who performed measurements on similar samples using a laboratory instrument (EDAX Eagle III), reported measurement times of $30\,\mathrm{h}$ in total to image an area of $1600 \times 1200\,\mu\mathrm{m}^2$ with a resolution of $20\,\mu\mathrm{m}$. The EDAX Eagle III, is a Rh-anode based instrument that allows measurements under vacuum conditions and uses a polycapillary optic to focus the primary X-ray beam, while the fluorescent X-rays are detected by an liquid nitrogen cooled Si(Li) detector. The obtained elemental distributions are shown in Figure 4.2, clearly visualising the three layers characteristic for the majolica technique. **(A)** The body, is rich in Ca and Fe, with inclusions of Al, Sb, Ti,Si and K, the latter two originating from quartz and feldspar, which were most likely added to alter the properties of the used clay[2]. The second layer **(B)**, white glaze, containing lead as the main element, causing the white colour. Sn is added to obtain the right opacity of the glaze layer, while again Si and K indicate the presence of quartz and feldspar. The last layer **(C)**, the decorating paint layer, which consists in this case of Sb, used in yellow pigments.

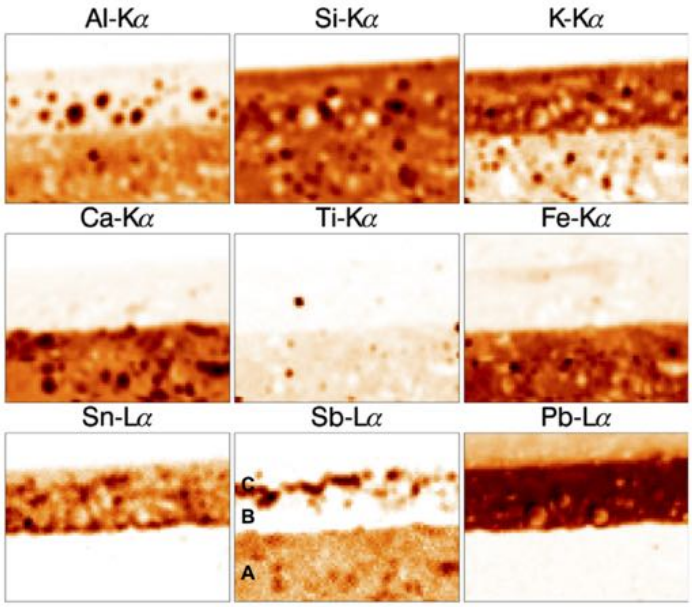

Figure 4.2: 2D elemental maps performed using the EDAX Eagle III scanning μXRF spectrometer, showing the layered structure of majolica, ***(A)*** *the body,* ***(B)*** *primary while glaze layer, and* ***(C)*** *the pigment layer with transparent lead glaze. (Measurement conditions:* $40\,\mathrm{kV}$, $150\,\mu\mathrm{A}$, $20\,\mu\mathrm{m}$ *steps,* $1600 \times 1200\,\mu\mathrm{m}^2$*,vacuum). Adapted from [2].*

The measurements performed with the SLcam® at beamline P06 are summarised in Figure 4.3 and show the 2D imaging capabilities of the SLcam® using a 6:1 polycapillary optic, offering a spatial resolution of about $8\,\mu\mathrm{m}$. The sample surface was orientated at an angle of $5°$ with respect to the primary X-ray beam of $17.0\,\mathrm{keV}$, shown in Figure 4.9. The small rotation applied to the samples was chosen to illuminate the full field of view of the detector while increasing the usage percentage of the full beam, increasing the amount of photons illuminating the field of view but keeping the angle small enough to avoid image distortion.

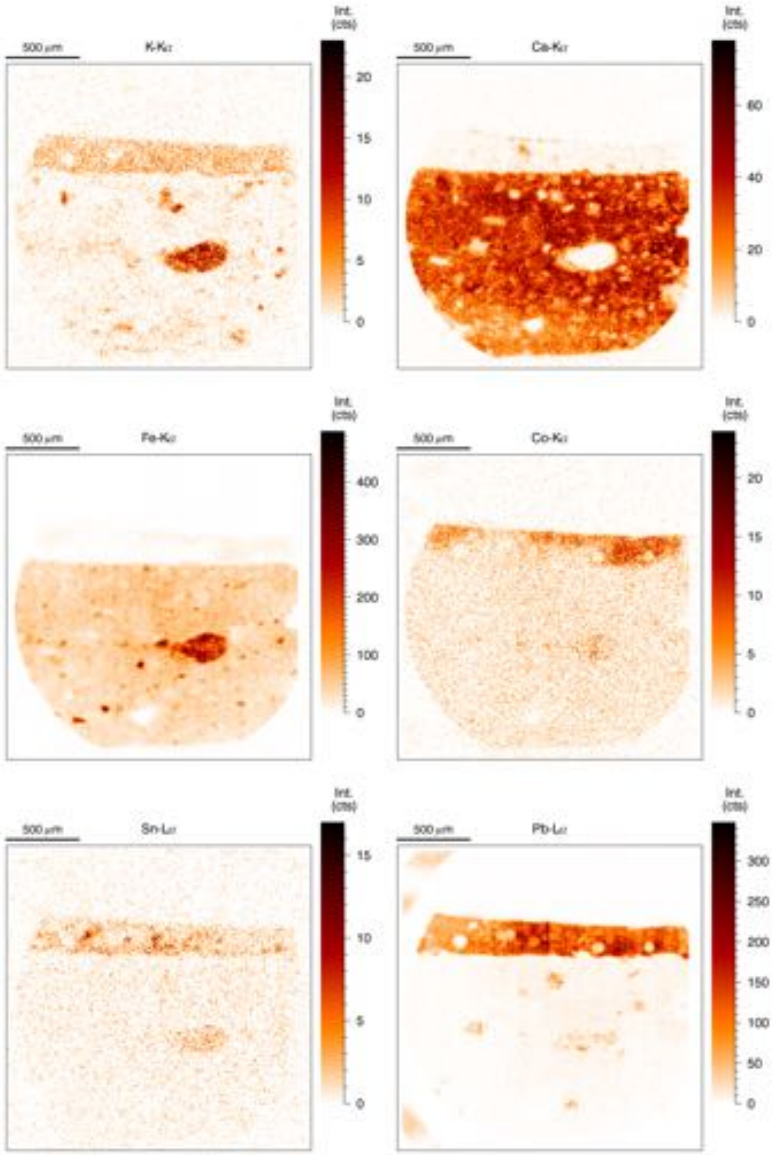

Figure 4.3: 2D elemental images of an Antwerp majolica sample obtained using the SLcam® at beamline P06 illuminated with a broad X-ray beam of 17.0 keV *for 90 minutes.*

Although the sample measured using the laboratory instrument was not identical to the sample that was measured using the SLcam®, one can eas-

ily conclude from comparing Figures 4.2 and 4.3 that the SLcam® offers higher resolution elemental images from a larger field of view in a fraction of the measurement time needed with the laboratory system. However, the sensitivity of the EDAX Eagle III laboratory spectrometer for the lower atomic number elements is higher due to the ability to perform measurements under vacuum conditions. From the elemental distribution images shown in Figure 4.3 confirm the typical structure found in Antwerp majolica consisting out of a body layer (K, Ca, Fe) and a glaze layer (Sn, Pb) and the element Co, present in the glaze layer, points towards the presence of a blue pigment.

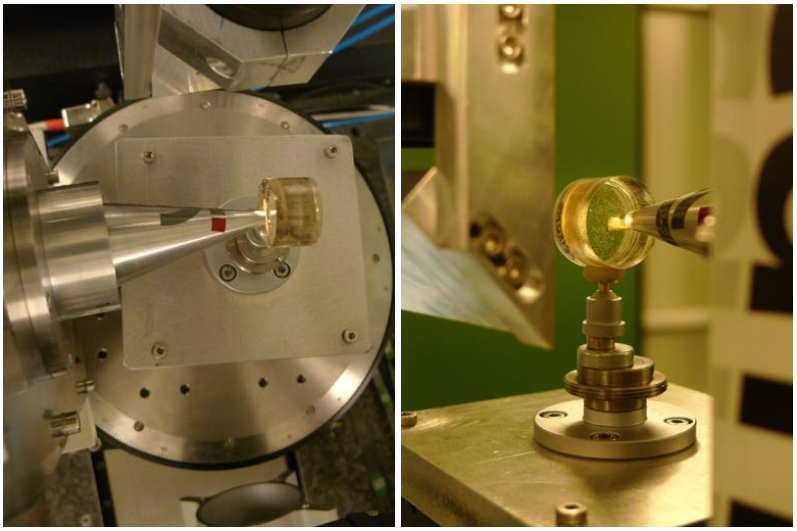

(a) *(b)*

Figure 4.4: The majolica sample embedded in resin mounted in front of the SLcam® equipped with a 6:1 polycapillary optic. The sample surface is rotated 5° *with respect to the primary X-ray beam* ***(A)***

4.2.2 Geological Application

In recent years, geologists have been using XRF more and more due to the general availability of portable or handheld XRF spectrometers[3, 4]. However, these instruments often only offer the ability to perform point measurements since the primary X-ray beam is often in the millimetre range although it is well known that samples are not homogeneous at this scale. If one is only interested in the average composition of a certain sample,

this approach works perfectly fine since the latest models of handheld XRF spectrometers offer a fundamental parameter based quantification scheme which is optimised for that specific spectrometer. The challenges start however when one needs two dimensional elemental information with a high spatial resolution (μm scale). While one of the appealing characteristic of XRF is its non-destructive nature, depending on the sample, the sample preparation often is not.

The geological sample (IM296) that will be discussed is volcanic rock originating from the Methana peninsula (Greece) where it was sampled from a ca. 300 ka old massive lava flow. The major element whole rock composition of IM296 classifies it as a typical arc-type andesite. The sample preparation consisted out of cutting the rock in thin slices using a microtome and depositing the slice on a support glass. The measurement area is shown in Figure 4.6a indicating the scanning area of about $1\,\mathrm{mm}$ in horizontal size.

To be able to characterise the different minerals inside the volcanic rock thin-section, some of which are light elements, a preliminary study was performed using the before mentioned EDAX Eagle III spectrometer due to its capability to perform measurements under vacuum conditions. The elemental distributions are shown in Figure 4.5. Figure 4.6b shows the setup at the P06 beamline, Petra III where the SLcam® measurements were performed. On the right one sees the pierced mirror of the in line beamline microscope, which was moved out during later experiments to increase the achievable vertical beamsize (see Chapter 5), in the middle the volcanic rock thin-section on a glass cover slip mounted in front of the SLcam®, and on the left the tip of the PCO4000 system. The sample was measured for $90\,\mathrm{minutes}$ under the same conditions as described in the previous section. This measurement time is equal to a dwell time of $77\,\mathrm{ms}$ per pixel of a conventional scanning type based XRF spectrometer. When comparing Figures 4.5 and 4.7, one immediately sees the difference in field of view and the obtained resolution. Secondly, the sensitivity towards light elements is greatly improved by the vacuum system and the Rh-L lines of the laboratory system in comparison to the synchrotron setup. However, if one would be more interested in the low Z elements, one could design a vacuum chamber the includes the SLcam®. The SLcam® provides elemental distribution images with lower statistics due to the shorter dwell time per pixel and the efficiency of the used polycapillary optic. The 6:1 polycapillary optic offers in general a lower efficiency due to its tapered form instead of a hyperbolic shape which provides a higher transmission efficiency. A triangular shaped mineral is located at the centre of both figures, consisting of an outer rim, which is clearly visible in the Ca image, consisting of

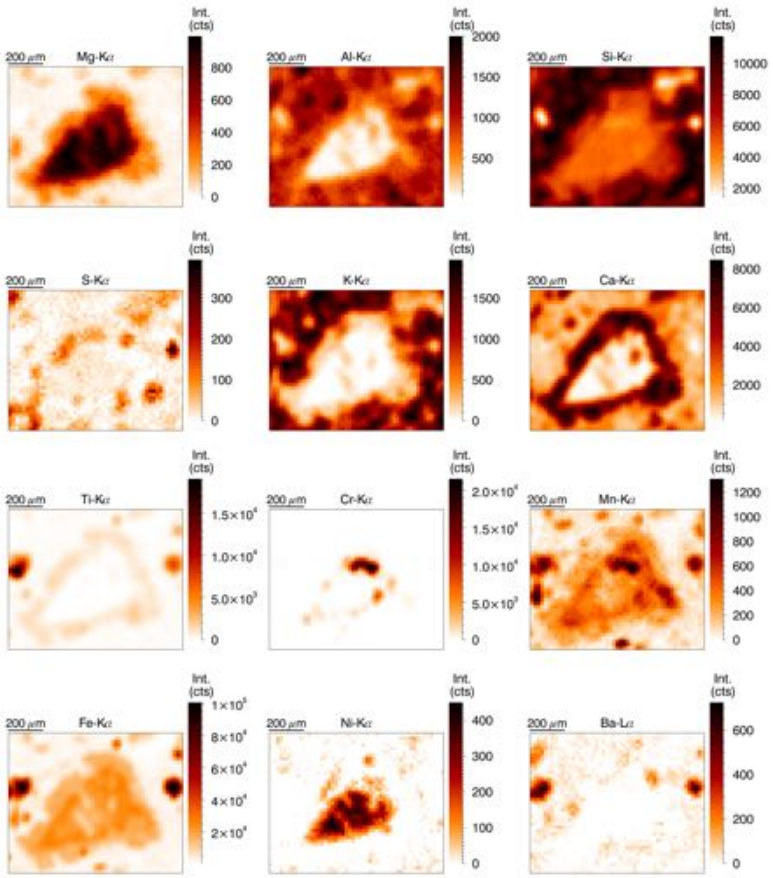

*Figure 4.5: 2D elemental images of a thin slice of volcanic rock thin-section measured under vacuum conditions using the EDAX Eagle III. (*40 kV*,* 180 µA*,* 20 µm *steps,* 10 s LT*, vacuum)*

amphibole. Amphibole is an important group of generally dark coloured inosilicate minerals which mainly consist out of Ca, Mg, Fe, Si, and Al, with traces of Ti, K, Mn. The outer rim encloses a mineral called olivine consisting of $(Fe,Mg)_2SiO_4$ with traces of Ni and Mn. The elemental image of Cr provided the needed information to confirm the presence of Cr-spinel.
Many rounded enclaves (inclusions of another magmatic rock) were observed during fieldwork and interpreted as the result of mixing between a more mafic magma and a crystal-rich more felsic magma. Petrographic observations of amphibole overgrowth rims on Cr-spinel-bearing olivine

(a) *(b)*

Figure 4.6: ***(a)*** *Microscope image of the volcanic rock thin-section indicating in red the measurement area of about* $1\,\mathrm{mm}$ *(H) size.* ***(b)*** *(Middle) volcanic rock thin-section on a glass cover glass mounted in front of the SLcam®, (Right) pierced mirror of the in line beamline microscope, and (Left) the front of the PCO4000 detector at the P06 beamline, Petra III.*

crystals were confirmed by XRF element mapping and represent additional strong evidence for magma mixing.
The petrogenesis of the IM296 lava is therefore interpreted as remobilisation of a cooling, more felsic crystal mush by partial remelting through interaction with a hot more mafic magma. Most of the large plagioclase, amphibole and biotite crystals thereby originate from the felsic crystal mush whereas the olivine crystals are inherited from the mafic replenishment. When such a mafic olivine crystal was enclosed in the felsic crystal mush it was in chemical disequilibrium and therefore reacted with the felsic melt which precipitated an amphibole rim around it[6].

The capability to image large areas with a resolution down to $8\,\mu\mathrm{m}$ in a short amount of time proves to be a real asset for heterogeneous samples like this, leading to a correct determination of the consisting minerals and general composition.

4.2.3 Palaeontological Application

Palaeontological samples can be a real challenging to measure due to several factors. Besides that these samples are often rare and fragile, they most of the time belong to a museum, who are often insisting on the use of non-destructive techniques. Secondly, they can be rather large in size or embedded into a host material, like rock. Due to all these challenges/limitations,

[6]Results to be published

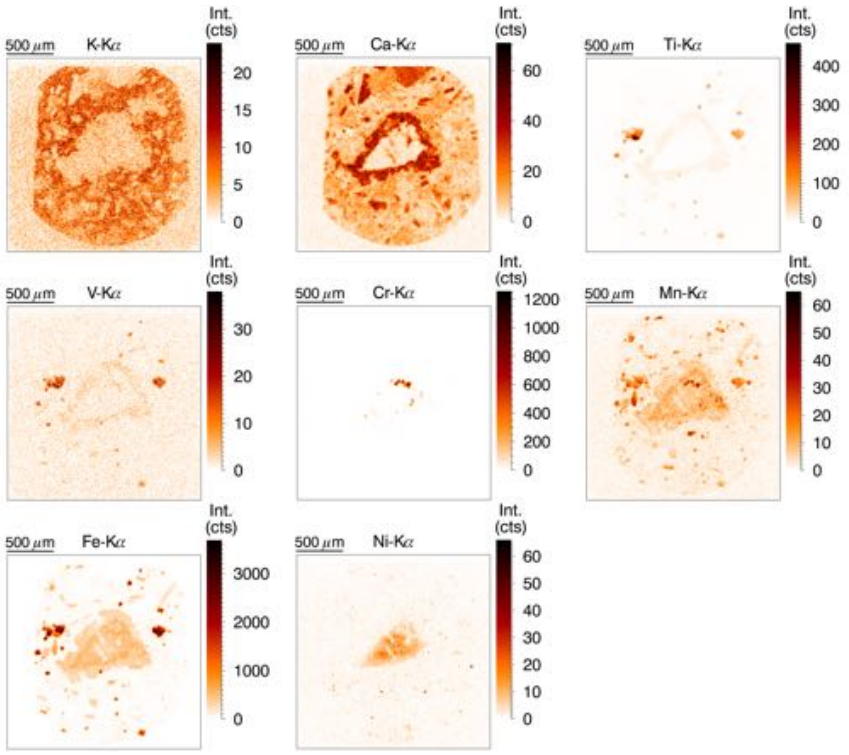

Figure 4.7: 2D elemental images of a thin slice of volcanic rock thin-section measured using the SLcam® with a 6:1 polycapillary lens for $90\,\mathrm{min}$ *at the P06 beamline.*

absorption CT is a technique that is often used since it is a non-destructive technique that allows fast imaging of large volumes.

Even though XRF measurements are to date not able to produce datasets at these scales do to technological limitations or the inherent characteristics of the technique. The technological advances in detector technology, with the SLcam® as an example, brings us one step closer to the possibility to be able to measure larger areas.

One of the measured samples at the ID19 beamline at the European Synchrotron Radiation Facility (ESRF) was a Naraoia fossil, shown in Figure 4.9a, which is a genus of small to average sized marine arthropods that lived during the early Cambrian (541 to $485\,\mathrm{mya}$) till the Silurian (443 to $419\,\mathrm{mya}$) period and can be found in North America, Australia and South Asia[5].

The $145\,\mathrm{m}$ long wiggler based ID19 beamline its main focus of application is absorption CT, therefore providing a large energy range (10 - $250\,\mathrm{keV}$) with a high flux and coherence. During this initial beamtime, the SLcam® was mounted out of the plane of polarisation, as can be seen on Figure 4.8, due to physical constraints which were solved during succeeding beamtimes, allowing mounting in the plane of polarisation thus reducing the background due to multiple Compton scattering. Due to the size of the fossil, the measurement consisted of measuring 11 tiles of a mosaic, illuminating each tile for 5 minutes with a white primary X-ray beam up to about $25\,\mathrm{keV}$ resulting in an average count rate of $435\,\mathrm{kcps}$. The SLcam® was equipped with a 1:1 polycapillary optic, resulting in an effective resolution of $48\,\mu\mathrm{m}^2$. Performing XRF measurements at a CT beamline offers

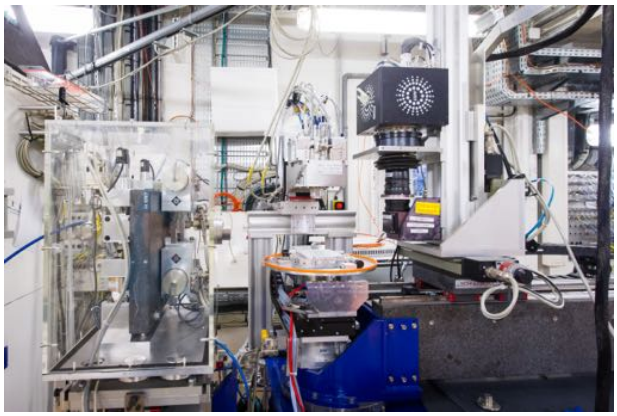

Figure 4.8: Experimental setup of the SLcam® at ID19, ESRF. The primary white X-ray beam comes from the left, passes through a slit system (Left), SLcam® in its measurement position perpendicular to the plane of polarisation (Middle), and FreLon detector (Right).

a couple of challenges, such as the lack of a beam intensity monitor to be able to normalise the measurement to the decaying intensity of the primary X-ray beam caused by the Touschek effect in the storage ring. The decay in intensity is substantial since the storage ring at the ESRF is up until now not operated in top-up mode. Figure 4.9b shows the iron distribution of the naraoia fossil which was not normalised for difference is beam intensity and distance to the detector to show the mosaic measurement strategy and the importance a normalisation step during data processing. The current strategy to keep track of the decay in beam intensity, is taking an image before and after the measurement with a photon counting detector when the

sample is moved out of the X-ray beam. Therefore, providing the average intensity during the measurement except for data that was acquired during a refill of the storage. In this particular case, the acquisition time before and after the refill is taken into account. This examples showed the fast

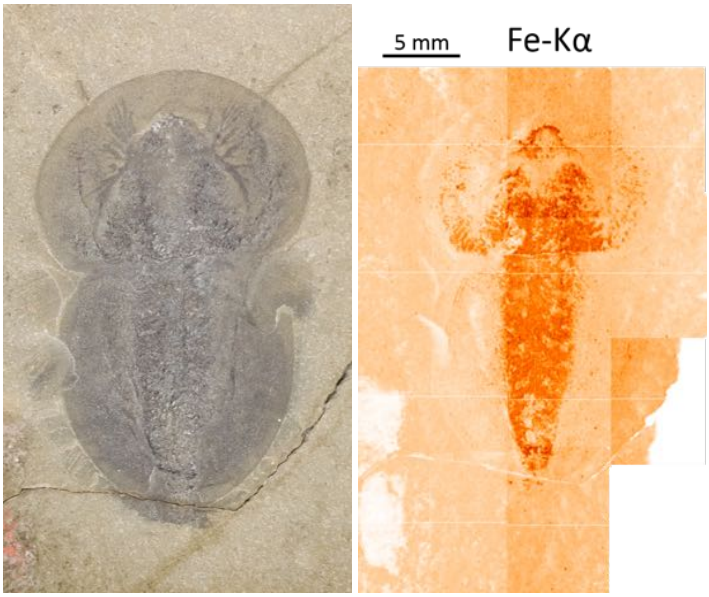

(a) *(b)*

Figure 4.9: ***(a)*** *Photograph of the measured Naraoia* ***(b)*** *non normalised Fe distribution image, showing the mosaic measuring pattern and the vast sample size that can be measured in a short period of time (*$1\,\mathrm{h}$*).*

imaging capabilities of the SLcam® by scanning an area of about 25 by $55\,\mathrm{mm}^2$ with a resolution of $48\,\mu\mathrm{m}^2$ in 1 hour.

4.2.4 2D XANES Imaging

The speed gain towards 2D elemental imaging by using an energy dispersive pixel detector, like the SLcam®, has made it possible to perform 2D X-ray Absorption Near Edge Structure (XANES) imaging in emission mode[6]. In the past XANES imaging was almost never performed due to the time consuming nature by the introduction of third scanning axis, the energy. XANES is a well-known technique to obtain chemical state and local structure information in a non-destructive way. While most laboratory instruments are able to perform 2D scans, they do not offer the possibility

to scan the source energy due to the lack of a monochromating crystal. Therefore, XANES experiments are most often performed at a synchrotron radiation facility where available experimental time is scarce. Tack et al. [6] have successfully shown the possibility the use the SLcam® as a detector during a fluorescence based XANES measurement performed at the Dutch Belgian Beamline (DUBBLE) at the ESRF. During this proof of principle experiment, a custom made sample consisting of iron standards (Fe^0/Fe_2O_3) was used, to provide proof of principle on the determination of the chemical state distribution of Fe using the SLcam®. The total experiment took $7.6\,\mathrm{h}$ to scan 51 energies with a field of $13^2\,\mathrm{mm}^2$ obtaining a resolution of $48^2\,\mu\mathrm{m}^2$. In comparison, a traditional fluorescence mode XANES measurement takes 2 to 20 minutes per scanning point, meaning that a similar measurement as performed using the SLcam® would take between 96.8 and 968 days, which is not feasible. However, with the introduction of new pulse processing units and detectors, like the Maia detector, and diffraction limited storage rings, 2D XANES imaging in emission mode will become a standard technique[7].

4.2.5 Conclusion and Outlook

This chapter presented an overview of different applications in different research field of the SLcam® and the speed increase in comparison to point-by-point based spectrometers. The SLcam® belongs to the category of first generation energy dispersive pixel detector. Although these detectors form a leap forward they are not without faults. Certain aspects as there are, the event analysis, the efficiency of optics of this size, still need to be optimised or improved upon. The sensitivity for the lighter elements can be improved upon by incorporating the detector into a vacuum chamber or purging the sample environment with He. Pixel based detectors will always have their resolution limited by the pixel size and the optics mounted on them, making them currently limited to a resolution of several micron while state-of-the-art microbeam end stations already offer resolutions of several $100\,\mathrm{nm}$. The SLcam® is definitely not always the best choice of detector system for each application, or should be the only detector system used during an experiment. The right choice of detector or detector combination will largely depend on the sample. For example, an experiment (not shown, submitted) at the P06 beamline the SLcam® was used to make large overview maps with $8^2\,\mu\mathrm{m}^2$ resolution with a field of view of $1.5^2\,\mathrm{mm}^2$ which were then used to select a ROI for a high resolution scan ($0.5\,\mu\mathrm{m}$) with a focussed beam and a Vortex SDD detector. The combination of both measurement strategies was not only a big time saver but also gave us elemental distribu-

tion images of a large area with a lower resolution while also obtaining high resolution images of a ROI selected using the elemental distribution images obtained using the SLcam®. The total opposite approach of the Maia detector allows for high resolution images of large areas in short periods of time but can be limited by the type and rigidity of the sample or the ability of the motor stages.

4.2.6 Acknowledgements

The author would like to thank Lien Van de Voorde for the collaboration regarding the Antwerp majolica samples, Dr. Ingrid Smet for the geological application, Dr. Paul Tafforeau concerning the Palaeontological application, and Pieter Tack for the proof of principal experiment concerning 2D XANES imaging in emission mode.

References

[1] J-M. Chaize, A. Götz, W-D Klotz, J. Meyer, M. Perez, and E. Taurel. TANGO - an object oriented control system based on CORBA. *ICALEPCS*, 1999.

[2] L. Van de Voorde, M. Vandevijvere, B. Vekemans, J. Van Pevenage, J. Caen, P. Vandenabeele, P. Van Espen, and L. Vincze. Study of a unique 16th century antwerp majolica floor in the rameyenhof castle's chapel by means of x-ray fluorescence and portable raman analytical instrumentation. *Spectrochimica Acta Part B: Atomic Spectroscopy*, 102(0):28 – 35, 2014. ISSN 0584-8547. doi: http://dx.doi.org/10.1016/j.sab.2014.10.007.

[3] M. West, A. T. Ellis, P. J. Potts, C. Streli, C. Vanhoof, and P. Wobrauschek. 2014 Atomic Spectrometry Update - a review of advances in X-ray fluorescence spectrometry. *JOURNAL OF ANALYTICAL ATOMIC SPECTROMETRY*, 29(9):1516–1563, SEP 2014. ISSN 0267-9477. doi: {10.1039/c4ja90038c}.

[4] G. L. Bosco. Development and application of portable, hand-held X-ray fluorescence spectrometers. *TRAC-TRENDS IN ANALYTICAL CHEMISTRY*, 45:121–134, APR 2013. ISSN 0165-9936.

[5] W.T. Zhang. Preliminary notes on the occurrence of the unusual trilobite naraoia in asia. *Acta Palaeontologica Sinica*, 24(6):591–595, 1985. URL `http://biostor.org/reference/47432`.

[6] P. Tack, J. Garrevoet, S. Bauters, B. Vekemans, B. Laforce, E. Van Ranst, D. Banerjee, A. Longo, W. Bras, and L. Vincze. Full-Field Fluorescence Mode Micro-XANES Imaging Using a Unique Energy Dispersive CCD Detector. *Analytical Chemistry*, 86(17):8791–8797, SEP 2 2014. ISSN 0003-2700. doi: {10.1021/ac502016b}.

[7] M.D. de Jonge, C.G. Ryan, and C.J. Jacobsen. X-ray nanoprobes and diffraction-limited storage rings: opportunities and challenges of fluorescence tomography of biological specimens. *JOURNAL OF SYNCHROTRON RADIATION*, 21(5):1031–1047, SEP 2014. ISSN 0909-0495. doi: {10.1107/S160057751401621X}.

5

A New Methodology Towards 3D Micro-XRF Imaging

As published:
J. Garrevoet, B. Vekemans, P. Tack, B. De Samber, S. Schmitz, F. E. Brenker, G. Falkenberg, and L. Vincze. Methodology toward 3d micro x-ray fluorescence imaging using an energy dispersive charge-coupled device detector. *Analytical Chemistry*, 86(23):11826–11832, 2014. doi: 10.1021/ac503410s

Three-dimensional micro X-ray fluorescence (μXRF) measurements are often needed to study the distribution of elements within the investigated objects but are not frequently used due to the time consuming nature of the required three-dimensional scanning in case of established techniques such as confocal XRF and XRF tomography[2]. Despite these limitations these methodologies are used in a variety of research fields, including Earth and environmental/life science, material science as well as cultural heritage related applications[3, 4]. The latest developments in energy dispersive (ED) X-ray detector technology opens new avenues for the determination of 3D distributions of elements within the investigated sample on the microscopic scale. By the introduction of a novel 2D energy dispersive detector (SLcam® [5, 6]), one can directly obtain 2D elemental distribution images of the sample in question when it is illuminated by a broad X-ray beam. This silicon CCD based detector consists of a chip measuring 12.7 by $12.7\,\mathrm{mm}^2$ with 264 by 264 energy dispersive pixels of $48\,\mu\mathrm{m}$ which delivers images with a spatial resolution down to $8\,\mu\mathrm{m}$ depending on the detector optics used. The proposed 3D elemental imaging methodology, which was independently developed from Radtke et al. [7], combines this novel 2D ED detector with a linearly focused X-ray beam (sheet beam) to obtain cross-sectional elemental distribution images from various depths of the sample when it is scanned perpendicularly through the sheet beam.

Combining the detected elemental images from the analysed cross-sections provides a three dimensional elemental view of the sample without any need of a tomographic reconstruction algorithm which can cause artefacts. This novel approach is demonstrated by 3D-XRF measurements performed at the Hard X-ray Micro/Nano-Probe beamline P06 (Petra III, DESY, Hamburg, Germany) on natural deep Earth diamonds.

5.1 Experimental Setup

The μXRF measurements were performed at the Microprobe endstation of beamline P06 at the $6\,\mathrm{GeV}$ electron or positron storage ring PETRA III at DESY (Hamburg, Germany) operated with a current of $100\,\mathrm{mA}$ in top-up mode. This undulator source based beamline is dedicated to chemical and structural imaging applications on the micro- and nanoscopic scale based on X-ray fluorescence (XRF), X-ray absorption spectroscopy (XAS) and X-ray diffraction (XRD) techniques. The beamline is equipped with a Si(111)/Si(311) double crystal monochromator with an energy resolution of $1.4 \cdot 10^{-4}\ \Delta\mathrm{E}/\mathrm{E}$ and can cover an energy range from 2.4 to $50\,\mathrm{keV}$ using the Si(111) monochromator. Furthermore it is equipped with a multilayer monochromator with an energy bandwidth of $2 \cdot 10^{-2}\ \Delta\mathrm{E}/\mathrm{E}$ cover-

ing an incident energy range of 10 to 100 keV, delivering a 30 times higher flux in comparison to the Si(111) monochromator. At the P06 microprobe the focussing of the monochromatised primary X-ray beam is performed by a Kirkpatrick-Baez (KB) mirror system (JTEC, Japan) with an energy range from 5 to 21 keV, a working distance of 200 mm and a divergence of 1 mrad.

During the 3D μXRF experiments, the vertically focusing mirror of the KB-system was lowered, removing it from the beam path. This way the beam was only focused in the horizontal dimension by the second mirror, producing a vertically oriented 'sheet-beam'. The horizontal beam size was determined by a knife-edge scan using a 50 μm gold wire, while the vertical beam size was determined using a PCO 4000 high resolution CCD X-ray camera which is positioned along the primary beam downstream of the sample position. The obtained sheet beam during the first experiment measured 6.8 μm horizontally by 1.37 mm vertically and 5.0 μm (H) by 1.8 mm (V) during the second experiment.

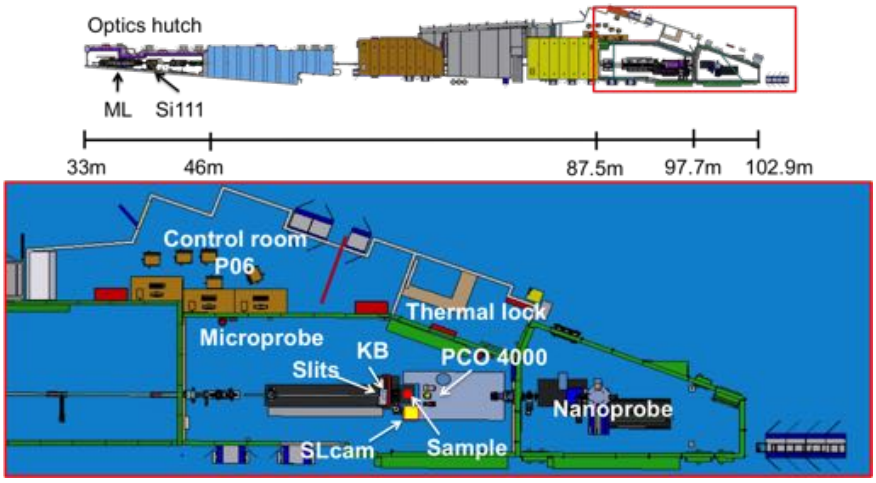

Figure 5.1: Showing a top view of the P06 Hard X-ray Micro/Nano-Probe, indication the locations of the monochromator, slit and KB system, SLcam®, PCO 4000 and the sample location.

The 2D energy dispersive detector (SLcam®) consists of a back-illuminated pnCCD chip of 264 by 264 pixels with an area of 48 by 48 μm^2 each. The active Si layer has a thickness of 450 μm. Because of this relatively thick active Si-layer, the quantum efficiency is above 95 % in the range of 3 to 10 keV and above 30 % at 20 keV [5]. An average energy resolution of

$156\,\mathrm{eV}$ at the Mn-Kα line ($5.898\,\mathrm{keV}$) is reached and thus comparable with current silicon drift detectors (SDD) when used with short peaking times. The detector can be equipped with a variety of optics ranging from pinholes to polycapillary lenses allowing the user to adapt the field of view and obtained spatial resolution to their experimental needs, reaching a maximal spatial resolution of $8\,\mu\mathrm{m}$ with a field of view of nearly 2 by $2\,\mathrm{mm}^2$. In case of these experiments, the SLcam® was mounted on a XYZ-stage and positioned at 90° with respect to the primary X-ray beam to obtain distortion free imaging capability with maximal achievable spatial resolution, and to improve the fluorescence-to-scatter background ratio due to the polarised nature of synchrotron radiation.

The cross-sectional elemental images are obtained by scanning the sample through the vertical sheet beam as depicted in Figure 5.2. Figure 5.3 shows the typical setup used.

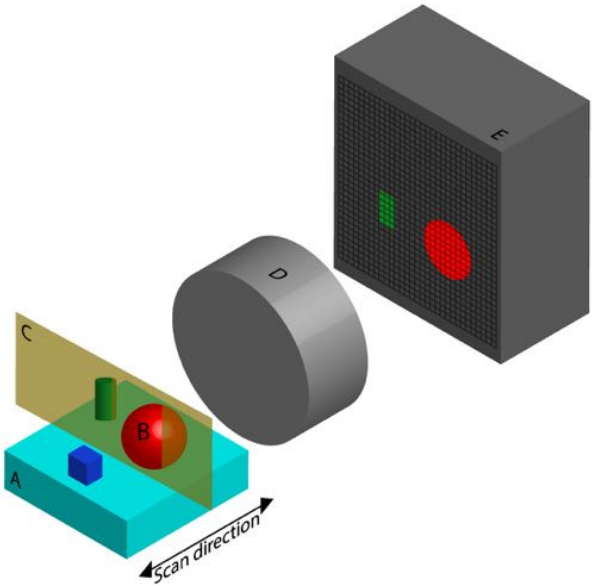

Figure 5.2: Cartoon depicting the measurement methodology. ***(A)*** *sample holder,* ***(B)*** *sample objects (red, green, blue),* ***(C)*** *sheet beam,* ***(D)*** *X-ray optic, and* ***(E)*** *the SLcam®.*

The raw XRF spectra are converted into net intensities using the non-linear least-squares fitting software package AXIL/microxrf2[8]. These software packages are designed for accurate background corrections, deconvolution of energy-dispersive XRF spectra, elimination of peak overlap

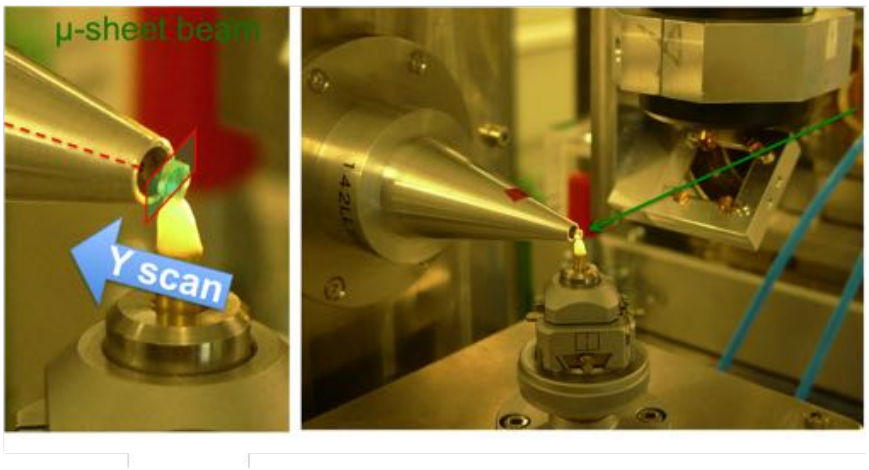

Figure 5.3: Experimental arrangement used for the 3D-XRF measurements (overview image: right; detail image: left), showing the natural deep Earth diamond sample in the centre of the images, mounted on a brass pin using wax. The polished side is oriented towards the 6:1 polycapillary optic. The vertical X-ray sheet beam (indicated by green overlay) penetrates the sample parallel with the polished surface of the diamond, oriented towards the detector optic of the detector. The generated XRF/scatter signal is detected by the SLcam®, resulting in a stack of elemental images (i.e. the desired 3D elemental information) derived from a linear Y-scan of the sample.

and other spectral artefacts. Self-absorption effects were not taken into account with the evaluation of these datasets, however for a maximum probing depth of $150\,\mu\mathrm{m}$ we expect an intensity reduction due to sample absorption, for Fe-Kα, less than $25\,\%$.

The described results were obtained during 2 experiments conducted at the P06 beamline at the Petra III storage ring, DESY. The excitation energy for the 3D µXRF measurements was fixed at $17.0\,\mathrm{keV}$ using the double crystal Si(111) monochromator for the first experiment and at $17.4\,\mathrm{keV}$ using the multilayer monochromator during the second.

5.2 Results and Discussion

5.2.1 Analytical Characteristics

In order to determine the analytical characteristics of the described experimental setup the ATHO-G (MPI-DING) rhyolitic glass standard[9, 10]

was illuminated using a quasi-monochromatic sheet beam of $5\,\mu\mathrm{m}$ (H) by $1.8\,\mathrm{mm}$ (V) in size at an energy of $17.4\,\mathrm{keV}$, obtained by multilayer based monochromatisation in conjunction with one-dimensional (horizontal) focusing by a single mirror. A 6:1 polycapillary lens was mounted on the SLcam® to obtain a high spatial resolution. The detected sum spectrum (integrated over the entire chip area) corresponding to an acquisition real-time of $600\,\mathrm{s}$ is shown in Figure 5.4a, illustrating the excellent peak-to-background ratios achievable by the SLcam®, even at count rates reaching $450\,\mathrm{kcps}$. This measurement results in minimum detection limits (MDL), calculated using Formula 5.1, in the ppm range for transition metals when larger pixels areas are taken into account (Figure 5.4b). MDLs based on single pixels are in the 10 to $100\,\mathrm{ppm}$ range.

$$MDL_i = \frac{3 \cdot \sqrt{B_i}}{I_i} \cdot c_i \tag{5.1}$$

With B_i the background intensity of element i, I_i the net line intensity of element I and c_i the certified concentration of element i in the standard.

The achievable elemental imaging capabilities at low concentration levels represent great benefits for non-destructive studies of minor and trace-element distributions in a variety of disciplines.

The spatial resolution of the first dimension is completely determined by the characteristics and tuning of the used focusing optics of the primary x-ray beam. The obtained spatial resolution in the two other dimensions are determined by the detector and the optics used and therefore currently limited to the micron scale while computed tomography based techniques are able to obtain resolutions below one micron. However, computed tomographic techniques and their obtained resolution are greatly influenced by motor accuracy and repeatability.

Self-absorption effects have a different impact on CT based XRF than on the presented methodology. While artefacts are introduced due to the tomographic reconstruction algorithm, self-absorption can only influence the information depth when this new methodology is used. This fundamental difference makes quantification of a dataset obtained using this full field method much more straight forward than for CT XRF.

5.2.2 Inclusions in natural deep Earth diamonds

Geological setting During the growth of a diamond, fluids, minerals and rocks can be trapped within and are then shielded during the transport towards the Earths surface preserving their original composition. Ultra-deep diamonds from the Transitions zone and the lower mantle regions of

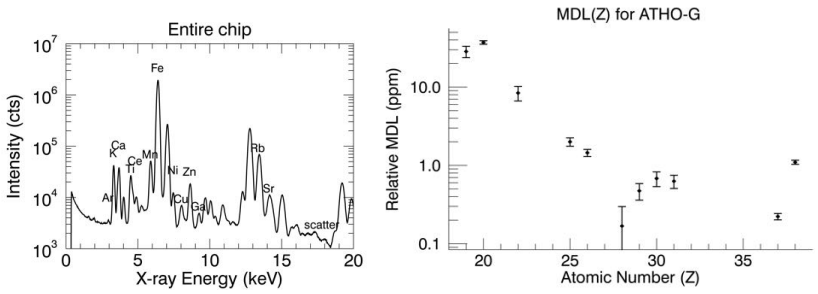

Figure 5.4: (a) XRF sum spectrum obtained by integrating the individual spectra recorded by each pixel of the chip, corresponding to the ATHO-G rhyolitic glass standard when illuminated for $600\,\mathrm{s}$ *using the vertical sheet beam. (b) The minimum detection limits calculated from the spectrum shown on the left are plotted in the figure.*

the deep Earth are provided by only a few sources like the Juina area in Brazil[2, 11–21]. They provide the only direct source of information about the chemical and physical conditions to at least the upper part of the lower mantle. Diamonds presented in this study come from the Juina and Rondonia regions (Brazil) which are located in the Northwest Mato Grosso in Brazil, South America.

Sample description We report here the results of the analyses corresponding to two diamonds investigated by the novel 3D SR-XRF elemental imaging technique. The first sample, diamond P11 comes from the Machado River (Rondonia) and RS55 from the Rio Soriso (Juina Area) alluvial diamond deposit. P11 is a diamond that was already polished into a parallel plate and had already undergone major investigations using various techniques (e.g. cathodoluminescence (CL), electron microscopy (EM), Raman, Fourrier transform infrared spectroscopy (FTIR), SR-XANES/XRF, SR-imaging using plate detector[1]). The diamond plate has a size of $\sim 3\,\mathrm{mm}$ and is transparent and colourless. It shows a large ($\sim 200\,\mu\mathrm{m}$) inclusion cloud in its growth centre which is $300 - 400\,\mu\mathrm{m}$ from both polished surfaces of the diamond plate (Figure 5.5a). This makes the collection of XRF radiation easier due to lower absorption and diminishes scattering caused by the diamond body. The complex inclusion cloud with an irregular shape and size of $\sim 200 - 250\,\mu\mathrm{m}$ is located right in the growth centre of the

[1] Unpublished data

diamond and could only be formed by crystallising from a melt or fluid trapped during the formation of the diamond. Furthermore, inclusions of ferripericlase and (MgFe)SiO_3 were identified by EM. Several other inclusions visible throughout the diamond P11 were identified to be of lower mantle ($> 660\,\mathrm{km}$ deep) origin based on the presence of ferropericlase coexisting with inclusions of (MgFe)SiO_3 enstatite, which was discovered using Raman spectroscopy as well as μXANES. (MgFe)SiO_3 diamond inclusions with pyroxene structure in association with ferropericlase are believed to be former (MgFe)SiO_3-perovskite as this association is only stable in the lower mantle (e.g. [22–24]).

The second diamond, RS55, comes from the Rio Soriso alluvial diamond deposit (Juina). The original diamond is colourless, transparent and was cut into a $\sim 1\,\mathrm{mm}$ thick diamond slice using a laser. This slice contains one large inclusion ($\sim 200\,\mu\mathrm{m}$, see Figure 5.5b) and a countless number of smaller micro-inclusions and nano-inclusions ($30 - 100\,\mathrm{nm}$). The main inclusion did not exhibit a detectable Raman spectrum to identify the mineral phases. The observed cracks surrounding the main inclusion did not show any connection to the surface of the diamond proving that loss of fluids did not occur.

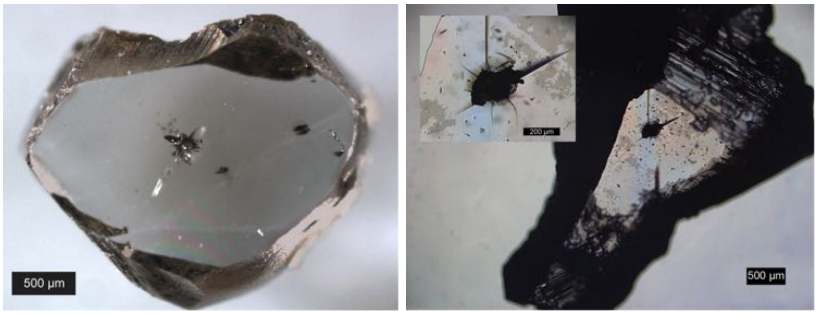

(a) *(b)*

Figure 5.5: ***a:*** *Diamond P11 showing the prominent central inclusion cloud with an irregular structure, consisting of a cluster of apparent different mineral/fluid phases.* ***b:*** *Inclusion in diamond RS55_SL2 showing several cracks around the inclusion and a large number of micro- and nano-inclusions in the diamond matrix. Inset shows main inclusion surrounded by cracks and a few smaller micron sized inclusions.*

Example 1: The experiment involving diamond P11 was conducted using a $17.0\,\mathrm{keV}$ primary X-ray sheet beam of $6.8\,\mu\mathrm{m}$ (H) by $1.8\,\mathrm{mm}$ (V) using

the Si(111) monochromator combined with the horizontally focussing mirror of the KB system. The recorded micro-XRF image-stack consists of 41 slices with $5\,\mu\mathrm{m}$ steps in between each slice.

Each slice was recorded using an acquisition (real) time of 30 minutes, which translates to a total measurement time of $\sim 20.5\,\mathrm{h}$. The obtained 2,857,536 ($41\times264\times264$) XRF spectra, corresponding to the analysed voxels, were deconvoluted using AXIL[8] and processed using several IDL (Exelis Visual Information Solutions, Boulder, Colorado) routines to combine the evaluated spectra into 3D elemental distribution images. Since there are no tomographic reconstruction algorithms needed to obtain the 3D elemental distribution images, no artefacts are introduced during the processing of the data. This is a huge benefit of this proposed technique over XRF tomography where the accuracy and quality of the 3D reconstruction depends crucially on the (statistical) quality of the obtained spectra. In order to identify chemically similar phases within the detected inclusion clouds, voxels corresponding to similar composition were grouped into clusters using K-means clustering[25]. The K-means clustering was performed using IDL code while the number of clusters was determined by an iterative process by comparing how well the different clusters could describe and separate the mineral phase from the diamond matrix. In the examples below only the clusters which contain the natural inclusions are shown.

Figure 5.6 (left) shows the 2D distribution of iron in slice 24 ($\sim 100\,\mu\mathrm{m}$ from the polished surface). Only the centre of the image appears to contain an iron rich inclusion, while the surrounding matrix represents the diamond ($264 \times 264\,\mathrm{pixels}$ or $2.1 \times 2.1\,\mathrm{mm}$). In the right panel of Fig.5., a magnified image of the central area is shown, consisting of $51 \times 51\,\mathrm{pixels}$ ($410 \times 410\,\mu\mathrm{m}$) showing the Fe distribution with several smaller hotspots located around the central inclusion. The ability to investigate a relatively large volume of a diamond in 3D in a single experiment using a simple linear scan has enabled us to analyse more diamond inclusions and to obtain larger 3D-XRF data sets than ever before. Previous confocal XRF and confocal XANES measurements on inclusions in deep Earth diamonds have proven to be challenging since the μm sized inclusions are difficult to locate in 3D within the diamond using a confocal setup with a confocal volume of only a few μm in size and therefore losing precious measurement time[4].

The acquired data for all detected elements was combined into 3 clusters of different average intensities using k-means clustering and a 3D volume was generated using these clusters. The obtained 3D cluster-images and the corresponding sum spectra of the clusters are shown in Figure 5.7. The 3D representation shows three clusters (red, green, blue), all are dominated by Fe whereas only the blue one contains some amount of Ni. The highest

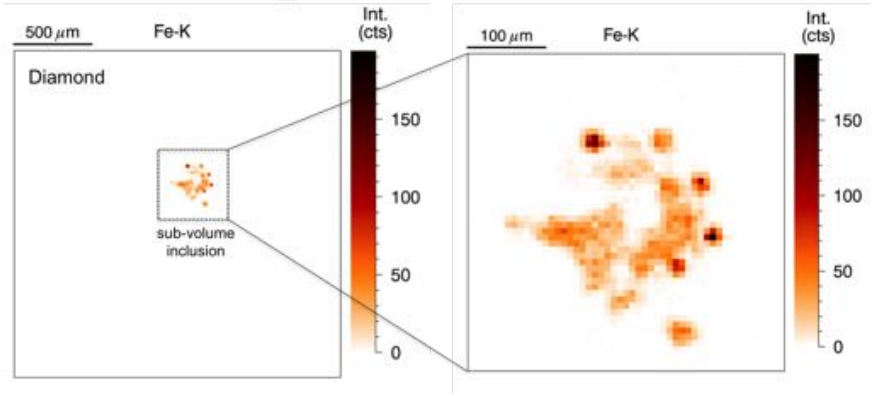

Figure 5.6: (Left) 2D elemental image of one slice of diamond P11 showing the Fe distribution for the main inclusion and some part of the surrounding diamond with no elemental contributions. (Right) A subvolume showing only the Fe distribution of the main inclusion.

Fe voxel intensities are coloured blue, lower intensities in green and even lower intensities in red. The cluster analysis was mainly influenced by the Fe and Ni fluorescence signal (Fe-K average voxel intensities for the different clusters: Clr1 14, Clr2 40, Clr3 129; Ni-K average voxel intensities for the different clusters Clr1 0, Clr2 1, Clr3 15). Noticeable is the fact that the outer rim of the inclusion is mostly coloured red, indicating a low Fe content in those regions (corresponding to the 2D Fe map shown in Figure 5.6). The centre of the inclusion shows a whole spectrum of colours, again demonstrating the complexity of the inclusion cloud.

It is clearly visible that there are several smaller, isolated hotspots located around the main inclusion (probably Ferropericlase, identified earlier by μ-XANES). The smaller Fe-enhanced spots located around the main inclusion correspond well with the optical image shown in Figure 5.5. The main inclusion shows lower Fe signal compared to the small hotspots and is supposed to be composed of a variety of different mineral inclusions which is known from Raman data (unpublished).

Example 2: RS55_SL2 is a diamond cut using a laser beam to a $\sim 1\,\mathrm{mm}$ thick slice. It is transparent and contains a large number of micro- and nano-inclusions and one larger inclusion ($\sim 200\,\mu\mathrm{m}$) , which was measured using the described full field 3D XRF methodology. This diamond was analysed during a second experiment at the P06 beamline using a $17.4\,\mathrm{keV}$

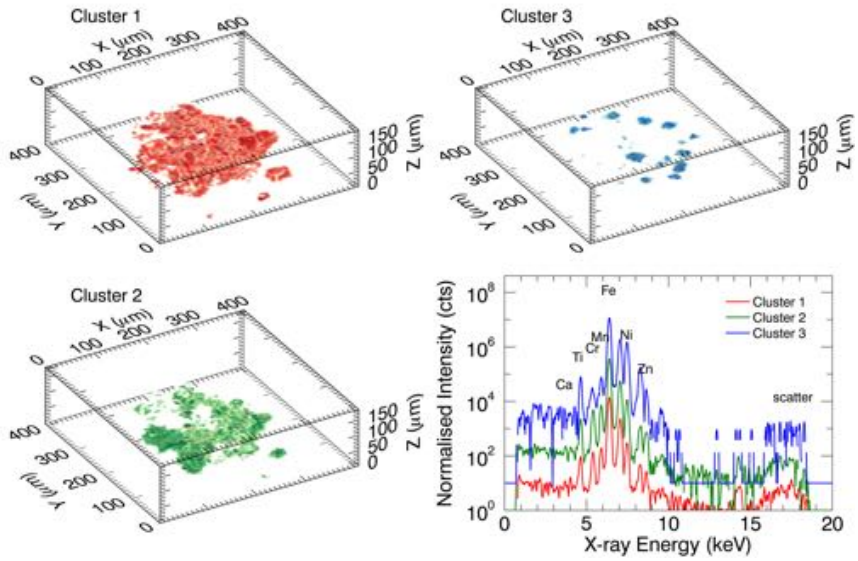

Figure 5.7: (Top and Left Bottom) 3D reconstruction of the main inclusion of diamond P11 using three clusters (esp. Fe is part of each cluster). (Right Bottom) Corresponding sum spectra of the three clusters. The highest Fe intensities are coloured blue, lower intensities in green and even lower intensities in red.

primary sheet beam of $5.0\,\mu\mathrm{m}$ (H) by $1.8\,\mathrm{mm}$ (V) in size, with a much higher flux due to the use of a multilayer monochromator which resulted in shorter measurement times per slice.

The inset in Figure 5.5b corresponds to the area that was measured, thus including the surrounding area around the larger inclusion, which is surrounded by several cracks. None of these cracks were in contact with the (former) diamond surface ensuring that there was no interaction with the surrounding environment. Here, 34 slices were measured with steps of $5\,\mu\mathrm{m}$ apart. Each slice was measured using an acquisition (real) time of $10\,\mathrm{min}$ which resulted in a total measurement time of $\sim 7\,\mathrm{h}$. The left of Figure 5.8 shows one of the slices obtained during the measurements on RS55_SL2 illustrating the employed 3D XRF methodology. The spectra were analysed and processed in the same way as was described for example 1.

The 3D ($0.48\times0.48\times0.12\,\mathrm{mm}^3$) reconstruction of the inclusion consists of 86400 voxels of $8\times8\times5\,\mu\mathrm{m}^3$ and represents a sub-volume of the total image (Figure 5.9). This measurement also provides Fe with the highest number of counts in each cluster. Next to the iron signal only lower

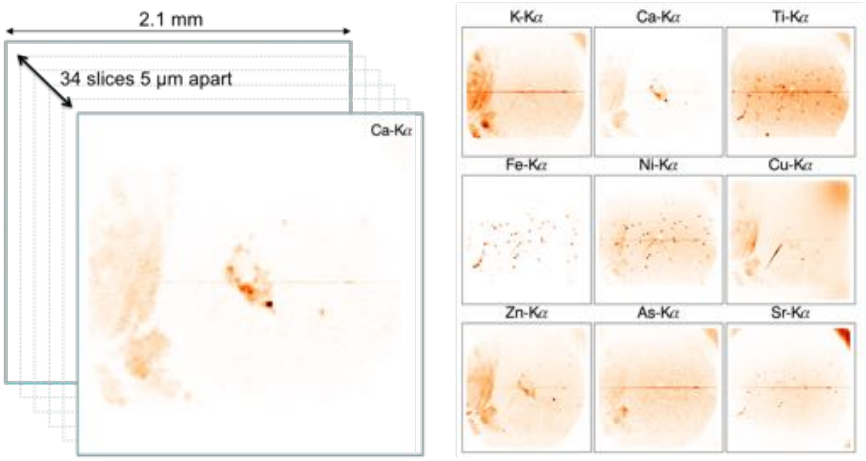

Figure 5.8: 2D elemental images of inclusions in diamond RS55_SL2. (Left) Showing the principle of data collection, performing various measurements of slices of the diamond at different depths (here, each slice was $5\,\mu\mathrm{m}$ *apart). 34 slices were collected in total, each slice was measured for* $10\,\mathrm{min}$ *at* $17.5\,\mathrm{keV}$ *(Right) Different elemental distribution images obtained at the same depth inside diamond RS55_SL2 are shown on the right.*

count rates of other elements like Mn or Ca are visible. Moreover, in the sum spectrum higher peaks of K, Ca, Cu, Zn and Rb are visible and lower count rates of Ti, Cr, Mn, Ni and Sr.

5.2.3 Cross-sectional imaging on biological samples

As stated in the title of this chapter, the proposed methodology provides a novel way to obtain 3D information on a sample, but can also be used to just obtain cross-sectional images.

5.2.3.1 Experimental description

A study on Earth worms, *Lumbriculus variegatus*, was conducted to study the uptake of Ni when the sediment was polluted with Ni. The worms were exposed for 28 days to control and $320\,{}^{\mathrm{mg}}/_{\mathrm{kg}}$ Ni spiked sediment, of which two different types were used, one with low and high binding capacities. Feeding regimes used in the toxicity tests were **(1)** food (Urtica+cellulose) spiked into the sediment with no additional feeding during the exposure (sed+) and **(1)** daily feeding with TetraMin (TM). This $2 \times 2 \times 2$ design ex-

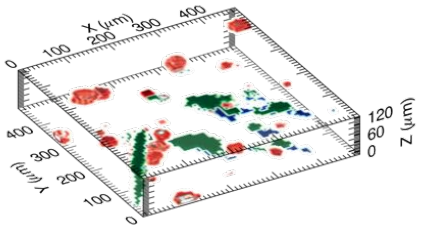

Figure 5.9: 3D reconstruction of the main inclusion of diamond RS55_SL2. K-means clusters are shown: Fe, Ni, Mn (red, minor spots) / Cu, Zn, Ca (green) / Fe (blue).

periment was set up to test the hypothesis that toxicant bioavailability, feeding characteristics and exposure route can affect the performance, response to toxicants and internal toxicant distribution of *Lumbriculus variegatus*.

The internal Ni distributions were obtained using µXRF at the P06 beamline described earlier using the Si(111) monochromator providing a primary X-ray beam of $11.5\,\mathrm{keV}$. To obtain information in the chemically fixed Earth worms, longitudinal cross-sectional images were needed. Since the worms are very long($\sim 3\,\mathrm{cm}$), see Figure 5.10b, longitudinal sections cannot be obtained using scanning CT XRF, while these kind of samples are perfectly suited for the slicing technique. Each cross-sectional image took $1.5\,\mathrm{h}$ to obtain, enabling the study of 57 worms in total.

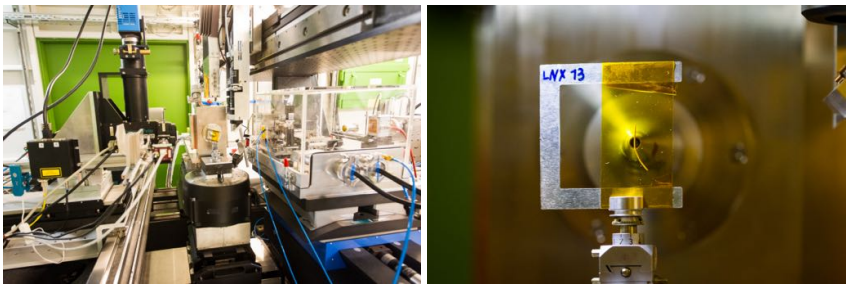

(a) *(b)*

Figure 5.10: ***(a)*** *Showing the general setup used at P06, Petra III* ***(b)*** *The chemically fixed worm, Lumbriculus variegatus mounted on kapton tape in front of the SLcam® detectors 6:1 polycapillary lens.*

5.2.3.2 Results

For the two sediments, no adverse effects were noted in the TM feeding regime. The total number of worms and biomass, however, were significantly reduced under the sed+ feeding mode. The lack of toxicity in the TM treatment was attributed to selective feeding on clean TetraMin and on the daily feeding regime, which promoted the organisms to spend less time in the sediment thus reducing overall Ni exposure The elemental distribution images show, Figure 5.11, that Ni is predominantly accumulated in the epidermis of *Lumbriculus variegatus* fed by clean food (TM) and exposed to a contaminated soil, demonstrating the role of dissolved Ni as the predominant exposure route. The results also show that for both sediments, Ni was predominantly present in the gut area of worms fed via sediment. This highlights the importance of diet-born Ni when contaminated sediment was the only dietary source.

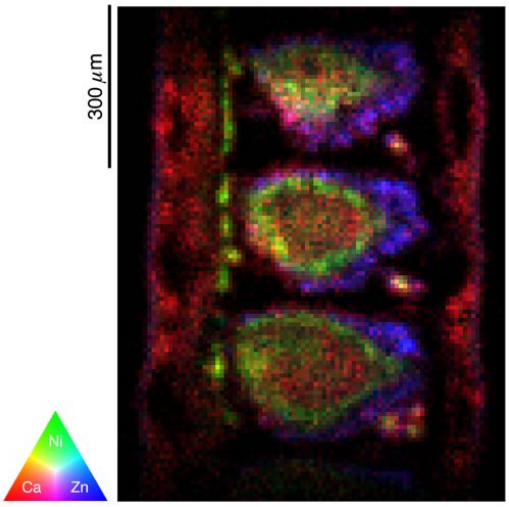

Figure 5.11: Longitudinal cross-section of an Earth worm (Lumbriculus variegatus) depicting the distribution of Ca (red), Ni (green), and Zn (blue), showing the predominant presence of Ni in the gut area.

5.3 Conclusions

The illustrated full-field 3D XRF methodology, using a novel 2D energy dispersive detector (SLcam®), provides a way that allows relatively rapid

analysis of larger volumes in comparison to the currently established techniques such as 3D confocal XRF and XRF tomography, which is of great benefit. To compare the proposed methodology to confocal XRF and XRF tomography we shall compare a virtual sample which measures $2\,\mathrm{mm}$ in each dimension to make a fair comparison. The measurement goal is to reach a 3D representation with a resolution of $8\,\mu\mathrm{m}$ which corresponds to 251 points. For confocal XRF one obtains the following equation to determine the total measurement time assuming a standard measurement time of 1 second per voxel:

$$t(h) = 251^3 \cdot 1\,\mathrm{s} = 4340\,\mathrm{hours} \tag{5.2}$$

Now the same calculation is valid for XRF tomography, except that one dimension is an angular dimension. Therefore using a typical measurement time per pixel of $100\,\mathrm{ms}$, which is typically applied during XRF tomography measurements, one obtains:

$$t(h) = 251^3 \cdot 0.1\,\mathrm{s} = 434\,\mathrm{hours} \tag{5.3}$$

For the proposed full field methodology one gets the following total data collection time when 10 minutes per cross-sectional slice is used:

$$t(h) = 251 \cdot 600\,\mathrm{s} = 42\,\mathrm{hours} \tag{5.4}$$

One can see, when not taking into account limitations caused by self-absorption effects that both confocal XRF and XRF tomography measurements would require a very long acquisition time to obtain fully 3D datasets with these dimensions. XRF tomography on this large data scale only became within reach during recent detector and detector electronic developments, making very short measurement times per pixel possible, for example by using the Maia detector[26]. However, these short dwell times per pixel require a continuous scanning mode by the sample stage, making it a necessity to be able to move the motors accurately at a constant speed and provide a fast readout system for the encoder signal to correlate the measured fluorescent signal to the motor position. The proposed full field methodology for 3D SR-XRF measurements at this scale is the fastest available so far without requiring a continuous/fast sample movement, simply based on a linear scan.
Reconstruction of the datasets of confocal XRF and the full-field methodology are identical. One just needs to correlate each measurement to the right coordinate in 3D, thus making online data visualisation and evaluation possible. Due to the experimental setup and thus the way the data is

collected, no tomographic reconstruction algorithms are needed to reconstruct the measured volume, therefore no possibilities to introduce artefacts as in the case when using tomographic reconstruction algorithms. Online tomographic results, in this case, are only available after sufficient angular information is available, making online data reconstruction and evaluation more difficult. XRF tomography also suffers from excessive reconstruction artefacts in case of the presence of elemental constituents providing fluorescent lines with low statistics.
Large samples or samples consisting of heavy matrices often form a problem or make 3D XRF measurements impossible due to the large influence of self-absorption effects. However, confocal XRF and the described methodology still allow a partial, artefact free image to be obtained unlike tomographic techniques.

5.4 Acknowledgements

Measuring these rare diamond samples was only possible by a collaboration with Prof. Dr. Frank Brenker and Dr. Sylvia Schmitz. The conducted biological measurements were conducted in collaboration with Prof. Dr. Colin Janssen, Dr. Michiel Vandegehuchte, and David Deruytter.

References

[1] J. Garrevoet, B. Vekemans, P. Tack, B. De Samber, S. Schmitz, F. E. Brenker, G. Falkenberg, and L. Vincze. Methodology toward 3d micro x-ray fluorescence imaging using an energy dispersive charge-coupled device detector. *Analytical Chemistry*, 86(23):11826–11832, 2014. doi: 10.1021/ac503410s.

[2] L. Vincze, B. Vekemans, F.E. Brenker, G. Falkenberg, K. Rickers, A. Somogyi, M. Kersten, and F. Adams. Three-dimensional trace element analysis by confocal X-ray microfluorescence imaging. *ANALYTICAL CHEMISTRY*, 76(22):6786–6791, NOV 15 2004. ISSN 0003-2700.

[3] R. Evens, K. A. C. De Schamphelaere, B. De Samber, G. Silversmit, T. Schoonjans, B. Vekemans, L. Balcaen, F. Vanhaecke, I. Szaloki, K. Rickers, G. Falkenberg, L. Vincze, and C. R. Janssen. Waterborne versus Dietary Zinc Accumulation and Toxicity in Daphnia magna: a Synchrotron Radiation Based X-ray Fluorescence Imaging Approach. *ENVIRONMENTAL SCIENCE & TECHNOLOGY*, 46(2):1178–1184, JAN 17 2012. ISSN 0013-936X.

[4] G. Silversmit, B. Vekemans, K. Appel, S. Schmitz, T. Schoonjans, F. E. Brenker, F. Kaminsky, and L. Vincze. Three-Dimensional Fe Speciation of an Inclusion Cloud within an Ultradeep Diamond by Confocal mu-X-ray Absorption Near Edge Structure: Evidence for Late Stage Overprint. *ANALYTICAL CHEMISTRY*, 83(16):6294–6299, AUG 15 2011. ISSN 0003-2700.

[5] O. Scharf, S. Ihle, I. Ordavo, V. Arkadiev, A. Bjeoumikhov, S. Bjeoumikhova, G. Buzanich, R. Gubzhokov, A. Guenther, R. Hartmann, M. Kuehbacher, M. Lang, N. Langhoff, A. Liebel, M. Radtke, U. Reinholz, H. Riesemeier, H. Soltau, L. Strueder, A. F. Thuenemann, and R. Wedell. Compact pnCCD-Based X-ray Camera with High Spatial and Energy Resolution: A Color X-ray Camera. *ANALYTICAL CHEMISTRY*, 83(7):2532–2538, APR 1 2011. ISSN 0003-2700.

[6] I. Ordavo, S. Ihle, V. Arkadiev, O. Scharf, H. Soltau, A. Bjeoumikhov, S. Bjeoumikhova, G. Buzanich, R. Gubzhokov, A. Guenther, R. Hartmann, P. Holl, N. Kimmel, M. Kuehbacher, M. Lang, N. Langhoff, A. Liebel, M. Radtke, U. Reinholz, H. Riesemeier, G. Schaller, F. Schopper, L. Strueder, C. Thamm, and R. Wedell. A new pnCCD-based color X-ray camera for fast spatial and energy-resolved meas-

urements. *NUCLEAR INSTRUMENTS & METHODS IN PHYSICS RESEARCH SECTION A-ACCELERATORS SPECTROMETERS DETECTORS AND ASSOCIATED EQUIPMENT*, 654(1):250–257, OCT 21 2011. ISSN 0168-9002.

[7] M. Radtke, G. Buzanich, J. Curado, U. Reinholz, H. Riesemeier, and O. Scharf. Slicing - a new method for non destructive 3D elemental sensitive characterization of materials. *JOURNAL OF ANALYTICAL ATOMIC SPECTROMETRY*, 29(8):1339–1344, AUG 2014. ISSN 0267-9477. doi: {10.1039/c4ja00085d}.

[8] B. Vekemans, K. Janssens, L. Vincze, F. Adams, and P. Vanespen. ANALYSIS OF X-RAY-SPECTRA BY ITERATIVE LEAST-SQUARES (AXIL) - NEW DEVELOPMENTS. *X-RAY SPECTROMETRY*, 23(6):278–285, NOV-DEC 1994. ISSN 0049-8246.

[9] K.P. Jochum, D.B. Dingwell, A. Rocholl, B. Stoll, A.W. Hofmann, S. Becker, A. Besmehn, D. Bessette, H.J. Dietze, P. Dulski, J. Erzinger, E. Hellebrand, P. Hoppe, I. Horn, K. Janssens, G.A. Jenner, M. Klein, W.F. McDonough, M. Maetz, K. Mezger, C. Munker, I.K. Nikogosian, C. Pickhardt, I. Raczek, D. Rhede, H.M. Seufert, S.G. Simakin, A.V. Sobolev, B. Spettel, S. Straub, L. Vincze, A. Wallianos, G. Weckwerth, S. Weyer, D. Wolf, and M. Zimmer. The preparation and preliminary characterisation of eight geological MPI-DING reference glasses for in-site microanalysis. *GEOSTANDARDS NEWSLETTER-THE JOURNAL OF GEOSTANDARDS AND GEOANALYSIS*, 24(1):87–133, JUN 2000. ISSN 0150-5505.

[10] L. Kempenaers, K. Janssens, K.P. Jochum, L. Vincze, B. Vekemans, A. Somogyi, M. Drakopoulos, and F. Adams. Micro-heterogeneity study of trace elements in USGS, MPI-DING and NIST glass reference materials by means of synchrotron micro-XRF. *JOURNAL OF ANALYTICAL ATOMIC SPECTROMETRY*, 18(4):350–357, 2003. ISSN 0267-9477.

[11] M. J. Walter, G. P. Bulanova, L. S. Armstrong, S. Keshav, J. D. Blundy, G. Gudfinnsson, O. T. Lord, A. R. Lennie, S. M. Clark, C. B. Smith, and L. Gobbo. Primary carbonatite melt from deeply subducted oceanic crust. *NATURE*, 454(7204):622–U30, JUL 31 2008. ISSN 0028-0836.

[12] T. Stachel, G.P. Brey, and J.W. Harris. Kankan diamonds (Guinea) I: from the lithosphere down to the transition zone. *CONTRIBU-*

TIONS TO MINERALOGY AND PETROLOGY, 140(1):1–15, NOV 2000. ISSN 0010-7999.

[13] T. Stachel. Diamonds from the asthenosphere and the transition zone. *EUROPEAN JOURNAL OF MINERALOGY*, 13(5):883–892, SEP-OCT 2001. ISSN 0935-1221.

[14] P.C. Hayman, M.G. Kopylova, and F.V. Kaminsky. Lower mantle diamonds from Rio Soriso (Juina area, Mato Grosso, Brazil). *CONTRIBUTIONS TO MINERALOGY AND PETROLOGY*, 149(4):430–445, JUN 2005. ISSN 0010-7999.

[15] F. V. Kaminsky, G. K. Khachatryan, P. Andreazza, D. Araujo, and W. L. Griffin. Super-deep diamonds from kimberlites in the Juina area, Mato Grosso State, Brazil. *LITHOS*, 112:833–842, NOV 2009. ISSN 0024-4937. 9th International Kimberlite Conference, Johann Wolfgang Goethe Univ, Frankfurt, GERMANY, AUG 10-15, 2008.

[16] F.E. Brenker, T. Stachel, and J.W. Harris. Exhumation of lower mantle inclusions in diamond: ATEM investigation of retrograde phase transitions, reactions and exsolution. *EARTH AND PLANETARY SCIENCE LETTERS*, 198(1-2):1–9, APR 30 2002. ISSN 0012-821X.

[17] F.E. Brenker, L. Vincze, B. Vekemans, L. Nasdala, T. Stachel, C. Vollmer, M. Kersten, A. Somogyi, F. Adams, W. Joswig, and J.W. Harris. Detection of a Ca-rich lithology in the Earth's deep (¿ 300 km) convecting mantle. *EARTH AND PLANETARY SCIENCE LETTERS*, 236(3-4):579–587, AUG 15 2005. ISSN 0012-821X.

[18] R. Tappert, T. Stachel, J.W. Harris, K. Muehlenbachs, T. Ludwig, and G.P. Brey. Subducting oceanic crust: The source of deep diamonds. *GEOLOGY*, 33(7):565–568, JUL 2005. ISSN 0091-7613.

[19] R. Wirth, C. Vollmer, F. Brenker, S. Matsyuk, and F. Kaminsky. Inclusions of nanocrystalline hydrous aluminium silicate "Phase Egg" in superdeep diamonds from Juina (Mato Grosso State, Brazil). *EARTH AND PLANETARY SCIENCE LETTERS*, 259(3-4):384–399, JUL 30 2007. ISSN 0012-821X.

[20] D. G. Pearson, F. E. Brenker, F. Nestola, J. McNeill, L. Nasdala, M. T. Hutchison, S. Matveev, K. Mather, G. Silversmit, S. Schmitz, B. Vekemans, and L. Vincze. Hydrous mantle transition zone indicated by ringwoodite included within diamond. *NATURE*, 507(7491): 221+, MAR 13 2014. ISSN 0028-0836.

[21] T. Stachel, J.W. Harris, G.P. Brey, and W. Joswig. Kankan diamonds (Guinea) II: lower mantle inclusion parageneses. *CONTRIBUTIONS TO MINERALOGY AND PETROLOGY*, 140(1):16–27, NOV 2000. doi: {10.1007/s004100000174}.

[22] G.P. Brey, V. Bulatov, A. Girnis, J.W. Harris, and T. Stachel. Ferropericlase - a lower mantle phase in the upper mantle. *LITHOS*, 77 (1-4):655–663, SEP 2004. ISSN 0024-4937. 8th International Kimberlite Conference, Victoria, CANADA, JUN 22-27, 2003.

[23] Yu. N. Palyanov, Yu. M. Borzdov, Yu. V. Bataleva, A. G. Sokol, G. A. Palyanova, and I. N. Kupriyanov. Reducing role of sulfides and diamond formation in the Earth's mantle. *EARTH AND PLANETARY SCIENCE LETTERS*, 260(1-2):242–256, AUG 15 2007. ISSN 0012-821X.

[24] F. V. Kaminsky and R. Wirth. Iron Carbide Inclusions in Lower-Mantle Diamond from Juina, Brazil. *CANADIAN MINERALOGIST*, 49(2):555–572, APR 2011. ISSN 0008-4476.

[25] B. Vekemans, K. Janssens, L. Vincze, A. Aerts, F. Adams, and J. Hertogen. Automated segmentation of mu-XRF image sets. *X-RAY SPECTROMETRY*, 26(6):333–346, NOV-DEC 1997. ISSN 0049-8246.

[26] R. Kirkham, P. A. Dunn, A. J. Kuczewski, D. P. Siddons, R. Dodanwela, G. F. Moorhead, C. G. Ryan, G. De Geronimo, R. Beuttenmuller, D. Pinelli, M. Pfeffer, P. Davey, M. Jensen, D. J. Paterson, M. D. de Jonge, D. L. Howard, M. Kuesel, and J. McKinlay. The Maia Spectroscopy Detector System: Engineering for Integrated Pulse Capture, Low-Latency Scanning and Real-Time Processing. In Garrett, R and Gentle, I and Nugent, K and Wilkins, S, editor, *SRI 2009: THE 10TH INTERNATIONAL CONFERENCE ON SYNCHROTRON RADIATION INSTRUMENTATION*, volume 1234 of *AIP Conference Proceedings*, pages 240–243, 2 HUNTINGTON QUADRANGLE, STE 1NO1, MELVILLE, NY 11747-4501 USA, 2010. Australian Synchrotron; State Govt Victoria; Australian Govt, Dept Innovat, Ind Sci & Res; Elsevier; Int Atom Energy Agcy; Australian Res Council, Mol & Mat Struct Network; JJ X ray A s; Lightsources, AMER INST PHYSICS. ISBN 978-0-7354-0782-4. 10th International Conference on Synchrotron Radiation Instrumentation, Australian Synchrotron, Melbourne, AUSTRALIA, SEP 27-OCT 02, 2009.

6

Alternative Methodology Towards X-ray Fluorescence Tomography

This chapter describes a new methodology to obtain three dimensional elemental information from a sample with a higher dose efficiency in comparison to the conventional methods.

6.1 Introduction

Chapter 4 and 5 showed approaches towards 2D and 3D elemental imaging using the SLcam® and the necessity the study certain type of samples with a larger field of view. This larger field of view can be limited by self absorption effects, which in certain applications can be solved by using higher X-ray energies, or the field of view is limited by time or dose deposition limitations. Recently a lot of attention has been devoted to studying the impact of radiation damage on the sample and the influence of radiation damage on the obtained results, making scientist rethink certain measurement strategies[1]. The recent technological advances in detector technology, such as the SLcam® and the Maia detector, have already lead to a drastic reduction in measurement time, resulting in a lower dose deposition in the sample[2–4]. Although several three dimensional XRF methodologies exist, each has its advantages and disadvantages. It has been shown that traditional confocal XRF, introduced by Vincze et al. [5], is able to ob-

tain 3D elemental information from the most challenging samples but has the downside of not only being a time consuming process, it only measures a small fraction of the total illuminated mass, thus depositing more radiation in the sample than is strictly necessary. Traditional XRF CT measurements are based on point by point line scans at different angles to obtain a sinogram, which then can be reconstructed into an image. However solving the inverse problem to obtain an image from a sinogram causes inevitable amplification of the data noise reducing the quality of the obtained image[6]. Statistical quality of XRF CT data is mainly determined by the total available experimental time or the dose tolerance of the sample, often causing the obtained statistics to be bad in comparison to what the standard is in absorption CT. One might thus prefer methodologies that immediately obtain elemental images instead of data that still has to be manipulated to obtain one. The slicing methodology, shown in Chapter 5, is one techniques that does not require a reconstruction algorithm to obtain elemental images, while also detecting a larger part of the illuminated mass, enabling a lower sample dosage per imaged area.

6.2 Methodology

The proposed methodology inherits characteristics from classical scanning XRF CT, by using a pencil beam to illuminate the sample, and from the slicing methodology (Chapter 5), by simultaneously collecting the fluorescent radiation from the irradiated matter. This simultaneous collection is achieved by masking a 2D energy dispersive detector, the SLcam® in this case, with a slit mounted perpendicular to the beam direction. A single column from the detector will thus represent a single point along the illuminated path in the sample. 3D elemental distribution images are thus obtained by scanning the pencil beam in the two dimensions perpendicular to the beam direction, acquiring one row along the beam path at a time, illustrated in Figure 6.1.

Since an entire column represents a single point, the effective solid angle of the detector is increased in comparison to the slicing methodology that was described previously. This large solid angle increases the achievable measuring speed, a strategy which is applied in every spectroscopy branch. Fu et al. [6], who conducted similar experiments in parallel to the ones that will be described here, believe to be able to achieved an increase in speed of one order of magnitude with a similar dose than the conventional scanning approach[7]. However, since their experiments were conducted with a CCD with a very limited active thickness, the increase in speed or the dose rate might be approved upon by using an energy dispersive detector, like

the SLcam®, that offers a much higher quantum efficiency.

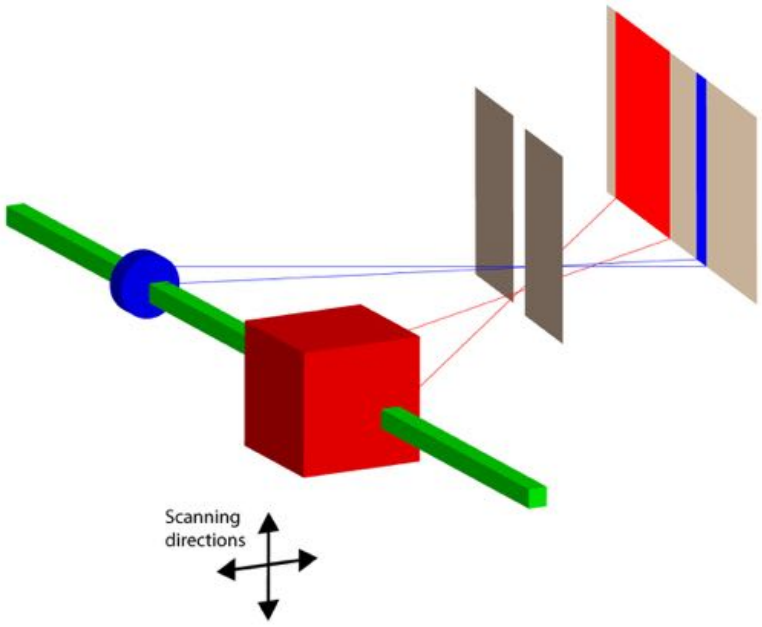

Figure 6.1: Schematic representation of a pencil beam (green) illuminating a line profile in the sample, causing fluorescent X-rays to be detected by a slit collimated pixel detector. Each column on the detector represents a single pixel along the illuminated path.

The use of slits imposes a couple of advantages over the use of imaging optics, like a polycapillary lens or a pinhole optic, as is needed by the methodology described in Chapter 5. First of all, production of slits with a conical shape, increasing the solid angle, with sizes down to $10\,\mu\mathrm{m}$ is easier than perfectly shaped polycapillary or pinhole optics. Secondly, automation of the magnification and the field of view is not possible when working with a fixed optic like a polycapillary lens. Being able to change the slit width and sample - slit - detector distances allow to adapt the achieved field of view and resolution.

Besides the optimisation in scanning speed and amount of radiation deposited, see next section, in the sample, it is applicable over a wide energy range. Polycapillary based techniques offer imaging capabilities in a limited energy range (2 to $20\,\mathrm{keV}$)[5]. Although a germanium based chip is preferred for high energy based measurements, Si based chips can still be used and can even be preferred since the Ge characteristic lines can

more easily cause interference due to spectral overlap with elements of interest. One of the drawbacks of the proposed techniques is the uncertainty involving the attenuation of the fluorescent X-rays when not acquiring any information on the elemental consistency of the material between the illuminated mass and the detector. The lack of information does only allow for an estimation of the attenuation of the fluorescent X-rays.

Absorption CT in general deposits less radiation in a sample compared to XRF measurements, making it a perfect complementary technique to provide three dimensional structural information of a sample. Not only the combination of elemental and structural information is a powerful combination, it also allows for an estimate of the attenuation of the fluorescent X-rays. Although the deduction of the attenuation coefficient is not straight forwards due to the difference in energy between primary X-ray beam used to obtain the absorption CT images and the characteristic elemental line energies.

6.3 Dose estimation

Applied dose to a sample can be calculated using the following formula[6]:

$$D = \Psi \frac{\mu_{en}}{\rho} \tag{6.1}$$

with Ψ being the photon flux of the primary X-ray beam (in $\frac{J}{cm^2}$), and $\frac{\mu_{en}}{\rho}$ the mass energy absorption coefficient.

$$\Psi = kI_0 Et\mathrm{e}^{-\mu x} \tag{6.2}$$

with k a conversion factor ($k = 1.8 \cdot 10^{-16} \frac{J}{keV}$), I_0 the photon flux density (in $\frac{ph}{cm^2 s}$), t the dwell time (in s), and x the probing depth (in cm). For an example shown later on, the total applied dose thus depends on the location of the volume in the sample, therefore as an example the dose is calculated for the centre of a homogeneous cylinder with a diameter of $1\,\mathrm{cm}$ and an $I_0 = 10^{11}\,\frac{\mathrm{ph}}{\mathrm{s}}$. The values used are obtained using Xraylib for $Ca(H_2PO_4)_2$ at $45\,\mathrm{keV}$.

$$D = kI_0 Et \exp\left(-\mu x \frac{\mu_{en}}{\rho}\right) \tag{6.3}$$

$$= 1.8 \cdot 10^{-16} \cdot 10^{11} \cdot 45 \cdot 90 \cdot \exp\left(-1.16 \cdot 0.5 \cdot 0.316\right) \tag{6.4}$$

$$= 12.9\,\mathrm{Gy} \tag{6.5}$$

Although $12.9\,\mathrm{Gy}$ is too high for in vivo imaging, the use of a Ge based detector will reduce the applied dose since it will obtain the same signal to noise ratio in a shorter amount of time due to the higher quantum efficiency. In comparison however to conventional scanning confocal XRF, the gain is equal to the amount of pixels measured simultaneously along the beam path, when not taking into account any efficiency effects from the use of optics. The comparison to scanning XRFCT is more complex to deduct since the dwell time needed to obtain an image with the same dynamic range is not so easily determined. The problem is thus approached by calculating the dwell time that would cause the same dose deposition in the centre of the cylindrical sample. Let us again take the same cylinder of $1\,\mathrm{cm}$ diameter and let the goal be to obtain a resolution of $50\,\mu\mathrm{m}$. One gets the following equation for a single point:

$$t_p = \frac{D}{kI_0 En \exp\left(-\mu x \frac{\mu_{en}}{\rho}\right)} \tag{6.6}$$

$$= \frac{D}{kI_0 E \frac{360^\circ}{\arcsin\frac{50}{5000}} \exp\left(-\mu x \frac{\mu_{en}}{\rho}\right)} \tag{6.7}$$

$$= 0.14\,\mathrm{s} \tag{6.8}$$

This is however without taking into account the decrease in signal to noise level in the reconstructed image. In order to obtain a similar signal to noise level the measurement time per point will need to be increased. 140 Milliseconds per scanning point is within reach using the latest detector technology and high flux beams produced by the latest generation synchrotrons. Fast scanning requires however good sample rigidity and accurate sample stages to ensure proper acquisition of the sinogram.

6.4 Examples

The described experiment was performed at the ID19 - Three-dimensional X-ray Imaging beamline at the ESRF, whose main application is micro CT and phase contrast imaging. This $145\,\mathrm{m}$ long beamline provides a high photon flux with tunable energy between 6 and $250\,\mathrm{keV}$ with the availability of 3 IDs, a wiggler and two undulators. The beamline is equipped with a double Laue or Bragg Si(111) crystal monochromator ($^{\Delta E}/_{E} = 10^{-4}$) and a state of the art multilayer monochromator ($^{\Delta E}/_{E} = 10^{-2}$), the latter was used during the described experiments and tuned to $50\,\mathrm{keV}$. The beam was focussed down using a transfocator to achieve a beam size of $300\,\mu\mathrm{m}\,(\mathrm{H})$ by $150\,\mu\mathrm{m}\,(\mathrm{V})$ measured using a Frelon camera.

Of the examples shown, fluorescence measurements were alternated with absorption CT measurements which can later be merged into a single dataset. Palaeontologists show great interest in dental examination of fossils since a lot of information arises from them, information like general health, diet and living habits[8].

6.4.1 Chimpanzee Molar

The first example shown is of a measurement performed on a molar tooth belonging to a 7.6 year-old wild chimpanzee (*Pan troglodytes*) from the Taï Forest, an evergreen rain forest located in the Ivory Coast, shown in Figure 6.2a. The populations of chimpanzees of this forest are being studied for over three decades by Prof. Boesch and his colleague primatologists, especially from the Department of Primatology, at the Max Planck Institute for Evolutionary Anthropology (MPI-EVA) in Leipzig, Germany[9–11]. The individual was named Lefkas by the primatologists that did observe him during his lifetime in the forest. At the death of the individual, the cadaver was buried for facilitating decay and the skeletal remains are prepared and transported to the MPI-EVA, where the osteological collection of the Taï chimpanzees is housed in the Department of Human Evolution.

Figure 6.2 shows the general setup used during the measurements, showing the SLcam® covered with lead lining to protect it from the primary X-ray beam on the right, an aluminium/lead sandwich plate at the front of the detector housing the $75\,\mu\mathrm{m}$ wide slit, and on the left two stacked teeth. $50\,\mathrm{keV}$ was chosen as an excitation energy to be able to excite the Ba K shell electrons ($37.44\,\mathrm{keV}$) and shift the broad Compton peak, caused by multiple Compton scattering, far enough to high energy to increase to peak to background ratio of the Ba-Kα line. An extra benefit of the high energy of the primary X-ray beam is the lower attenuation in the sample, the relatively high energy of the Ba-Kα photons provides greater possible information depths. The teeth were aligned in a way that a vertical line scan could be performed through the cusps of the molar closest to the detector. Each line was measured for $150\,\mathrm{s}$ with a step resolution of $125\,\mu\mathrm{m}$, imaging a cross-sectional area of the top tooth of about $12\,\mathrm{mm}\,(\mathrm{H})$ by $16\,\mathrm{mm}\,(\mathrm{V})$ in $5\,\mathrm{h}$ with an estimated resolution between 75 and $125\,\mu\mathrm{m}$. The obtained Ba image, Figure 6.3, reveals the different growth layers inside the molar of the primate, enabling the palaeontologists to extract information on for example breastfeeding behaviour of primates.

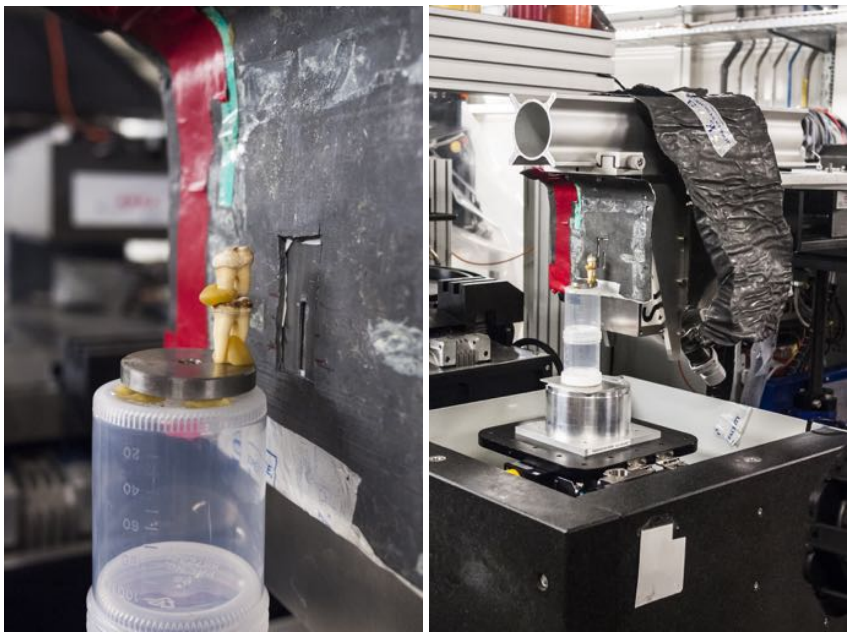

(a) *(b)*

Figure 6.2: ***(a)*** *Two primate molar teeth mounted as a stack in front of the SLcam® collimated by a slit.* ***(b)*** *A general overview image of the measurement setup at ID19, ESRF.*

6.4.2 Neanderthal Cheekbone

The investigated cheekbone with teeth originates from a Neanderthal fossil that was found in the province of Liège, Belgium in 1830 but was only classified as a Neanderthal fossil in 1936. The fossil in question is 30000 years old and is of a child that died at an age of 3. The used setup is the same as described previously, a measurement time of $90\,\mathrm{s}$ per line with a step size of $60\,\mu\mathrm{m}$. The sample in question is more challenging than the one shown previously since the teeth of interest are still located inside the cheekbone. Sample alignment was performed using the beforehand acquired absorption CT images, shown in Figure 6.4. Figure 6.5 depicts the Ba distribution, nicely showing the two teeth inside the cheekbone of the Neanderthal fossil. This clearly proves that tomographic information can be extracted from deeper within a sample using this proposed methodology.

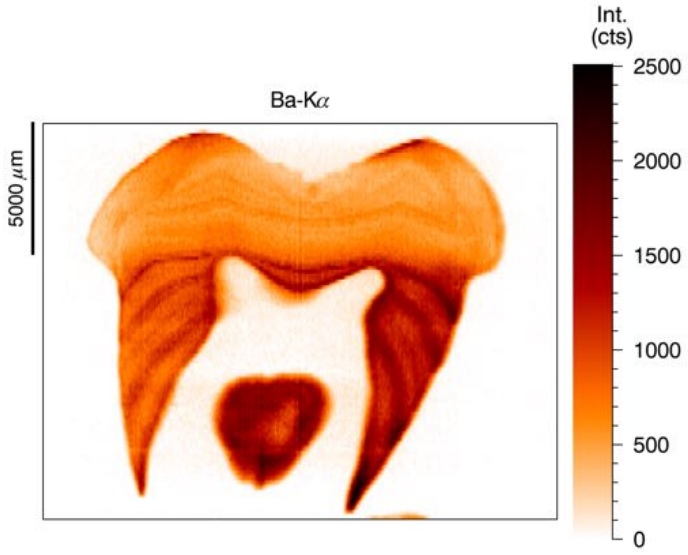

Figure 6.3: The Ba distribution inside a molar of a primate.

6.5 Conclusion

The presented elemental distribution images show that the proposed methodology provides the possibility to extract tomographic XRF information from within samples with a resolution below $100\,\mu\mathrm{m}$. Since no reconstruction algorithms are needed to obtain tomographic cross-sections, no artefacts can be introduced or image noise being amplified. Due to the optimisation of the detection strategy, the applied dose level is lower than for scanning confocal XRF. Compared to scanning XRF CT, the applied dose can be equal when making use of large area SDD detector with fast pulse processing units. Of course, the more pixels simultaneously measured using the proposed strategy the higher the efficiency will be and the more dose efficient it will be in comparison to other point by point scanning based techniques. To truly compare the different tomographic techniques, one would need to perform measurements on a test samples with the goal to obtain images with the same signal to noise ratio. A downside however is the lack of information of the attenuating material between the illuminated mass and the detector, when not imaging the entire sample, not allowing a correction for self-absorption effects without making assumptions about the sample. This can be partly circumvented by combining the obtained XRF dataset with an absorption CT dataset, allowing for an estimate of the

(a) *(b)*

Figure 6.4: ***(a)*** *Visual alignment using the beforehand acquired absorption CT images.* ***(b)*** *The Neanderthal cheekbone mounted in front of the SLcam® collimated with a vertical slit.*

attenuation coefficients of the photon path.

Further improvements to the system can be an automation of the slit gap and the possibility to on the fly change the sample-slit and slit-detector distances to enable on the fly adaptation of the field of view/resolution.

Acknowledgements

This study was performed in collaboration with Dr. Paul Tafforeau, Dr. Adeline Le Cabec of ID19, ESRF and Dr. Anne Bonnin of Tomcat, PSI. We are grateful to the department of Human Evolution and Primatology of the Max Planck Institute for Evolutionary Anthropology for providing access to the Taï chimpanzee tooth.

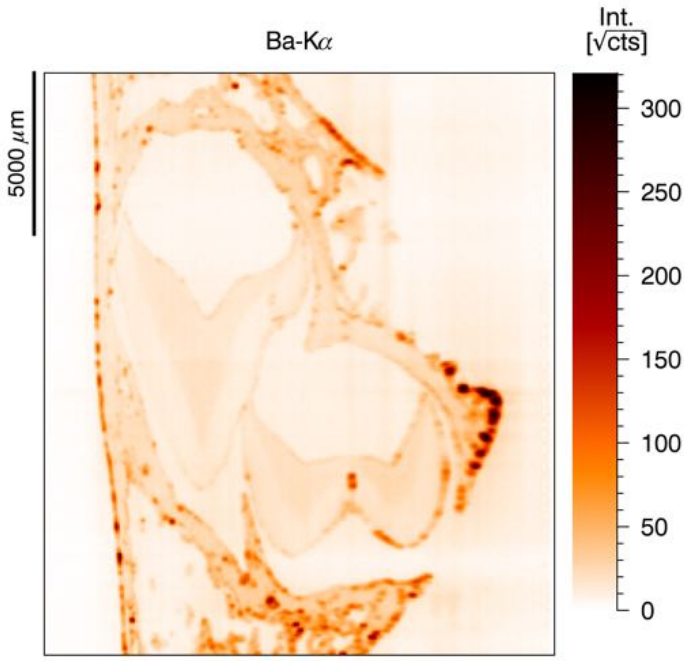

Figure 6.5: Ba distribution of a Neanderthal cheekbone with 2 teeth inside.

References

[1] S. Storm, M. Ogurreck, D. Laipple, C. Krywka, M. Burghammer, E. Di Cola, and M. Müller. On radiation damage in FIB-prepared softwood samples measured by scanning X-ray diffraction. *Journal of Synchrotron Radiation*, 22(2):267–272, Mar 2015. doi: 10.1107/S1600577515001241. URL `http://dx.doi.org/10.1107/S1600577515001241`.

[2] J. Garrevoet, B. Vekemans, P. Tack, B. De Samber, S. Schmitz, F. E. Brenker, G. Falkenberg, and L. Vincze. Methodology toward 3d micro x-ray fluorescence imaging using an energy dispersive charge-coupled device detector. *Analytical Chemistry*, 86(23):11826–11832, 2014. doi: 10.1021/ac503410s.

[3] P. Tack, J. Garrevoet, S. Bauters, B. Vekemans, B. Laforce, E. Van Ranst, D. Banerjee, A. Longo, W. Bras, and L. Vincze. Full-Field Fluorescence Mode Micro-XANES Imaging Using a Unique Energy Dispersive CCD Detector. *Analytical Chemistry*, 86(17): 8791–8797, SEP 2 2014. ISSN 0003-2700. doi: {10.1021/ac502016b}.

[4] M.D. de Jonge, C.G. Ryan, and C.J. Jacobsen. X-ray nanoprobes and diffraction-limited storage rings: opportunities and challenges of fluorescence tomography of biological specimens. *JOURNAL OF SYNCHROTRON RADIATION*, 21(5):1031–1047, SEP 2014. ISSN 0909-0495. doi: {10.1107/S160057751401621X}.

[5] L. Vincze, B. Vekemans, F.E. Brenker, G. Falkenberg, K. Rickers, A. Somogyi, M. Kersten, and F. Adams. Three-dimensional trace element analysis by confocal X-ray microfluorescence imaging. *ANALYTICAL CHEMISTRY*, 76(22):6786–6791, NOV 15 2004. ISSN 0003-2700.

[6] G. Fu, L.-J. Meng, P. Eng, M. Newville, P. Vargas, and P. La Riviere. Experimental demonstration of novel imaging geometries for x-ray fluorescence computed tomography. *MEDICAL PHYSICS*, 40(6), JUN 2013. ISSN 0094-2405. doi: {10.1118/1.4801907}.

[7] L.J. Meng, N. Li, and P.J. La Riviere. X-Ray Fluorescence Emission Tomography (XFET) With Novel Imaging Geometries-A Monte Carlo Study. *IEEE TRANSACTIONS ON NUCLEAR SCIENCE*, 58 (6, 2):3359–3369, DEC 2011. ISSN 0018-9499. doi: {10.1109/TNS.2011.2167632}.

[8] C. Austin, T. M. Smith, A. Bradman, K. Hinde, R. Joannes-Boyau, D. Bishop, D. J. Hare, P. Doble, B. Eskenazi, and M. Arora. Barium distributions in teeth reveal early-life dietary transitions in primates. *NATURE*, 498(7453):216+, JUN 13 2013. ISSN 0028-0836. doi: {10.1038/nature12169}.

[9] C. Boesch and H. Boesch. Hunting Behavior of Wild Chimpanzees in the Tai-National-Park. *AMERICAN JOURNAL OF PHYSICAL ANTHROPOLOGY*, 78(4):547–573, APR 1989. ISSN 0002-9483. doi: {10.1002/ajpa.1330780410}.

[10] T. M. Smith, B. H. Smith, D. J. Reid, H. Siedel, L. Vigilant, J. J. Hublin, and C. Boesch. Dental development of the Tai Forest chimpanzees revisited. *JOURNAL OF HUMAN EVOLUTION*, 58(5):363–373, MAY 2010. ISSN 0047-2484. doi: {10.1016/j.jhevol.2010.02.008}.

[11] B. H. Smith and C. Boesch. Mortality and the magnitude of the "wild effect" in chimpanzee tooth emergence. *JOURNAL OF HUMAN EVOLUTION*, 60(1):34–46, JAN 2011. ISSN 0047-2484. doi: {10.1016/j.jhevol.2010.08.006}.

7

Development and Applications of a Laboratory μXRF Spectrometer using Monochromatic Excitation for Quantitative Elemental Analysis

As published:
J. Garrevoet, B. Vekemans, S. Bauters, A. Demey, and L. Vincze. Development and applications of a laboratory micro x-ray fluorescence (xrf) spectrometer using monochromatic excitation for quantitative elemental analysis. *Analytical Chemistry*, 2015. doi: 10.1021/acs.analchem.5b00770

The analytical characterisation and an application example of a novel laboratory X-ray fluorescence (μXRF) microprobe is presented, which combines monochromatic, focused X-ray beam excitation with a high-performance silicon drift detector (SDD) and 2D/3D scanning capability. Due to the monochromatic excitation, below the (multiple) Compton/Rayleigh scatter peak region, the XRF spectra obtained by this laboratory spectrometer has similarly high peak-to-background ratios as can be obtained at synchrotron sources. As a result, sub-ppm minimum detection limits (MDL) for transition metals are obtained for a variety of sample matrices. The monochromatic excitation also allows for the efficient use of an iterative Monte Carlo simulation algorithm to obtain quantitative information of the analysed samples. The analytical characteristics of this instrument and quantitative results in combination with an iterative reverse Monte Carlo simulation algorithm will be demonstrated using measurements conducted on an iron containing meteorite.

7.1 Introduction

Laboratory micro X-ray fluorescence (XRF) spectrometers are indispensable tools in many fields of research, evolving rapidly and offering a high level of accessibility in comparison with e.g. state-of-the-art μXRF spectrometers installed at synchrotron radiation sources. Rapid advances in the design of the different components (X-ray source, focusing optics, detectors) result in more and more sensitive instruments with a higher flux in smaller X-ray spots, making laboratory XRF imaging at these micron-scale resolutions possible[2–5].

Advances in X-ray tube technology, such as the ULTRA-LITE X-ray source from Moxtek[6] or the field emitter based X-ray tubes[7] which both can be battery operated, make new developments in portable or hand held systems for on site analysis, which is often needed in e.g. archaeology and geology, possible[8–10].

A recent trend in μXRF imaging is represented by advances in three-dimensional (3D) elemental imaging. At synchrotron radiation (SR) based instruments this is to a large extent enabled by the application of new detector types and detection modes, based on either full-field detectors or fast, large solid angle, multi-element detectors making sub-millisecond dwell times possible[11–13]. This trend is not only seen at SR facilities but also in the laboratory environment by the development of confocal detection based 3D-XRF spectrometers coupled with the development of algorithms needed to obtain quantitative information of the sample in question[3, 14–19]. A third avenue of development is represented by the combination of several

techniques into one laboratory instrument such as the combination of XRF with Raman spectroscopy or the combination of XRF/XRD[20, 21].
This paper describes a laboratory XRF microprobe which differs from commercially available spectrometers by the fact that it is mainly optimised for elemental sensitivity instead of ultimate spatial resolution. This is achieved by using a custom-made version of a commercially available microfocus X-ray source equipped with large, three-segment Doubly Curved Crystal (DCC) optics (X-ray Optical Systems, Albany, NY, USA). The latter is not only used as a focussing optic but also as a monochromator for the X-ray beam. The application of the monochromatic microbeam not only increases dramatically the measured peak-to-background ratios, but it also eliminates uncertainties associated with the energy-distribution of the polychromatic excitation spectrum when using fundamental parameter or Monte Carlo based quantification algorithms. Both of these aspects represent a major advantage compared to currently available mainstream microbeam XRF spectrometers. Next to characterising the produced monochromatic X-ray microbeam, the achievable analytical characteristics of the self-developed XRF microprobe are presented below. As an application example, quantitative XRF scan results on a rare meteoritic material[22] are shown to illustrate the analytical capabilities of this instrument. The quantitative μXRF results are obtained by the use of iterative reverse Monte Carlo[23] simulations using the XMI-MSIM package[24–29]. This way of quantitative analysis of scanning μXRF data-sets becomes possible by taking advantage of the monochromatic nature of the X-ray excitation, representing the cutting edge of quantitative analysis in XRF-spectrometry.

7.2 Experimental

The monochromatic μXRF laboratory setup, shown in Figure 7.1 was developed at the X-ray Microscopy and Imaging group (XMI) of Ghent University. The instrument is based on a custom-made air-cooled X-Beam source ($50\,\mathrm{W}$) manufactured by X-ray Optical Systems Inc. (XOS), Albany, USA. The employed X-Beam source uses a microfocus X-ray tube with a molybdenum anode to generate the primary X-ray beam, which is focused and monochromatised at the energy of the Mo-Kα line ($17.4\,\mathrm{keV}$) by a doubly curved crystal (DCC) having three segments providing a large subtended X-ray source emission solid angle. The optic produces a strongly focused beam having a divergence of 27 degrees horizontally and 0.6 degrees vertically. The diffraction based focusing results in a monochromatic X-ray micro beam with a high flux density having FWHM values of $120\,\mu\mathrm{m}$ horizontally by $46\,\mu\mathrm{m}$ vertically at a focal distance of $32\,\mathrm{mm}$. The X-ray

source is controlled by a PCS-50 (XOS), high voltage power supply with an integrated controller, to obtain high degrees of stability under changing temperature and power conditions. The sample scanning stage consists of three Physik Instrumente (Karlsruhe, Germany) M-410.DG linear stages ($100\,\mathrm{mm}$ travel, $0.1\,\mu\mathrm{m}$ minimum step size), controlled by a C-863 DC controller, and a PI M-660.55 rotation stage ($34\,\mu\mathrm{rad}$ minimum step size), controlled by a C-867 piezo controller, which are mounted in an XYZΘ-geometry. The X-ray fluorescent radiation is detected under 90 degrees relative to the incoming X-ray micro beam by a SiriusSD Silicon Drift detector (e2v, Essex, United Kingdom) having an active area of $60\,\mathrm{mm}^2$, with an energy resolution $< 160\,\mathrm{eV}$ for commonly used peaking times and is controlled by the DX1 controller of e2v. The detector can be equipped with different collimators, changing the subtended detection solid-angle or adding certain filters. Special multilayer collimators have been designed to avoid spectral artefacts caused by internal fluorescence of the collimator material. A long working distance Dino-Lite digital microscope (Dino-Lite Europe, Naarden, The Netherlands) with a maximum magnification of $90\times$ is used for alignment and positioning of the sample and is placed under 45 degrees with respect to the primary X-ray micro beam. The X-ray source, motors and detector are controlled by a standard desktop computer running an in-house developed scanning software with online spectrum evaluation built in. Static (step-wise scanning) and dynamic (continuous scanning) data acquisition modes are incorporated.

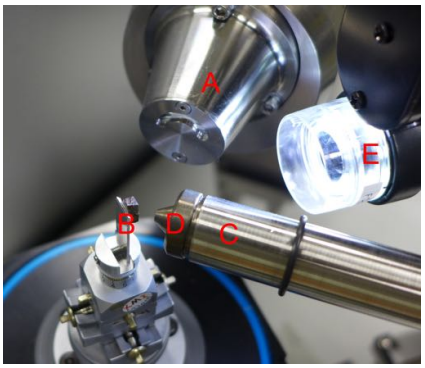

Figure 7.1: Optical image of the laboratory μXRF spectrometer showing the monochromatic X-ray source (A), the sample mounted on the XYZθ motor stages (B), and the SDD detector (C) with a Mo based conical collimator (D) in a 90 degree geometry. The Dino-Lite optical microscope (90×) (E), mounted perpendicularly to the sample surface, is used to position the sample in the focal plane of the monochromatic X-ray source and to provide an optical view of the measured sample area.

7.3 Results and Discussion

7.3.1 Source Performance

Beam size The beam size achieved by the DCC optics was measured by performing line scans with a resolution of $10\,\mu\mathrm{m}$ (H) and $5\,\mu\mathrm{m}$ (V) with a dwell time of $60\,\mathrm{s}$ (live time, LT) at the focal distance over a cross consisting of $10\,\mu\mathrm{m}$ stainless steel wires (Goodfellow, London, United Kingdom). The obtained results are shown in Figure 7.2 corresponding to a measured horizontal Gaussian width of $120\,\mu\mathrm{m}$ (FWHM) and a vertical beam size of $46\,\mu\mathrm{m}$ (FWHM), as determined using the Fe signal.

The beam size measurements for Cr and Ni are identical to the results obtained by the Fe signal due to the monochromaticity of the used X-ray source. Although the achieved beam size is not in competition with state-of-the-art polycapillary based systems, which achieve beam sizes down to $2.5\,\mu\mathrm{m}$ and even $1\,\mu\mathrm{m}$ has been reported feasible, these systems lack the versatility due to the very short working distance[5, 15]. Portable systems, do not provide the ability for elemental imaging, therefore the average beam size is in the $0.5 - 3\,\mathrm{mm}$ range[6, 9, 21, 30].

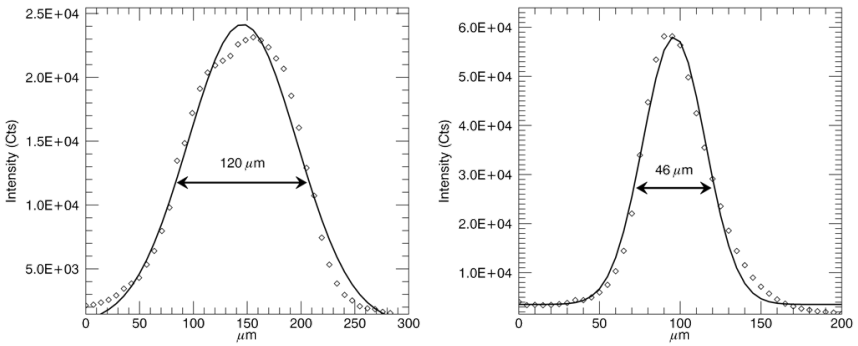

Figure 7.2: Results from a linear wire scan to determine the beam size achieved by the DCC optics at a focal distance of $32\,\mathrm{mm}$*, resulting in a horizontal beam size of* $120\,\mu\mathrm{m}$ *(FWHM)* ***(a)*** *and a vertical beam size of* $46\,\mu\mathrm{m}$ *(FWHM)* ***(b)****.*

Flux In order to determine the X-ray flux and the effective degree of linear polarisation in the horizontal plane (which arises from the use of diffractive optics), a Monte Carlo simulation of an XRF spectrum obtained from an NIST Standard Reference Material (SRM) 1155 (Stainless steel) was performed using the in-house developed XMI-MSIM software package[24]. The standard was measured in a 2D scanning mode consisting of 3×3 points of $50\,\mathrm{s}$ live time (LT) with a step size of $250\,\mu\mathrm{m}$ to achieve better statistical sampling using an X-ray tube setting of $40\,\mathrm{kV}$, $0.4\,\mathrm{mA}$. A sum spectrum was obtained by summing each individual pixel spectrum which was then used as a reference for the Monte Carlo simulation. These simulations resulted in a flux of $1.21 \pm 0.03 \times 10^7\ \frac{\mathrm{ph}}{\mathrm{s}}$ with a degree of polarisation of $14.4\,\%$ and an energy bandwidth of $1.5\,\%\frac{\Delta\mathrm{E}}{\mathrm{E}}$. When operating the X-ray tube at maximum power ($40\,\mathrm{kV}$, $1.0\,\mathrm{mA}$) this results in a photon flux of $3.02 \times 10^7\ \frac{\mathrm{ph}}{\mathrm{s}}$. Monochromatised microfocus X-ray tubes were not used in the past due to the low efficiency of the monochromatising optics, but when compared to X-ray sources based on the same model but equipped with other focusing optics (polycapillary, $7.4 \times 10^7\ \frac{\mathrm{ph}}{\mathrm{s}}$ / monocapillary, $2.54 \times 10^6\ \frac{\mathrm{ph}}{\mathrm{s}}$, determined by X-ray Optical Systems Inc. (XOS), Albany, USA) it is clear that advances in optics technology have made monochromatic laboratory μXRF spectrometers possible[3]. When compared to high power tubes like the MetalJet D2 of Excillum, which have a flux in the order of $10^{10}\ \frac{\mathrm{ph}}{\mathrm{s}}$ when coupled with a elliptical mirror optic (Incoatec GmbH, Germany and Excillum, Sweden), which is on par with the currently available rotating anode X-ray sources offered by companies as

Rigaku, the flux obtained from the monochromatic source is 2-3 orders of magnitude lower but also costs a fraction of the price of a high power rotating anode or MetalJet X-ray source. Future developments on the MetalJet technology will allow for a gain of 100 in intensity while being compatible with DCC optics[15, 31]. Portable equipment is often battery operated, using low power X-ray tubes delivering a significantly lower flux compared to standard laboratory systems[32, 33].

Monochromaticity For applications such as X-ray diffraction, the energy profile of the beam is an important parameter. To be able to determine the FWHM of the energy distribution of the generated (quasi) monochromatic microbeam, the detector response at the energy of Mo-Kα needs to be known since the experimental profile of the Rayleigh scatter peak is a convolution of the energy distribution of the beam and the detector response. The energy resolution of the detector is given by:

$$\Delta E_{res} = \sqrt{\Delta E_{det}^2 + \Delta E_{elec}^2} \tag{7.1}$$

$$E_{det} = 2\sqrt{2\ln(2) F \epsilon E} \tag{7.2}$$

$$E_{elec} = 2\sqrt{2\ln(2)\epsilon \frac{ENC}{q}} \tag{7.3}$$

where E_{res} is the obtained energy resolution of the spectroscopic system, E_{det} is the detector processes contribution, E_{elec} detector electronics noise contribution, E the photon energy in eV, F the fano factor (0.11 for Si) and ϵ the mean energy required to produce a single electron-hole pair (3.62 eV for Si), ENC the equivalent noise charge and q the electron charge[34]. Since the ENC is solely depending on the used shaping time and used filters, it is energy independent.

By applying equations 7.2 and 7.3 to calculate the energy response at the Mo-Kα energy and taking into account the FWHM of the energy distribution of the focused beam, one gets:

$$\begin{aligned}\Delta E_{Mo-K\alpha} &= \sqrt{\Delta E_{det_{Mo-K\alpha}}^2 + \Delta E_{elec}^2 + \Delta E_{source}^2} \\ &= \sqrt{\Delta E_{det_{Mo-K\alpha}}^2 + \Delta E_{Mn-K\alpha}^2 - \Delta E_{det_{Mn-K\alpha}}^2 + \Delta E_{source}^2}\end{aligned} \tag{7.4}$$

with:

$$\Delta E^2_{det_{Mo-K\alpha}} = \left(2\sqrt{2\ln(2)F\epsilon E_{Mo-K\alpha}}\right)^2 \tag{7.5}$$

$$\Delta E^2_{det_{Mn-K\alpha}} = \left(2\sqrt{2\ln(2)F\epsilon E_{Mn-K\alpha}}\right)^2 \tag{7.6}$$

The Rayleigh scatter peak of the experimentally obtained spectrum was fitted with a Gaussian, resulting in an $\Delta E_{Mo-K\alpha}$ of 261 eV. The FWHM of the energy profile can thus be calculated by reforming equation 7.4:

$$\begin{aligned}\Delta E_{source} &= \sqrt{\Delta E^2_{Mo-K\alpha} - \Delta E^2_{det_{Mo-K\alpha}} - \Delta E^2_{Mn-K\alpha} + \Delta E^2_{det_{Mn-K\alpha}}} \\ &= 139\,\mathrm{eV}\end{aligned} \tag{7.7}$$

The FWHM of the energy distribution of the focused excitation beam is therefore:

$$\frac{\Delta E}{E} = \frac{139\,\mathrm{eV}}{17479\,\mathrm{eV}} = 0.795\,\% \tag{7.8}$$

Therefore, the monochromaticity is not as good as one obtains using a Si111 monochromator, which is typically in the order of 10^{-4} $\Delta\mathrm{E}/\mathrm{E}$, but is comparable to a multilayer monochromator producing a pink beam with an energy profile width in the order of 10^{-2} $\Delta\mathrm{E}/\mathrm{E}$. The suppression of the Mo-Kb line by the diffractive optics was determined by comparing the theoretical Mo-Kβ intensity to the Mo-Kβ intensity used as input for the Monte Carlo simulations. These calculations resulted in a $\frac{K\beta_{exp}}{K\beta_{theory}}$ of 10 %.

7.3.2 Analytical characteristics

Several analytical characteristics were examined to evaluate the performance of this μXRF spectrometer based on monochromatic radiation, as detailed below.

Energy Resolution The energy resolution of the obtained XRF spectra for different detector peaking times (PT) (0.8 - 50 μs) as a function of incoming count rates (ICR) were determined by measuring an iron foil and fitting the Fe-Kα signal with a Gaussian, using the fitted FWHM value as the measure of the energy resolution. Figure 7.3a shows the energy resolution as a function of the incoming count rate, obtained by increasing the X-ray tube current, for different peaking times, resulting in an increase of energy resolution with longer peaking times, except for the 50 μs PT where the energy resolution decreases again. Furthermore, it shows that the energy resolution is not affected by the incoming count rate. Figure 7.3b

shows the detector dead time as a function of effectively detected count rate (OCR) for different detector electronics peaking times. Using a peaking time of 3 µs represents a good compromise between detector throughput and achievable energy resolution. These results lay in the expected range of what is currently achieved by other laboratory based systems[33].

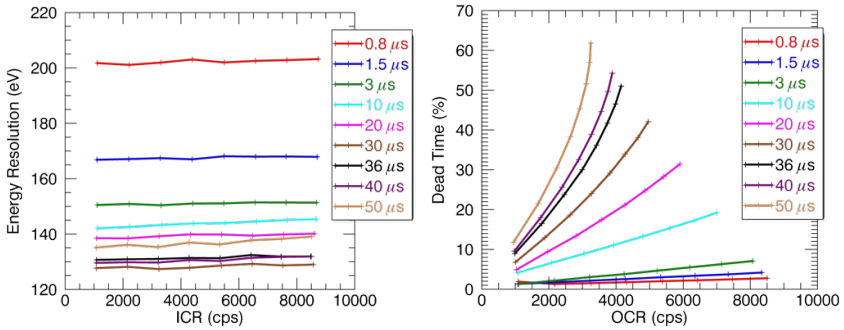

Figure 7.3: Performance of the applied energy-dispersive detector in terms of energy resolution (a) and dead time (b) for different peaking times.

Spectral quality In order to evaluate the spectral quality of the attainable XRF spectra, measured XRF distributions were compared to data obtained from monochromatic excitation based µXRF experiments performed at a synchrotron microprobe. Figure 7.4 shows an XRF spectrum of an NIST SRM 1577c pressed pellet sample measured at beamline L (DORIS III, DESY, Hamburg, Germany), compared to a spectrum obtained by the laboratory microprobe described in this paper. In both cases the standard reference material was measured for 1000 s, the excitation energy at the bending magnet beamline was 17.5 keV while the laboratory source has a fixed excitation energy of 17.4 keV. Since the intensity of the primary synchrotron beam is much higher (i.e. by 2-3 orders of magnitude), the synchrotron spectrum was scaled by a factor of 36 to obtain the same Cu signal level. This scaling factor is less then the ratio of the primary beam intensities, as the lack of beam intensity in case of the laboratory source is partially compensated by the larger detection solid angle employed. As illustrated in Figure 7.4, the scatter signal of the synchrotron measurement is lower in intensity and shows less tailing due to the much higher degree of linear polarisation of the primary beam while the intensity of the fluorescent lines of the lower atomic number elements are less intense, due to the larger air

path between the sample and detector. For the region ranging from Ca to Br both spectra have similar peak to background ratios, showing the excellent quality of the monochromatically excited XRF spectra obtained by this spectrometer. Due to the excellent peak-to-background ratios of the collected XRF-spectra, this instrument offers a leap forward for quantitative 2D elemental imaging of trace elements with significantly improved detection limits compared state-of-the-art polycapillary based systems albeit with lower spatial resolution[16, 33].

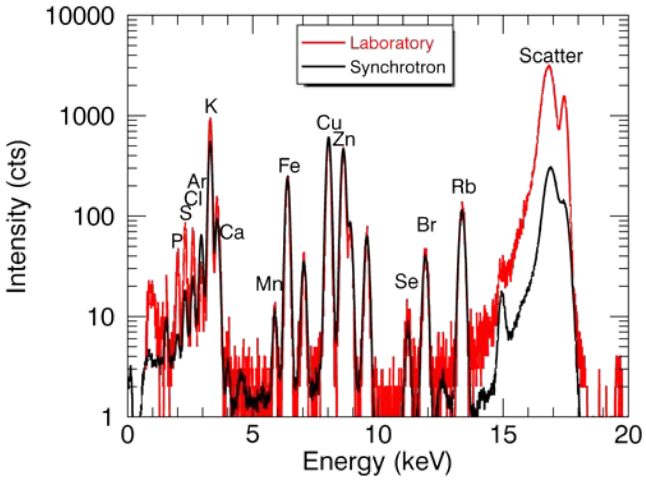

Figure 7.4: Comparison of XRF spectra obtained at a bending magnet beamline (beamline L, DORIS III, DESY) and the laboratory instrument to evaluate the XRF spectral quality achievable with this monochromatic instrument. The spectra were scaled to the maximum of the Cu-Kα fluorescent peak. (Measurement time = 1000 s, synchrotron: $E_0 = 17.5\,\mathrm{keV}$, laboratory: $E_0 = 17.4\,\mathrm{keV}$, synchrotron spectrum was normalised using the Cu-Kα signal, normalisation factor 36).

Detection Limits The achievable detection limits were determined using the standard reference material NIST SRM 1577c, a biological standard (bovine liver powder) pressed as an approximately $100\,\mu\mathrm{m}$ thick pellet with a diameter of $13\,\mathrm{mm}$. A 2D mapping was performed in order to reduce the effects of potential inhomogeneity of the pellet, a 3×3 grid of $1000\,\mathrm{s}$ (LT) point measurements with a grid size of $250\,\mu\mathrm{m}$ was measured using an X-ray tube setting of $40\,\mathrm{kV}$ and $0.4\,\mathrm{mA}$. For a biological matrix, the relative detection limits for a $1000\,\mathrm{s}$ measurement range approximately from $750\,\mathrm{ppm}$ for P, which is excited relatively inefficiently by the $17.4\,\mathrm{keV}$ beam and suffers from considerable absorption effects by the am-

bient air and detector window, to sub-ppm detection limit values (down to $\sim 400\,\mathrm{ppb}$) in the atomic number range of 29-37, see Figure 7.5a. In terms of absolute detection limits this translates to values below $1\,\mathrm{pg}$ for elements in the atomic number range of 25-37 (see Figure 7.5b.

The presented detection limits were calculated using[11]:

$$DL_i = \frac{3\sqrt{B_i}}{N_i} c_i \tag{7.9}$$

where DL_i represents the detection limit for element i, B_i the background intensity of element , and N_i the net intensity of the Kα or Lα peak of element i. For the absolute detection limits, the information depth, which represents the sample thickness which produces $99\,\%$ of the total fluorescence intensity, was calculated using:

$$\frac{I_i\left(d_{info}\right)}{I_i\left(\infty\right)} = 1 - \mathrm{e}^{-\chi\rho d_{info}} = 0.99 \tag{7.10}$$

$$d_{info} = \frac{ln100}{\rho\chi} \tag{7.11}$$

$$\text{with} \quad \chi = \frac{\mu_0}{\sin\alpha} + \frac{\mu_i}{\sin\beta} \tag{7.12}$$

with ρ the density, μ_0 the mass attenuation coefficient, determined using Xraylib[35], of the primary X-ray beam, μ_i the mass attenuation coefficient of element i, and α and β the angles between primary X-ray beam and sample, and sample and detector axis respectively. The probing volume can thus be determined using the information depth, beam size of the primary X-ray beam, and instrument geometry and converted into illuminated mass using the certified concentrations, which can then be used in Equation 7.9 to calculate the absolute detection limits. Error estimation is done by standard error propagation of the background and net intensities, and concentrations of the SRM, if supplied by the manufacturer. The plotted error bars represent 2σ.

Synchrotron based XRF, gains in general 1 order of magnitude lower detection limits. Compared to other laboratory based systems, the obtained detection limits of the presented system are 1 order of magnitude or more better, enabling to scan considerably faster than other polychromatic based (confocal or conventional) laboratory systems, while reaching the same detection limits as these systems[16, 36]. These levels of detection lead the way to 2D measurements of samples with lower trace elemental concentrations than is possible with polychromatic microbeam based spectrometers. The shorter measuring times required allows the user to measure larger

areas while still operating at the same levels of detection as currently available laboratory systems.

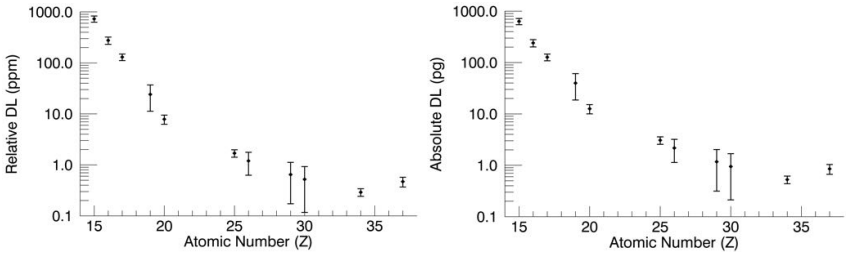

(a) *(b)*

Figure 7.5: The relative (in ppm) ***(a)*** *and absolute (in pg)* ***(b)*** *detection limits for a* $1000\,\mathrm{s}$ *measurement of the NIST SRM 1577c (biological standard) using an X-ray tube setting of* $40\,\mathrm{kV}$ *and* $0.4\,\mathrm{mA}$.

7.3.3 Software

To control the spectrometer and to provide the user with online data evaluation, in-house scanning software was written in IDL language (Exelis Visual Information Solutions, Boulder, Colorado, USA). The software allows for static (step-wise) and dynamic (continuous) scanning of the sample in a repeated line or 'snake' pattern. Using the dynamic scan in the latter mode it is possible to make quick overview images for better alignment of the region of interest and for the estimation of the required detector dwell time per pixel.

7.3.4 Quantification

Due to the monochromatic nature of the developed instrument, quantification via reverse Monte Carlo simulations becomes much more accurate and much faster compared to polychromatic excitation, since the sample response due to the polychromatic part of the excitation spectrum, the Bremsstrahlung continuum, does not need to be simulated. This not only reduces potential errors associated with the uncertainties in the polychromatic component of the excitation spectrum, but it also makes it possible to simulate/quantify each pixel spectrum in the measured XRF distributions. To illustrate the quantification capabilities for this monochromatic excitation case using the reverse Monte Carlo simulations, XRF spectra of NIST SRM 1155 (Stainless steel) were collected, quantified and compared to the certi-

fied values. All XRF Monte Carlo simulations illustrated below were performed using the in-house developed XMI-MSIM software package[24]. Figure 7.6 shows the experimental and the simulated spectra, showing that the experimental data can be simulated with a high accuracy which is confirmed by the results when performing a quantitative analysis of this NIST standard, shown in Table 7.1. In general, there is a good agreement between the certified concentrations and those that resulted from the quantitative analysis. However, the concentrations of elements like S, V, Co and Pb have large relative deviations in comparison with the certified concentrations due to peak overlap (S-Kα/Mo-Lα, Co/Fe-Kβ+Ni-Kα) and the non-optimised detector response function for low Z elements used in the XMI-MSIM simulation software. In the case of Pb, the concentration value of $10\,\mathrm{ppm}$ provided by the certificate is given by NIST for information only and this value is also close to the detection limit of Pb for this instrument. Schoonjans et al. [25] presented quantitative results of the same NIST SRM 1155 measured at a synchrotron source (beamline L, DORIS III, DESY) and obtained comparable results to the present laboratory spectrometer, as shown previously.

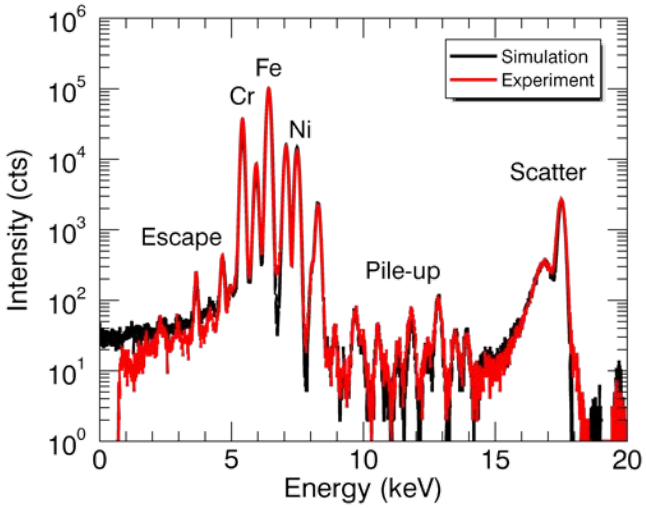

Figure 7.6: Experimental (red) and simulated (black) XRF spectrum corresponding to the NIST SRM 1155 sample measured with a detector dwell time of $450\,\mathrm{s}$ *(LT).*

	Certified (w%)	Calculated (w%)	Standard deviation (w%)	Relative deviation (%)	Relative difference (%)
S	0.018	0.01	< 0.01	13	-28
V	0.051	0.03	< 0.01	6	-44
Cr	18.370	18.00	0.04	< 1	-2
Mn	1.619	1.60	0.01	1	-1
Fe$^{\bullet}$	64.192	63.94	0.09	< 1	< 1
Co	0.105	0.30	0.01	4	185
Ni	12.350	12.47	0.04	< 1	1
Cu	0.173	0.16	< 0.01	3	-7
As†	0.011	0.01	< 0.01	9	7
W*	0.110	0.11	< 0.01	3	1
Pb*	0.001	< 0.01	< 0.01	46	179

Table 7.1: Results of reverse Monte Carlo quantitative analysis of NIST SRM 1155. Elements marked with † are reference only, elements marked with ⋆ are informative only. Fe has no certified value and is marked with •, its certified value was calculated based on all other certified concentrations.

7.3.5 Application

7.3.5.1 Quantitative elemental mapping of meteoritic materials for planetary science

As an application example, quantitative 2D elemental mapping is illustrated on a rare iron meteorite. In general, iron meteorites chemical classification is based on the contents of, and ratios between certain elements of interest as Ga, Ge, As, Ir, Ni and Au[22]. The crystallisation history of the iron meteorites parent bodies is determined using the bulk concentrations of several elements.[37] Besides the above mentioned elements, other elements such as Pt, Os and Au, have an impact on the right determination and classification of iron meteorites. However, the pool of analytical data for particular elements is scarce, thus limiting the right classification. Studies by Ryan et al. [38] and Hoashi et al. [39] showed the importance of concentration ratios of several platinum group elements, providing a powerful tool for taxonomic classification of iron meteorites. Due to the sensitive nature of inductively coupled plasma mass spectrometry (ICP-MS), it is the most commonly used technique for (ultra)trace elemental analysis. ICP-MS is in its standard form only applicable on aqueous solutions, however, by the

use of a laser ablation (LA) as means of sample introduction unit, it permits the direct analysis of solid samples. For the evaluation of LA-ICP-MS for quantitative trace elemental analysis of iron meteorites, a cross comparison was conducted with quantitative μXRF imaging[22]. The example given, describes the μXRF measurement and quantification of an iron meteorite, named Cheder, which was found on October 26, 2003 in Kyzyl, Russia, and was used for the validation of the LA-ICP-MS analysis[40]. Based on the classification system for iron meteorites, it was first published as an IIIAB class iron meteorite, however since then it has been re-classified as a IID class iron meteorite, meaning that the meteorite is expected to contain $9.8 - 11.3\,\%$ Ni[40, 41]. A 2D scan was performed of 37×112 pixels with 75 (H) and $25\,\mu\mathrm{m}$ (V) step sizes respectively, utilising a dwell time of $50\,\mathrm{s}$ per pixel with an X-ray tube setting of $0.4\,\mathrm{mA}$ and $40\,\mathrm{kV}$ resulting in a flux of $1.2 \times 10^7\,{}^{\mathrm{photon}}/_{\mathrm{s}}$. The obtained spectra were deconvoluted using AXIL[42] while the net line intensities were visualised using in-house developed software to obtain elemental distribution images, shown in Figure 7.7.

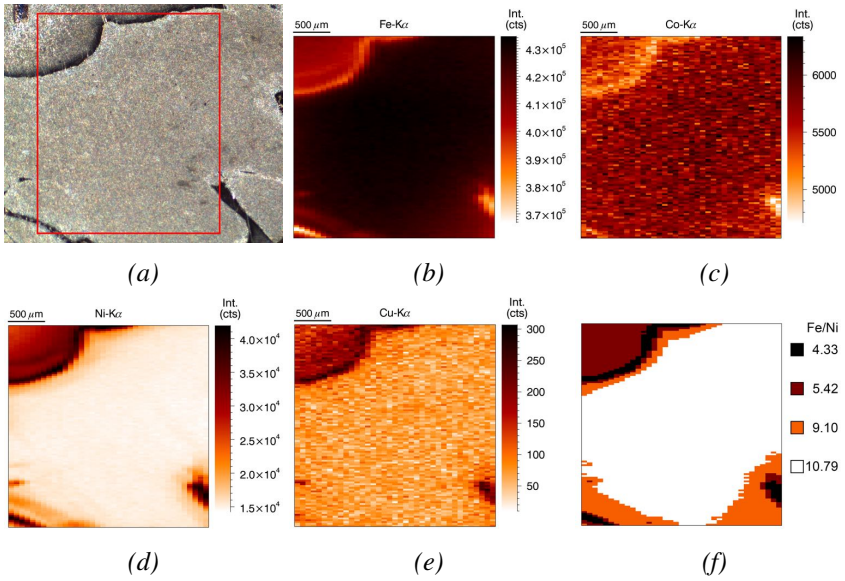

Figure 7.7: (a) Optical image of the examined surface of the Cheder iron meteorite showing the measured area in red ($2.8 \times 2.8\,\mathrm{mm}^2$). (b-e) Elemental distribution images of Fe, Co, Ni, and Cu. (f) Homogeneous regions obtained by K-means clustering and their corresponding Fe to Ni ratio of the performed 2D mapping ($37 \times 75\,\mu\mathrm{m}$ (H) by $112 \times 25\,\mu\mathrm{m}$ (V), ${}^{50\,\mathrm{s}}/_{\mathrm{pixel}}$, $0.4\,\mathrm{mA}$, $40\,\mathrm{kV}$)

A special interest is the Fe/Ni ratio in the different regions, which are individually homogeneous, of the meteorite. Therefore the data was treated using a K-means clustering algorithm implemented in the in-house developed software package Microxrf2[43]. To avoid a biased K-means clustering, a square root transformation and a region of interest normalisation were applied, giving an equal weight to both elements of interest, Fe and Ni. Each obtained cluster was then quantified using the iterative reverse Monte Carlo simulation quantification scheme, of which the results are summarised in Figure 7.7f and Table 7.2.

	Calculated (w%)	Standard deviation (w%)	Relative deviation (%)
Fe	90.07	<0.01	0.01
Co	1.31	<0.01	0.05
Ni	8.35	<0.01	0.02
Cu	0.04	<0.01	0.30
Ga	0.01	<0.01	0.52
Ge	0.01	<0.01	0.43

Table 7.2: Calculated elemental concentration values (weight %) obtained by a reverse Monte Carlo quantification scheme corresponding to the main cluster (white cluster in Figure 7.7f) of the Cheder iron meteorite.

The iron meteorite forms a challenging sample for quantitative calculations since the Ni fluorescent photons are able to excite Fe-K shell electrons, causing significant self enhancement effects, showing the importance of the ability to simulate high order effects. In this particular case, the simulation tracked photons that had up to 4 interactions before reaching the detector. The different interaction contributions can be found in Table 7.3, showing that the total fluorescent intensity for Ni is determined by first order interactions, while for Fe both first and second order interactions are important due to the self enhancement effect caused by the Ni fluorescent photons. Not taking into account of higher order interactions would result in incorrectly calculated Fe concentrations, resulting in an underestimation of nearly $5\,\%$. For more information regarding the influence of higher order effects on the total fluorescence intensity, the authors would like to refer to Schoonjans et al. [24].

n	Fe-KL_3 (%)	Ni-KL_3 (%)
1	95.35	99.08
2	4.57	0.91
3	0.08	< 0.01
4	< 0.01	0

Table 7.3: Contribution of the interaction order (n) to the total fluorescence intensity for the iron meteorite simulation showing the enhancement effect of Fe caused by Ni fluorescent photons.

The obtained concentration values are in good agreement with quantified results from the same sample determined by other analytical techniques, including LA-ICP-MS, showing the quantitative performance of this laboratory instrument based on monochromatic excitation[22, 44]. Due to the good agreement with other analytical techniques, the non destructive nature of μXRF imaging and the high sensitive of this laboratory instrument based on monochromatic excitation, it forms a valuable instrument towards a better taxonomic classification of iron meteorites. From a methodological point of view, the applicability of Monte Carlo simulation based quantification schemes in 2D elemental imaging (made possible by the monochromatic excitation) represents a significant milestone compared to currently used approaches employed in case of polychromatic excitation.

7.4 Conclusions

A newly developed laboratory XRF microprobe is described based on a novel monochromatic excitation source. The applied X-Beam (XOS, Albany, USA) microfocus X-ray tube has an integrated (custom made) three-segment doubly curved crystal (DCC) optic, providing a focal spot of 120 (H) by $46\,\mu\mathrm{m}$ (V). Using a state-of-the-art $60\,\mathrm{mm}^2$ energy dispersive SDD detector, optimised for energy resolution and/or throughput for different usage scenarios, relative detection limits reach sub-ppm levels (down to $400\,\mathrm{ppb}$) for the most efficiently excited/detected elements in $1000\,\mathrm{s}$ in case of biological sample matrices. The achieved detection limits represent an improvement of approximately an order of magnitude compared to polychromatic based laboratory and portable systems. This microprobe is therefore very suitable for trace element imaging in case of applications where sensitivity has preference over e.g. spatial resolution, which can still be improved upon when compared to other state-of-the-art laboratory spec-

trometers. Despite the fact that Al can be detected when the concentration is high enough, this spectrometer is in its current state not suited for trace elemental analysis of light elements (Na to S) due to the lack of a sample environment in vacuum or which can be improved upon by purging the detection path by He. Although depth sensitive or 3D XRF measurements are currently not possible, this functionality can easily be added by a future expansion of the spectrometer with a polycapillary half lens at the detector side.

Next to superior peak-to-background ratios, resulting in low detection limits, compared to polychromatic excitation based XRF spectrometers, another important aspect of the applied monochromatic microbeam source is the dramatically improved potential for quantitative analysis using Monte Carlo based quantification methods. This is on the one hand due to the short simulation time needed to model XRF spectra induced by monochromatic excitation and, on the other hand, due to the elimination of the uncertainties that are typically associated with the error-prone determination of the polychromatic excitation spectrum. The demonstrated quantitative analysis using reverse Monte Carlo simulations on a NIST standard reference material and an iron meteorite showed the potential of this strategy towards quantitative measurements, representing an important step in the generalisation of quantitative approaches in scanning XRF spectrometry.

7.5 Acknowledgement

The authors thank Dr. Ning Gao and XOS for the custom designed X-ray tube. Stepan M. Chernonoshkin, Dr. Steven Goderis and Prof. Dr. Frank Vanhaecke of the Ghent University for providing the meteorite sample.

References

[1] J. Garrevoet, B. Vekemans, S. Bauters, A. Demey, and L. Vincze. Development and applications of a laboratory micro x-ray fluorescence (xrf) spectrometer using monochromatic excitation for quantitative elemental analysis. *Analytical Chemistry*, 2015. doi: 10.1021/acs.analchem.5b00770.

[2] A. Migliori, P. Bonanni, L. Carraresi, N. Grassi, and P. A. Mando. A novel portable XRF spectrometer with range of detection extended to low-Z elements. *X-RAY SPECTROMETRY*, 40(2):107–112, MAR-APR 2011. ISSN 0049-8246.

[3] I. Mantouvalou, K. Lange, T. Wolff, D. Groetzsch, L. Luehl, M. Haschke, O. Hahn, and B. Kanngiesser. A compact 3D micro X-ray fluorescence spectrometer with X-ray tube excitation for archaeometric applications. *JOURNAL OF ANALYTICAL ATOMIC SPECTROMETRY*, 25(4):554–561, 2010. ISSN 0267-9477.

[4] M. Shanmugam, S. Vadawale, Y. B. Acharya, V. Mishra, P. N. Patel, and S. K. Goyal. Design and performance evaluation of SDD based X-ray spectrometer for future planetary exploration. *RADIATION MEASUREMENTS*, 47(5):375–382, MAY 2012. ISSN 1350-4487.

[5] S. Komatani, K. Nakamachi, K. Nakano, S. Ohzawa, H. Uchihara, A. Bando, and K. Tsuji. Fundamental characteristics of hybrid X-ray focusing optics for micro X-ray fluorescence analysis. *NUCLEAR INSTRUMENTS & METHODS IN PHYSICS RESEARCH SECTION B-BEAM INTERACTIONS WITH MATERIALS AND ATOMS*, 309(): 260–263, AUG 15 2013. ISSN 0168-583X. doi: {10.1016/j.nimb.2013.02.023}.

[6] S. Cornaby. Moxtek's ULTRA-LITE X-ray Source. *SPECTROSCOPY*, 1(S):11, FEB 2013. ISSN 0887-6703.

[7] Y. Iwai, T. Koike, Y. Hayama, A. Jouzuka, T. Nakamura, Y. Onizuka, M. Miyoshi, and H. Mimura. X-ray tube with a graphite field emitter inflamed at high temperature. *JOURNAL OF VACUUM SCIENCE & TECHNOLOGY B*, 31(2), MAR 2013. ISSN 1071-1023. doi: {10.1116/1.4769970}.

[8] S. J. Piercey and M. C. Devine. Analysis of powdered reference materials and known samples with a benchtop, field portable

X-ray fluorescence (pXRF) spectrometer: evaluation of performance and potential applications for exploration lithogeochemistry. *GEOCHEMISTRY-EXPLORATION ENVIRONMENT ANALYSIS*, 14 (2):139–148, MAY 2014. ISSN 1467-7873.

[9] G. L. Bosco. Development and application of portable, hand-held X-ray fluorescence spectrometers. *TRAC-TRENDS IN ANALYTICAL CHEMISTRY*, 45:121–134, APR 2013. ISSN 0165-9936.

[10] J. Johnson. Accurate Measurements of Low Z Elements in Sediments and Archaeological Ceramics Using Portable X-ray Fluorescence (PXRF). *JOURNAL OF ARCHAEOLOGICAL METHOD AND THEORY*, 21(3):563–588, SEP 2014. ISSN 1072-5369. doi: {10.1007/s10816-012-9162-3}.

[11] J. Garrevoet, B. Vekemans, P. Tack, B. De Samber, S. Schmitz, F. E. Brenker, G. Falkenberg, and L. Vincze. Methodology toward 3d micro x-ray fluorescence imaging using an energy dispersive charge-coupled device detector. *Analytical Chemistry*, 86(23):11826–11832, 2014. doi: 10.1021/ac503410s.

[12] M. Radtke, G. Buzanich, J. Curado, U. Reinholz, H. Riesemeier, and O. Scharf. Slicing - a new method for non destructive 3D elemental sensitive characterization of materials. *JOURNAL OF ANALYTICAL ATOMIC SPECTROMETRY*, 29(8):1339–1344, AUG 2014. ISSN 0267-9477. doi: {10.1039/c4ja00085d}.

[13] M.D. de Jonge, C.G. Ryan, and C.J. Jacobsen. X-ray nanoprobes and diffraction-limited storage rings: opportunities and challenges of fluorescence tomography of biological specimens. *JOURNAL OF SYNCHROTRON RADIATION*, 21(5):1031–1047, SEP 2014. ISSN 0909-0495. doi: {10.1107/S160057751401621X}.

[14] M. Dehlinger, C. Fauquet, S. Lavandier, O. Aumporn, F. Jandard, V. Arkadiev, A. Bjeoumikhov, and D. Tonneau. Spatial resolution of confocal XRF technique using capillary optics. *NANOSCALE RESEARCH LETTERS*, 8, JUN 7 2013. ISSN 1931-7573. doi: {10.1186/1556-276X-8-271}.

[15] M. Dehlinger, C. Fauquet, F. Jandard, A. Bjeoumikhov, S. Bjeoumikhova, R. Gubzhokov, A. Erko, I. Zizak, D. Pailharey, S. Ferrero, B. Dahmani, and D. Tonneau. Toward sub-micro-XRF working at nanometer range using capillary optics. *X-RAY SPECTROMETRY*, 42 (6):456–461, NOV 2013. ISSN 0049-8246. doi: {10.1002/xrs.2503}.

[16] T. Nakazawa and K. Tsuji. Development of a high-resolution confocal micro-XRF instrument equipped with a vacuum chamber. *X-RAY SPECTROMETRY*, 42(5):374–379, SEP 2013. ISSN 0049-8246. doi: {10.1002/xrs.2458}.

[17] S. Smolek, T. Nakazawa, A. Tabe, K. Nakano, K. Tsuji, C. Streli, and P. Wobrauschek. Comparison of two confocal micro-XRF spectrometers with different design aspects. *X-RAY SPECTROMETRY*, 43 (2):93–101, MAR 2014. ISSN 0049-8246.

[18] I. Mantouvalou, T. Wolff, C. Seim, V. Stoytschew, W. Malzer, and B. Kanngiesser. Reconstruction of Confocal Micro-X-ray Fluorescence Spectroscopy Depth Scans Obtained with a Laboratory Setup. *ANALYTICAL CHEMISTRY*, 86(19):9774–9780, OCT 7 2014. ISSN 0003-2700. doi: {10.1021/ac502342t}.

[19] P. Wrobel and M. Czyzycki. Direct deconvolution approach for depth profiling of element concentrations in multi-layered materials by confocal micro-beam X-ray fluorescence spectrometry. *TALANTA*, 113: 62–67, SEP 15 2013. ISSN 0039-9140. doi: {10.1016/j.talanta.2013.03.087}.

[20] M. Guerra, S. Longelin, S. Pessanha, M. Manso, and M. L. Carvalho. Development of a combined portable x-ray fluorescence and Raman spectrometer for in situ analysis. *REVIEW OF SCIENTIFIC INSTRUMENTS*, 85(6), JUN 2014. ISSN 0034-6748.

[21] L. Beck, H. Rousselière, J. Castaing, A. Duran, M. Lebon, B. Moignard, and F. Plassard. First use of portable system coupling x-ray diffraction and x-ray fluorescence for in-situ analysis of prehistoric rock art. *Talanta*, 129(0):459 – 464, 2014. ISSN 0039-9140. doi: http://dx.doi.org/10.1016/j.talanta.2014.04.043.

[22] S. M. Chernonozhkin, S. Goderis, S. Bauters, B. Vekemans, L. Vincze, P. Claeys, and F. Vanhaecke. Evaluation of pneumatic nebulization and ns-laser ablation ICP-MS for bulk elemental analysis and 2-dimensional element mapping of iron meteorites. *JOURNAL OF ANALYTICAL ATOMIC SPECTROMETRY*, 29:1001–1016, 2014.

[23] N. Metropolis. The beginning of the monte carlo method. *LOS ALAMOS SCIENCE SPECIAL ISSUE*, 1(15), 1987.

[24] T. Schoonjans, L. Vincze, V.A. Sole, M.S. del Rio, P. Brondeel, G. Silversmit, K. Appel, and C. Ferrero. A general Monte Carlo simulation

of energy dispersive X-ray fluorescence spectrometers - Part 5 Polarized radiation, stratified samples, cascade effects, M-lines. *SPECTROCHIMICA ACTA PART B-ATOMIC SPECTROSCOPY*, 70:10–23, APR 2012. ISSN 0584-8547.

[25] T. Schoonjans, V.A. Sole, L. Vincze, M. S. del Rio, K. Appel, and C. Ferrero. A general Monte Carlo simulation of energy-dispersive X-ray fluorescence spectrometers - Part 6. Quantification through iterative simulations. *SPECTROCHIMICA ACTA PART B-ATOMIC SPECTROSCOPY*, 82:36–41, APR 1 2013. ISSN 0584-8547.

[26] L. Vincze, K. Janssens, B. Vekemans, and F. Adams. Monte Carlo simulation of X-ray fluorescence spectra: Part 4. Photon scattering at high X-ray energies. *SPECTROCHIMICA ACTA PART B-ATOMIC SPECTROSCOPY*, 54(12):1711–1722, NOV 22 1999. ISSN 0584-8547.

[27] L. Vincze, K. Janssens, F. Adams, and K.W. Jones. A general monte carlo simulation of energy-dispersive X-ray fluorescence spectrometers .3. Polarized polychromatic radiation, homogeneous samples. *SPECTROCHIMICA ACTA PART B-ATOMIC SPECTROSCOPY*, 50 (12):1481–1500, OCT 1995. ISSN 0584-8547.

[28] L. Vincze, K. Janssens, F. Adams, M.L. Rivers, and K.W. Jones. A General Monte-Carlo Simulation of ED-XRF Spectrometers .2. Polarized Monochromatic Radiation, Homogeneous Samples. *SPECTROCHIMICA ACTA PART B-ATOMIC SPECTROSCOPY*, 50(2): 127–147, MAR 1995. ISSN 0584-8547.

[29] L. Vincze, K. Janssens, and F. Adams. A General Monte-Carlo Simulation of Energy-Dispersive X-ray-Fluorescence Spectrometers .1. Unpolarized Radiation, Homogeneous Samples. *SPECTROCHIMICA ACTA PART B-ATOMIC SPECTROSCOPY*, 48(4):553–573, MAR 1993. ISSN 0584-8547.

[30] R. A. Crocombe. Handheld spectrometers: the state of the art. In Druy, MA and Crocombe, RA, editor, *NEXT-GENERATION SPECTROSCOPIC TECHNOLOGIES VI*, volume 8726 of *Proceedings of SPIE*, 1000 20TH ST, PO BOX 10, BELLINGHAM, WA 98227-0010 USA, 2013. SPIE, SPIE-INT SOC OPTICAL ENGINEERING. ISBN 978-0-8194-9517-4. doi: {10.1117/12.2017892}. Conference on Next-Generation Spectroscopic Technologies VI, Baltimore, MD, APR 29-30, 2013.

[31] A. Maderitsch, S. Smolek, P. Wobrauschek, C. Streli, and P. Takman. Feasibility study of total reflection X-ray fluorescence analysis using a liquid metal jet X-ray tube. *SPECTROCHIMICA ACTA PART B-ATOMIC SPECTROSCOPY*, 99(1):67–69, SEP 1 2014. ISSN 0584-8547. doi: {10.1016/j.sab.2014.06.003}.

[32] S. Kunimura and J. Kawai. Trace elemental determination by portable total reflection X-ray fluorescence spectrometer with low wattage X-ray tube. *X-RAY SPECTROMETRY*, 42(3):171–173, MAY-JUN 2013. ISSN 0049-8246. doi: {10.1002/xrs.2445}.

[33] M. West, A. T. Ellis, P. J. Potts, C. Streli, C. Vanhoof, and P. Wobrauschek. 2014 Atomic Spectrometry Update - a review of advances in X-ray fluorescence spectrometry. *JOURNAL OF ANALYTICAL ATOMIC SPECTROMETRY*, 29(9):1516–1563, SEP 2014. ISSN 0267-9477. doi: {10.1039/c4ja90038c}.

[34] R. Van Grieken and A. Markowicz. *Handbook of X-Ray Spectrometry, Second Edition*. CRC PRESS, 2001.

[35] T. Schoonjans, A. Brunetti, B. Golosio, M.S. del Rio, V.A. Sole, C. Ferrero, and L. Vincze. The xraylib library for X-ray-matter interactions. Recent developments. *SPECTROCHIMICA ACTA PART B-ATOMIC SPECTROSCOPY*, 66(11-12):776–784, NOV-DEC 2011. ISSN 0584-8547.

[36] M. Guerra, M. Manso, S. Pessanha, S. Longelin, and M. L. Carvalho. Theoretical and experimental study on the angular dependence of scattering processes in X-ray fluorescence systems. *X-RAY SPECTROMETRY*, 42(5):402–407, SEP 2013. ISSN 0049-8246. doi: {10.1002/xrs.2491}.

[37] J. I. Goldstein, E. R. D. Scott, and N. L. Chabot. Iron meteorites: Crystallization, thermal history, parent bodies, and origin. *CHEMIE DER ERDE-GEOCHEMISTRY*, 69(4):293–325, 2009. ISSN 0009-2819. doi: {10.1016/j.chemer.2009.01.002}.

[38] D.E. Ryan, J. Holzbecher, and R.R. Brooks. Rhodium and Osmium in Iron-Meteorites. *CHEMICAL GEOLOGY*, 85(3-4):295–303, JUL 30 1990. ISSN 0009-2541. doi: {10.1016/0009-2541(90)90006-S}.

[39] M. Hoashi, R.R. Brooks, and R.D. Reeves. Palladium, Platinum and Ruthenium in Iron-Meteorites and their Taxonomic Significance. *CHEMICAL GEOLOGY*, 106(3-4):207–218, JUN 25 1993. ISSN 0009-2541. doi: {10.1016/0009-2541(93)90027-G}.

[40] S.S. Russell, L. Folco, M.M. Grady, M.E. Zolensky, R. Jones, K. Righter, J. Zipfel, and J.N. Grossman. The Meteoritical Bulletin, No. 88, 2004 July. *METEORITICS & PLANETARY SCIENCE*, 39(8, S):A215–A272, AUG 2004. ISSN 1086-9379.

[41] H. C. Connolly, J. Zipfel, J. N. Grossman, L. Folco, C. Smith, R. H. Jones, K. Righter, M. Zolensky, S. S. Russell, G. K. Benedix, A. Yamaguchi, and B. A. Cohen. The Meteoritical Bulletin, No. 90, 2006 September. *METEORITICS & PLANETARY SCIENCE*, 41(9): 1383–1418, 2006. ISSN 1945-5100.

[42] B. Vekemans, K. Janssens, L. Vincze, F. Adams, and P. Vanespen. ANALYSIS OF X-RAY-SPECTRA BY ITERATIVE LEAST-SQUARES (AXIL) - NEW DEVELOPMENTS. *X-RAY SPECTROMETRY*, 23(6):278–285, NOV-DEC 1994. ISSN 0049-8246.

[43] B. Vekemans, K. Janssens, L. Vincze, A. Aerts, F. Adams, and J. Hertogen. Automated segmentation of mu-XRF image sets. *X-RAY SPECTROMETRY*, 26(6):333–346, NOV-DEC 1997. ISSN 0049-8246.

[44] L. V. Agafonov, V. A. Popov, G. N. Anoshin, L. N. Pospelova, V. I. Zabelin, and V. I. Kudryavtsev. The Cheder iron meteorite (Tuva): mineral composition, structure, and PGE and REE contents. *RUSSIAN GEOLOGY AND GEOPHYSICS*, 52(6):620–630, JUN 2011. ISSN 1068-7971.

8
Conclusion and Outlook

This worked shows the characterisation of an Energy Dispersive (ED) pixel detector, called the SLcam®, Chapter 3. The detector offers an outstanding ER of $156\,\mathrm{eV}$ at the Mn-Kα line and can handle a count rate of $450\,\mathrm{kcps}$ using a $450\,\mu\mathrm{m}$ thick Si chip, offering a high quantum efficiency up to $20\,\mathrm{keV}$. The ability to mount several different optics in front of the detector ensures a flexibility towards field of view (max. $12^2\,\mathrm{mm}^2$) and obtained resolution (max. $8^2\,\mu\mathrm{m}^2$). This property was extensively used during the measurements performed at various beamlines at third generation synchrotron sources.
Chapter 4 shows the application of the SLcam® to obtain 2D elemental distribution images of a variety of samples without the need to move the sample in a short period of time due to the simultaneous recording of nearly 70,000 pixels. When measuring heterogeneous samples, a large field of view is often needed. Although when utilising the detector in the modus resulting in the largest field of view "only" provides a resolution of $48^2\,\mu\mathrm{m}^2$, one could easily change the optic and record an image with a higher resolution of a specific region of interest, or can be combined with a scanning based system to achieve even higher resolutions.

A novel methodology to obtain three dimensional elemental information about your sample was presented in Chapter 5. By combining a thin sheet beam, orientated parallel with the detector chip of the SLcam®, one illuminates only a certain cross section of the sample. Since the detector is parallel to the primary X-ray beam, one immediately obtains 2D elemental

distribution images of a specific depth in the sample. A linear scan perpendicular to the sheet beam results in a 3D representation of the elements in the sample without the need of any reconstruction algorithm, therefore not introducing additional noise or reconstruction artefacts in the final image. Due to the way of detection, the correction of self absorption effects is more straight forward than for CT approaches. The proposed methodology also enable imaging of much larger volumes than was ever achieved before, due to the time consuming characteristic of conventional scanning based methodologies as confocal XRF or XRF CT. The latter however got a major gain in popularity by the introduction of novel detector technology, like the Maia detector, which optimises the detector solid angle, aiming for sub milliseconds dwell times.

Both approaches, large area pixel detectors Vs. fast detectors with a large solid angle, seem to be at first glance competing methodologies. This is however not the case, which approach is better depends on the sample and the goal of the experiment. For 2D imaging, large area detectors are able to offer higher resolution images in the same time frame, compared to the SLcam. There are exceptions, measurements of samples in sample environments or with equipment attached for in-situ experiments, or samples which do not allow for fast sample movements.

For 3D imaging, the attenuation of the sample will become more important since the CT approach of the large area detectors will fail due to self absorption effects in the sample, while the slicing methodology will allow you to image until the information depth is reached. For small less absorbing samples, large area detectors can have the upper hand. Examples were shown of 3D elemental distribution images obtained from measurements conducted on deep Earth diamonds with natural inclusions in them.

Each different methodology, CT or full-field based, has its own advantages and disadvantages towards quantitative XRF imaging.

Chapter 6 described a methodology towards tomographic XRF imaging based on the collimation of the SLcam® with a slit and illuminating the sample with a pencil beam. By placing a slit orientated perpendicular to the pencil beam, one converts the SLcam® from a 2D to a 1D detector, but one increases the solid angle since each column on the detector represents a single pixel along the illuminated path. By scanning the pencil beam perpendicular to the beam path, one obtains 3D imaging capabilities without the need of any reconstruction algorithm. An experiment at high energy ($E_0 = 50\,\mathrm{keV}$) was conducted, by producing tomographic slices in teeth of chimpanzees and Neanderthals.

What all these methodologies based on the use of ED pixel detectors have in common is the fact that the achievable resolution depends on the

development of new optics or on new detector chips, which in general is a slow process, where nanometre X-ray beams can already be produced using Fresnel zone plates. The attractiveness of the use of ED pixel detectors also depends on their total amount of pixels, which will increase in the future, just imagine having an ED detector with 4k by 4k pixels.

The SLcam® detector is one of the many attempts to make up arrears in detector technology to be able to cope with the increasing flux of current and future generation of X-ray sources. If detector technology does not catch up, the ultimate storage rings of the future will be useless for XRF imaging purposes.

Chapter 7 shows the development and applications of a laboratory μXRF spectrometer based on monochromatic excitation. An in depth characterisation of all the components was conducted to enable the experimentalist to adapt the setup to the needs of the application. Due to the monochromatic nature of the primary X-rays, one achieves very good signal-to-background ratios, which are being expressed in the excelled limits of detection. A quantification scheme was developed using reverse iterative Monte Carlo simulations using the in house developed software package XMI-MSIM. The quantitative resolving power was shown using a NIST SRM and applied on an Iron based meteorite.

A

Gaussian Coefficients

The Gaussian fit used in this thesis contains four coefficients. The general function is the following:

$$f(x) = A_0 \cdot \mathrm{e}^{\frac{-\left(\frac{x-A_1}{A_2}\right)^2}{2}} + A_3 \tag{A.1}$$

Where:

- A_0 the height of the Gaussian;
- A_1 the center of the Gaussian;
- A_2 the width (the standard deviation) of the Gaussian;
- a_3 the constant term.

B

^{55}Fe Source Certificate

Short description of the Fe55 source

Certificate No. 144855 – TP 313 for a sealed radioactive source: given by Eckert & Ziegler Nuclitec GmbH, Gieselweg 1, D-38110 Braunschweig (tel:+49 5307 932-0)

Fe-55 sealed radioactive source Model: IEC120
Fe-55 x-ray source activity:
3.7 MBq (0.1 mCi)
1.15×10^5 photons (Mn X-rays) /s/steradian [13 May 2011]
Fe-55 x-ray source capsule: VZ-2937-001 (X.0709)
ISO classification: C.44342
US Model no.: IEC.A1
Remark: The photon flux per solid angle is related to the emission of 5.9 to 6.5 keV photons (Mn-K-radiation) penetrating through the front window

Fe-55 is electrodeposited as iron metal on the face of a copper substrate, 12.5 mm diameter 3 mm thick covered with a protective nickel layer.

X.0709*
VZ-2937

Safety performance testing

ANSI/ISO classification	US Model number
C44342*	IEC.A1

*C33232 in USA

* X.0709 manufactured according to drawing VZ-2937

The source must never be modified or reworked. Potentially dangerous radioactive material may be released if the radiation source is damaged by misuse. The radiation source must only be used by qualified persons or by trained assistants working under their direct supervision. The source should be inspected before and after use to ensure that there are no obvious signs of damage. To clean carefully any foreign matter from the outside of the source for most of the sources use a cotton wool or tissue swab lightly moistened with water, ethanol or acetone.

C

SLcam TANGO server properties and attributes

SLcam TANGO server properties:

- hostname
- port number
- simulationmode

Extra information on the specific settings of the TANGO server for each different beamline can be found in the XMI wiki[1].

[1] http://we08nas1.ugent.be/XMI/index.php?title=SLcam#Beamline_integration

Tango attribute	SLcam remote command
Start	a
Stop	b
Clear	c
Record	d
Save	e
Frame record	f
Error	q

Table C.1: SLcam TANGO server attributes

D

Publications and Activities

D.1 Peer Reviewed Articles

- J. Garrevoet, B. Vekemans, S. Bauters, A. Demey, and L. Vincze. Development and applications of a laboratory micro x-ray fluorescence (xrf) spectrometer using monochromatic excitation for quantitative elemental analysis. *Analytical Chemistry*, 2015. doi: 10.1021/acs.analchem.5b00770

- L. Van de Voorde, B. Vekemans, E. Verhaeven, P. Tack, R. De Wolf, J. Garrevoet, P. Vandenabeele, and L. Vincze. Analytical characterization of a new mobile x-ray fluorescence and x-ray diffraction instrument combined with a pigment identification case study. *Spectrochimica Acta Part B: Atomic Spectroscopy*, 110(0):14 – 19, 2015. ISSN 0584-8547. doi: http://dx.doi.org/10.1016/j.sab.2015.05.002. URL `http://www.sciencedirect.com/science/article/pii/S058485471500124X`

- D. Deruytter, M.B. Vandegehuchte, J. Garrevoet, F. De Laender, E. Vergucht, K. Delbeke, R. Blust, K.A.C. De Schamphelaere, L. Vincze, and C.R. Janssen. Salinity and dissolved organic carbon both affect copper toxicity in mussel larvae: Copper speciation or competition cannot explain everything. *Environmental Toxicology and Chemistry*, pages n/a–n/a, 2015. ISSN 1552-8618. doi: 10.1002/etc.2924. URL

http://dx.doi.org/10.1002/etc.2924

- D. Bourgeois, B. Burt-Pichat, X. Le Goff, J. Garrevoet, P. Tack, G. Falkenberg, L Van Hoorebeke, L. Vincze, M.A. Denecke, D. Meyer, C. Vidaud, and G. Boivin. Micro-distribution of uranium in bone after contamination: new insight into its mechanism of accumulation into bone tissue. *Analytical and Bioanalytical Chemistry*, accepted, 2015

- Eva Vergucht, Toon Brans, Filip Beunis, Jan Garrevoet, Stephen Bauters, Maarten De Rijcke, David Deruytter, Colin Janssen, Christian Riekel, Manfred Burghammer, and Laszlo Vincze. Methodological challenges related to optical tweezers based X-ray fluorescence imaging of biological model organisms at synchrotron facilities. *JOURNAL OF SYNCHROTRON RADIATION*, accepted, 2015

- Eva Vergucht, Toon Brans, Filip Beunis, Jan Garrevoet, Maarten De Rijcke, Stephen Bauters, David Deruytter, Michiel Vandegehuchte, Ine Van Nieuwenhove, Colin Janssen, Manfred Burghammer, and Laszlo Vincze. In vivo x-ray elemental imaging of single cell model organisms manipulated by laser-based optical tweezers. *Sci. Rep.*, 5, 03 2015. URL http://dx.doi.org/10.1038/srep09049

- Maria Joanna Niemiec, Bjorn De Samber, Jan Garrevoet, Eva Vergucht, Bart Vekemans, Riet De Rycke, Erik Bjorn, Linda Sandblad, Gerd Wellenreuther, Gerald Falkenberg, Peter Cloetens, Laszlo Vincze, and Constantin Felix Urban. Trace element landscape of resting and activated human neutrophils on the sub-micrometer level. *Metallomics*, pages –, 2015. doi: 10.1039/C4MT00346B. URL http://dx.doi.org/10.1039/C4MT00346B

- Brecht Laforce, Sylvia Schmitz, Bart Vekemans, Jennifer Rudloff, Jan Garrevoet, Remi Tucoulou, Frank E. Brenker, Gema Martinez-Criado, and Laszlo Vincze. Nanoscopic x-ray fluorescence imaging of meteoritic particles and diamond inclusions. *Analytical Chemistry*, 86(24):12369–12374, 2014. doi: 10.1021/ac503764h. URL http://dx.doi.org/10.1021/ac503764h

- J. Garrevoet, B. Vekemans, P. Tack, B. De Samber, S. Schmitz, F. E. Brenker, G. Falkenberg, and L. Vincze. Methodology toward 3d micro x-ray fluorescence imaging using an energy dispersive charge-coupled device detector. *Analytical Chemistry*, 86(23):11826–11832, 2014. doi: 10.1021/ac503410s

- P. Tack, J. Garrevoet, S. Bauters, B. Vekemans, B. Laforce, E. Van Ranst, D. Banerjee, A. Longo, W. Bras, and L. Vincze. Full-Field Fluorescence Mode Micro-XANES Imaging Using a Unique Energy Dispersive CCD Detector. *Analytical Chemistry*, 86(17):8791–8797, SEP 2 2014. ISSN 0003-2700. doi: {10.1021/ac502016b}

- M.N. Boone, J. Garrevoet, P. Tack, O. Scharf, D.P. Cormode, D. Van Loo, E. Pauwels, M. Dierick, L. Vincze, and L. Van Hoorebeke. High spectral and spatial resolution X-ray transmission radiography and tomography using a Color X-ray Camera. *Nuclear Instruments & Methods in Physics Research Section A-accelerators Spectrometers Detectors and Associated Equipment*, 735:644–648, JAN 21 2014. ISSN 0168-9002

- David Deruytter, Jan Garrevoet, Michiel B. Vandegehuchte, Eva Vergucht, Bjoern De Samber, Bart Vekemans, Karen Appel, Gerald Falkenberg, Katrien Delbeke, Ronny Blust, Karel A. C. De Schamphelaere, Laszlo Vincze, and Colin R. Janssen. The Combined Effect of Dissolved Organic Carbon and Salinity on the Bioaccumulation of Copper in Marine Mussel Larvae. *Environmental Science & Technology*, 48(1):698–705, JAN 7 2014. ISSN 0013-936X. doi: {10.1021/es4024699}

- Jennifer O'Reilly, David Douglas, Julian Braybrook, P-W. So, Eva Vergucht, Jan Garrevoet, Bart Vekemans, Laszlo Vincze, and Heidi Goenaga-Infante. A novel calibration strategy for the quantitative imaging of iron in biological tissues by LA-ICP-MS using matrix-matched standards and internal standardisation. *Journal of Analytical Atomic Spectrometry*, 29(8):1378–1384, AUG 2014. ISSN 0267-9477. doi: {10.1039/c4ja00002a}

D.2 Conference Contributions

D.2.1 Invited Talks

- SLcam users meeting 2012, Berlin, Germany

D.2.2 Oral Presentations

- A new approach towards 3d elemental micro-imaging using a novel energy dispersive xrf detector, XRM 2014, 26-31 October, 2014, Melbourne, Australia

- A new methodology towards 3D micro-XRF imaging using a novel energy-dispersive CCD detector,EXRS 2014, 15-20 June, 2014, Bologna, Italy

- A new methodology towards 3D micro-XRF imaging using a novel energy-dispersive CCD detector, ICXOM 2013, 2-5 September, 2013, Hamburg, Germany

D.2.3 Poster Presentations

- Cryogenic analysis of frozen hydrated biological tissue at the hard x-ray micro-probe beamline P06 at Petra III, XRM 2014, 26-31 October, 2014, Melbourne, Australia

- High spectral and spatial resolution x-ray transmission radiography and tomography, XRM 2014, 26-31 October, 2014, Melbourne, Australia

- Full-field micro-XANES for 2D and 3D Chemical State Imaging using a Novel Energy Dispersive CCD Detector, EXRS 2014, Bologna, Italy

- Development and applications of a laboratory micro- XRF spectrometer using monochromatic excitation, EXRS 2014, 15-20 June, 2014, Bologna, Italy

- Cryogenic Synchrotron Radiation X-ray Fluorescence Analysis of Biological Model Organisms Using a State-of-the-art Cryochamber at P06, PETRA III, ChemCYS 2014, 27-28 February, 2014, Blankenberge, Belgium

- Full-field micro-XANES for 2D and 3D Chemical State Imaging using a Novel Energy Dispersive CCD Detector, ChemCYS 2014, 27-28 February, 2014, Blankenberge, Belgium

- Non-destructive elemental imaging studies of 16th - 17th century majolica tiles from antwerp (belgium) using synchrotron and laboratory based micro-xrf techniques, WIRMS 2013, 10-14 November, 2013, Lorne, Australia

- 3D Micro-XRF Imaging using a Novel Energy-Dispersive CCD Detector: A New Methodology, SYNEW 2013, 28 November, 2013, Antwerp, Belgium

- Advanced research on nickel toxicity in sediments: species, bioavailability and toxicity, SETAC 2013 North America Annual Meeting, 17-21 November, 2013, Nashville, TN, United States of America

- Development and applications of a laboratory micro- XRF spectrometer using monochromatic excitation, ICXOM 2013, 2-5 September, 2013, Hamburg, Germany

- Development of a cryogenic sample environment for the analysis of biological tissue, ICXOM 2013, 2-5 September, 2013, Hamburg, Germany

- Advanced research on nickel toxicity in sediment: species, bioavailability and toxicity, SETAC 2013 Europe Annual Meeting, 12-16 May, 2013, Glasgow, Scotland

- Advanced research on nickel toxicity in sediment: species, bioavailability and toxicity, ECHA 2013 Workshop on Risk Assessment for the Sediment Compartment, 7-8 May, 2013, Helsinki, Finland

- The combined effects of DOC and salinity on the accumulation and toxicity of copper in mussel larvae, PRIMO 2013, 5-8 May, 2013, Faro, Portugal

- The combined effects of DOC and salinity on the accumulation and toxicity of copper in mussel larvae, VLIZ 2013, 15 February, 2013, Brugge, Belgium

- A new methodology towards 3D micro-XRF imaging using a novel energy-dispersive CCD detector, HASYLAB Users Meeting 2013, 23-25 January, 2013 Hamburg, Germany

- Influence of test organism feeding type and behaviour in whole sediment toxicity tests with the oligochaete Lumbriculus variegatus, SETAC 2012, 20-24 May, 2012, Berlin, Germany

D.3 Visits

- Visiting scientist at the Hard X-ray Micro/Nano-Probe Beamline P06, Petra III, DESY, 1 June - 18 August, 2013, Hamburg, Germany

D.4 Experiments at Synchrotron Radiation Facilities

- 2010
  - October 17-20: DESY, Doris L, Inclusions in natural deep earth diamonds
- 2011
  - March: DESY, Doris L, Inclusions in natural deep earth diamonds
  - May: DESY, Doris L, Metal distribution inside biological organisms;
  - June: Petra III P06 (Nano end station), Metal distributions in mossel larvae;
  - July 6 till 12: ESRF ID22, Nanochemical Imaging of Neutrophile Extracellullar Traps (NETs)
  - October: DESY, Doris L, Enzymes on electrodes
  - November: Confocal distribution of metal distributions inside biological organisms
- 2012
  - March 19 to 27: Petra III P06 (Micro end station), Full field imaging using the SLcam
  - April 26 to 30: Petra III P06 (Micro end station), Full field imaging using the SLcam
  - May 18 to 22: DESY, Doris L, Metal distribution inside biological organisms
  - July 5 to 11: DESY, Petra III P06 (Micro end station): Quantitative sub-micron and full-field XRF analyses of mantle fluids and melts trapped in cloudy diamonds of ultra-deep sources;
  - August 24 to 27: DESY, Petra III P06 (Micro end station): Quantitative sub-micron and full-field XRF analyses of mantle fluids and melts trapped in cloudy diamonds of ultra-deep sources;
  - October 6 to 7: DESY, Doris L, Metal distribution inside mussel D-larvae
  - October 13 to 20: DESY, Petra III P06 (Nano endstation): Investigation of solar condensates

  - November 14 to 21: DESY, Petra III P06 (Micro end station), Quantitative sub-micron and full-field XRF analyses of mantle fluids and melts trapped in cloudy diamonds of ultra-deep sources;
  - November 21 to 28: DESY, Petra III P06 (Micro endstation), Nanochemical Imaging of Neutrophile Extracellullar Traps (NETs)
  - December 5 to 7: ESRF, ID13 (Micro endstation), Optical Tweezers testing;

- 2013

  - June 18 to 21: DESY, Petra III P06 (Micro end station), Uranium particles in rat bone fragments;
  - June 21 to 24: DESY, Petra III P06 (Micro end station), Quantitative sub-micron and full-field XRF analyses of mantle fluids and melts trapped in cloudy diamonds of ultra-deep sources;
  - June 24 to July 2: DESY, Petra III P06 (Micro end station), Installation of a cryogenic work flow (cryo chamber) for absorption CT and 2D/CT XRF;
  - July 26 to 31: DESY, Petra III P06 (Micro end station), Quantitative sub-micron and full-field XRF analyses of mantle fluids and melts trapped in cloudy diamonds of ultra-deep sources;
  - October 1 to 7: DESY, Petra III P06 (Micro end station), Full-field 3D XRF-imaging study of metal accumulation, distribution and effects in aquatic invertebrates exposed in complex environments;
  - November 18 to 25: ESRF BM26 (DUBBLE): Full field XANES with the SLcam;
  - December 7 to 14: DESY, Petra III P06 (Micro end station), Installation of a cryogenic work flow (cryo chamber) for absorption CT and 2D/CT XRF;

- 2014

  - January 12 to 19: ESRF, ID13 (Micro endstation), Optical Tweezers dry test;
  - January 21 to February 1: ESRF, ID19, SLcam imaging on teeth and brain tissue;
  - March 16 to 19: ESRF, ID13 (Micro endstation), Optical Tweezers;

  - May 20 to 27: ESRF, ID13 (Micro endstation), Optical Tweezers;
  - August 26 to September 2: ESRF, ID19, Elemental imaging using the SLcam on teeth;
  - October 1 to 4: ESRF, ID13 (Micro endstation), Optical Tweezers;

- 2015
  - January 30 to February 3: ESRF, ID19, Elemental imaging on mice brain using the SLcam®;
  - May 18 to 24: Petra III P06 (Micro end station), Wavelength dispersive and confocal XRF on natural inclusions in diamonds;
  - May 24 to 26: Petra III P06 (Micro end station), 3D elemental imaging on battery components;
  - June 1 to 5: Petra III P06 (Micro end station), Fast energy xanes with the Maia detector;
  - June 14 to 20: Petra III P06 (Micro end station), Wavelength dispersive and confocal XRF on natural inclusions in diamonds;
  - June 22 to 29: ESRF, ID19, Elemental imaging using the SLcam on teeth